8-17-2023

Improving the Environmental Density Mapping of Galaxies at Redshift 0.5 < z < 1.7 Using the CANDELS-Herschel Environmental Spectroscopic Survey (CHESS)

Jitrapon Lertprasertpong
jl4949@rit.edu

Improving the Environmental Density Mapping of Galaxies at Redshift $0.5 < z < 1.7$ Using the CANDELS-Herschel Environmental Spectroscopic Survey (CHESS)

JITRAPON LERTPRASERTPONG

A Thesis Submitted in Partial Fulfillment of the Requirements for the Degree of Master of Science in Astrophysical Sciences & Technology

School of Physics and Astronomy
College of Science
Rochester Institute of Technology
Rochester, NY
August 17, 2023

ASTROPHYSICAL SCIENCES AND TECHNOLOGY
COLLEGE OF SCIENCE
ROCHESTER INSTITUTE OF TECHNOLOGY
ROCHESTER, NEW YORK

CERTIFICATE OF APPROVAL

M.S. DEGREE THESIS

The M.S Degree Thesis of **Jitrapon Lertprasertpong**
has been examined and approved by the thesis
committee as satisfactory for the thesis
requirement for the M.S. degree in Astrophysical
Sciences and Technology.

Dr. Jeyhan Kartaltepe, Thesis Advisor

Dr. Andrew Robinson, Committee Member

Dr. Joshua Faber, Committee Member

Date:

Abstract

Numerous studies show that galaxies in dense environments often exhibit a decline in their star formation rates (SFR) which can be observed in the SFR-density relation, referred to as "environmental quenching." However, at redshift $z > 1$, there exists tension among different studies regarding the evolution of the SFR-density relation. One source of this uncertainty arises from the lack of spectroscopy of galaxies at $z > 1$, which can result in inaccurately estimating the environmental density of galaxies in extragalactic fields. To address this issue, we present the CANDELS-Herschel Environmental Spectroscopic Survey (CHESS) designed to increase the spectroscopic completeness in CANDELS COSMOS, UDS, and EGS fields at the redshift range of $0.5 < z < 1.7$. This spectroscopic catalog focuses on the Herschel-selected galaxies with stellar masses $M* > 10^{10}$ solar masses to accurately measure SFR for those sources and ensure an unbiased spectroscopic sampling at our redshift range. From the CHESS observation program, we obtained 677 new high-quality spectroscopic redshifts in the COSMOS, UDS, and EGS fields, including serendipitous objects. By combining our new spectroscopic catalog with the existing archival spectroscopic redshifts, we are able to construct improved overdensity maps of galaxies in all five CANDELS fields using the Monte Carlo Voronoi tessellation method. With our new CHESS catalog, we are able to detect new overdensity regions in CANDELS COSMOS, UDS, and EGS fields as well as generate an updated SFR-density relation. This new dataset allows us to probe deeper into the large-scale structure at $0.5 < z < 1.7$, and offer us new insights into the evolution of SFR with varying redshifts.

Contents

List of Figures

List of Tables

1 Introduction

1.1 The Evolution of the Star Formation Rates of Galaxies

Galaxies are gravitationally bound systems consisting of stars, gas, dust, and dark matter. Galaxy populations can be categorized into two groups based on their star formation rates (SFR): star-forming galaxies, and quiescent galaxies. Star-forming galaxies are characterized by an ongoing process of star formation while quiescent galaxies have ceased their star formation activity. The presence of young, bright, and short-lived O and B stars in star-forming galaxies make these galaxies exhibit bluer colors compared to quiescent galaxies as shown in the UVJ color-color diagram shown in Figure 1. Hence, the UVJ diagram is a useful tool to differentiate these two galaxy populations. Utilizing the UVJ color-color diagram to track the evolution of galaxies, we notice that galaxies tend to migrate from star-forming galaxies to quiescent galaxies with cosmic time as shown in Figure 2.

The decline of star formation is also evident in the SFR-M* plane. Star-forming galaxies populate the region known as the "star-forming main sequence" (SFMS) on the SFR-M* plane. At high redshifts, galaxies tend to have higher SFRs, elevated compared to the star forming main sequence observed in the local universe (Schreiber et al. 2015). The evolution of the specific star formation rate (SFR/M*) as a function of redshift also shows that the star formation rate density (SFRD) reaches its peak at around $z = 2$ as shown in Figure 3 (Madau & Dickinson 2014). The overall decline of star formation of galaxies implies the decrease in the rate that which galaxies are forming new stars, known as "galaxy quenching."

In general, the cessation of star formation is closely tied to the amount of gas reservoirs inside galaxies. There is a well-known relation between the amount of gas inside the galaxies and the star formation rate of the galaxies known as the Schmidt-Kennicutt law (Schmidt 1959; Robert C. Kennicutt 1998). This law implies that certain physical processes such as AGN feedback (Combes 2017), supernova feedback (Bermejo-Climent et al. 2018), mergers (Gabor et al. 2010), and interactions with the surrounding environment, can deplete the gas reservoir within galaxies, leading to their quenching. In this research, we primarily focus on the role of the environment in the termination of star formation.

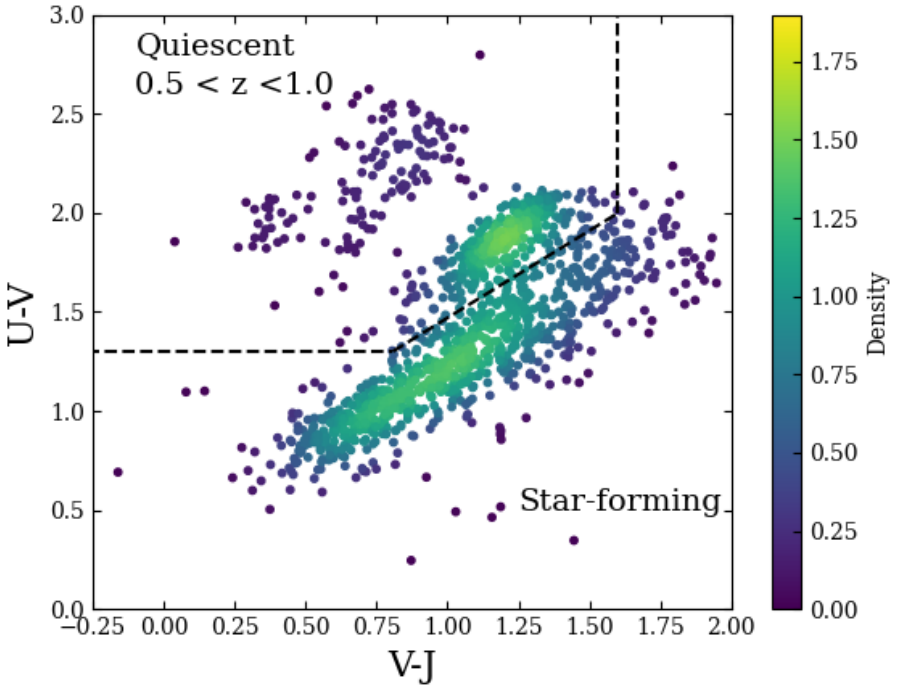

Figure 1: The rest-frame UVJ color-color diagram at redshift range $0.5 < z < 1.0$ created using galaxies from the COSMOS photometric catalog (Nayyeri et al. 2017). The dashed line indicates the division between star-forming and quiescent galaxy populations defined by the selection criteria based on Williams et al. (2009). This plot shows the bimodal distribution of the galaxy population that can be used to distinguish star-forming galaxies from quiescent galaxies.

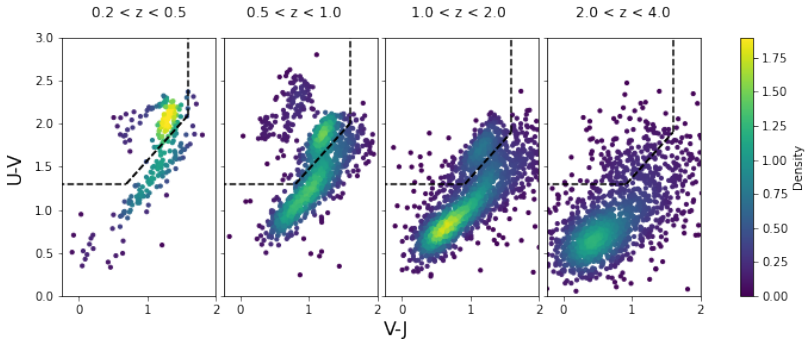

Figure 2: The evolution of the rest-frame UVJ diagrams from redshift $z = 0.2$ to $z = 4.0$. At high redshift, galaxies populate primarily in the star-forming region on the UVJ diagram. At lower redshift, galaxies tend to migrate from star-forming population to quiescent population. This evolution implies the quenching process that shuts down star formation of galaxies over cosmic time.

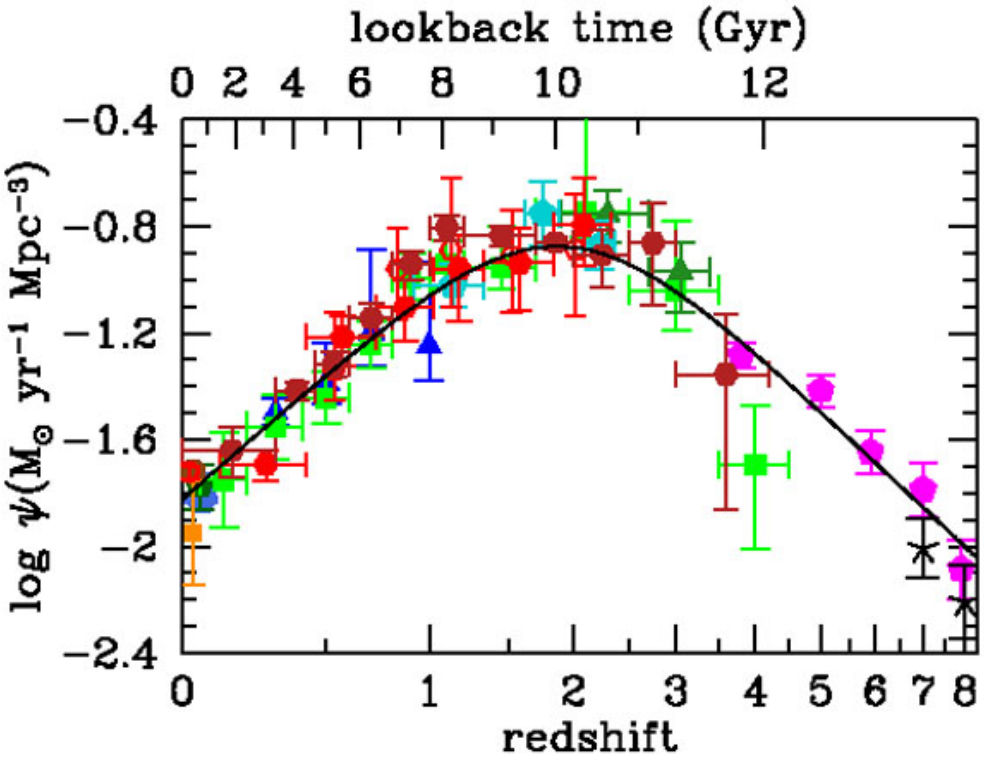

Figure 3: The cosmic star formation history (SFH) from far-UV (FUV) and infrared (IR) rest-frame measurements excerpted from Madau & Dickinson (2014). This plot captures the evolution of star formation rate density (SFRD) ψ as a function of redshift. From this plot, the SFRD reaches its peak at around the redshift between $z = 2$ and 1.5, then declines until the present day.

1.2 Environmental Quenching

In addition to the overall decline of star formation observed in the local universe, galaxies often experience the termination of star formation processes in dense environments. In this study, we define the environment as the local number density of the extragalactic field. There are several studies of the environmental quenching of galaxies. In 1978, Butcher & Oemler (1978) found that galaxies in the core of the cluster at intermediate redshift ($z \sim 0.4$) tend to be bluer than galaxies in the core of the cluster in the local universe. According to the Butcher-Oemler effect, the SFR in a dense environment is lower than the SFR in a less dense environment. This change in SFR implies that galaxies can be quenched in a high-density environment such as galaxy clusters. The data from SDSS, zCOSMOS, and other deep surveys showed that environmental quenching at fixed overdensity does not have a significant influence on galaxies at $z < 1$ (Peng et al. 2010). This result suggests that environmental quenching occurs during the formation of large-scale structures of the universe. There are multiple processes involved in environmental quenching, such as the reduction of gas inflow (strangulation), ram-pressure stripping, and frequent galaxy interaction (harassment) (Feldmann & Mayer 2014).

We can identify the environmental quenching using the SFR-density relation, which is the relation between SFR and the number density of the environment that the galaxy resides in. While the SFR-density relation shows clear evidence that the SFR of galaxies drops in high-density environments, the SFR-density relation at $z > 1$ introduces a new problem in extragalactic astrophysics. Many studies show the reversal of SFR-density relation at $z > 1$ (e.g. Cooper et al. (2007); Elbaz et al. (2007); Hilton et al. (2010); Koyama et al. (2013)) since it's the epoch that early-type galaxies still form the bulk of stars (Rettura et al. 2010). However, several studies argue that there is no reversal of this relation at $z > 1$ (e.g. Bouché & Lowenthal (2005); Chartab et al. (2020); Darvish et al. (2016)) or show flattening of this relation (e.g. Bouché & Lowenthal (2005); Scoville et al. (2013)).

This contradiction of the SFR-density relation at $z > 1$ implies that we still do not have well-defined constraints on how the environment plays a part in galaxy quenching at high redshift. One

of the reasons this discrepancy emerge is due to the limited availability of galaxy spectroscopy to precisely determine the redshifts of galaxies, which is a crucial component in identifying the local environmental densities. Typically, for galaxies that lack spectroscopy, photometric redshifts (photoz) serve as an alternative method for estimating redshifts based on photometry. However, currently, the typical photometric redshift uncertainties of sources with spectroscopy are at about $|\Delta z| \approx 0.03(1+z)$ (Kodra et al. 2023). This level of precision is insufficient for creating accurate density maps and overdensity maps for studying environmental quenching. In fact, this uncertainty can be translated to the comoving distance of more than 100 Mpc at $z = 1$, which will dilute most structures in the extragalactic fields. As a result, more precise redshift measurements from spectroscopic redshifts (specz) are crucial for gaining a better understanding of the role of the environment on galaxy quenching. Therefore, our goal in this study is to improve density maps of galaxies using optical spectra from sources that lack spectroscopy in the CANDELS COSMOS, UDS, and EGS fields at redshift range $0.5 < z < 1.7$ at stellar mass $log(M*/M_{\odot}) > 10$.

1.3 Redshift Measurements of Galaxies

Creating density maps requires the three-dimensional positions of galaxies. While angular positions can be easily determined using the right ascension (RA) and declination (DEC), obtaining radial positions is much more challenging. Nevertheless, the current cosmological model provides the method to determine the radial distance to galaxies using redshifts.

Redshifts play a crucial role in the study of galaxy evolution for two purposes. Firstly, we can infer the radial distance to galaxies using redshifts based on the expansion of the universe. The greater the value of redshifts imply the greater distances to galaxies. Secondly, we can use redshifts to investigate the time evolution of galaxies. By examining the redshift, we can infer the lookback time of the galaxy, which is the time elapsed since the photons were emitted from the galaxy. As a result, we can also use the lookback time to study the past stages of galaxies.

Using the ΛCDM model, we can determine the comoving distance d_c and look back time t_L of galaxies using the formula as shown below (Mo et al. 2010).

$$d_c(z) = \frac{c}{H_0} \int_0^z \frac{dz'}{\sqrt{\Omega_r(1+z')^4 + \Omega_m(1+z')^3\Omega_k(1+z')^2 + \Omega_\Lambda}} \tag{1}$$

$$t_L(z) = \frac{1}{H_0} \int_0^z \frac{dz'}{(1+z')\sqrt{\Omega_r(1+z')^4 + \Omega_m(1+z')^3\Omega_k(1+z')^2 + \Omega_\Lambda}} \tag{2}$$

where H_0 is the Hubble constant, Ω_Λ is the dark energy density parameter, Ω_m is the matter density parameter, Ω_k is the spatial curvature density parameter, and Ω_r is the radiation density parameter.

Since redshifts play a central role in our understanding of how galaxies evolve over cosmic time, redshifts are the core element of galaxy evolution studies. Accurate redshift measurements help astronomers to place galaxies at correct distance and time, providing the means to study galaxy spatial distribution, and time evolution in a proper cosmological context. Hence, the improvement of redshift measurements will directly impact the reliability of our understanding of galaxy evolution.

There are two distinct methods to determine the redshift of galaxies. The first approach relies on analyzing the photometric data of galaxies in various wavelengths to construct the Spectral Energy Distribution (SED). Then, we perform the SED-fitting procedure to determine the redshift. The redshift obtained through this method is referred to as "photometric redshift" (photoz). Another method to determine redshifts involves directly measuring redshift from galaxy spectra. The redshift measured using this method is called "spectroscopic redshift" (specz).

1.3.1 Photometric Redshift

Photometric redshift (photoz) is the redshift obtained from broadband photometry and SED fitting. This method of redshift measurement is a quick and efficient method to approximate redshifts of a large number of galaxies. This approach utilizes the photometry data in various bands to generate the SED of an object. Subsequently, we fit a template constructed from spectroscopic redshifts of known objects to estimate the redshifts of the target galaxies.

This photoz technique is effective for measuring redshifts of a vast number of objects, including faint galaxies that are not feasible for obtaining spectra. However, the major drawback of this

method lies in its accuracy of redshift measurements. Due to its reliance on SED fitting, the current accuracy of photoz is still limited to approximately $\Delta z = 0.03(1 + z)$ (Kodra et al. 2023) which is insufficient for a precise mapping of large-scale structure.

1.3.2 Spectroscopic Redshift

Spectroscopic redshift (specz) is the redshift obtained through the conventional method of spectral analysis. This approach involves measuring the wavelength of various spectral features such as emission lines and absorption lines, and comparing them with their rest-frame wavelengths to obtain redshifts.

This method offers significantly higher precision in terms of redshift measurements since this approach is a direct measurement of redshifts from spectra. However, the main limitation of this method is that it is time-consuming since it requires the direct measurement of spectral features of each object, making it challenging to obtain the specz of a large number of objects. Additionally, the difficulty of obtaining spectra for faint objects, especially at high redshifts, makes this method challenging for faint sources.

Due to the different advantages and disadvantages of photoz and specz, astronomers often employ both methods to study galaxies. For objects with available specz, astronomers prioritize using specz due to their reliability for precise distance measurements. For objects without specz, photoz still serves as an alternative. The combination of photoz and specz allows astronomers to map the spatial positions of a large sample of galaxies effectively. Until the present day, obtaining more specz remains a crucial objective in galaxy evolution studies as they are important for investigating precise spatial density distribution, and serve as the benchmark for the calibration of photoz. The example of the comparison between using the photoz and specz from a sample of galaxies in the CANDELS COSMOS fields (Nayyeri et al. 2017) shown in Figure 4 indicates that specz and photoz do not always match. Hence, it is necessary to gather more specz to gain more precise distance measurements. Hence, our main objective of this research is to obtain more specz through the CHESS observing program.

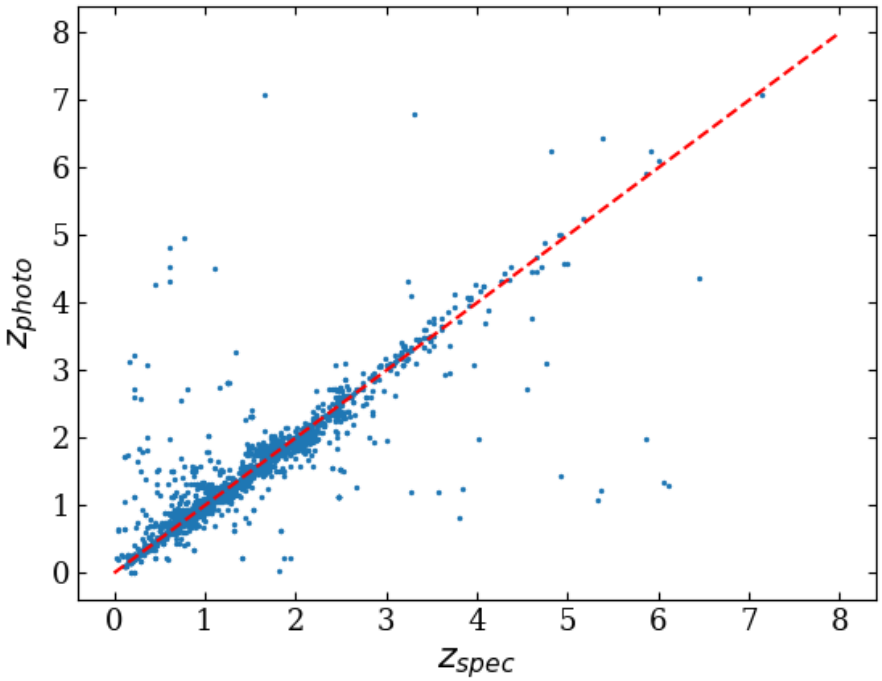

Figure 4: The comparison between photoz and specz comparison using the sample of galaxies in the CANDELS COSMOS fields (Nayyeri et al. 2017). The red dashed line shows the $z_{spec} = z_{photoz}$ trend. This plot shows that some photoz and specz still do not perfectly match one another, necessitating the need to obtain more specz to constrain the precision of photoz.

1.4 Galaxy Spectra

Galaxy spectra are the combination of spectra from all stars, nebula emission, dust, and Active Galactic Nuclei (AGN). By studying galaxy spectra, astronomers can gain insights into physical processes inside galaxies, such as compositions, dynamics, SFR, and properties of the interstellar medium (ISM) inside galaxies. Since our objective is to gather and analyze spectra from galaxies within the CANDELS fields, it is crucial to establish the fundamental spectral features of both star-forming and quiescent galaxies. This comprehension will aid the classification of our galaxy samples, and lead to the understanding of galaxy properties in all CANDELS fields.

1.4.1 Spectra of star-forming galaxies

Star-forming galaxies are galaxies that contain many short-lived O and B stars due to their active star formation. The Ultraviolet (UV) radiation emitted by these stars generates HII regions which are the source of nebula emission lines. Consequently, the spectra of star-forming galaxies can be identified using the emission features.

Within the Near-Infrared (NIR) filter, several emission lines are prominent including [OII] 3726, 3729, [OIII] 4959, 5007, Hβ, and Hα. These emission lines serve as indicators of their ongoing star formation process. Besides, The intensity of emission lines and emission line ratios can be used to determine the physical properties of these galaxies, including SFR, and electron temperature. Figure 5 shows the characteristic spectra of star-forming galaxies along with prominent emission lines.

1.4.2 Spectra of quiescent galaxies

Since quiescent galaxies lack ionizing radiation from O and B stars, they do not have clear emission lines in their spectra. Instead, quiescent galaxies display prominent absorption lines, which can be utilized to identify redshifts.

Some of the absorption lines present in quiescent galaxy spectra include Ca H, Ca K, G band, Mg I, and Na I lines. These absorption lines are the result of the combinations of absorption lines in stellar atmosphere. Furthermore, another prominent feature that can be observed in quiescent

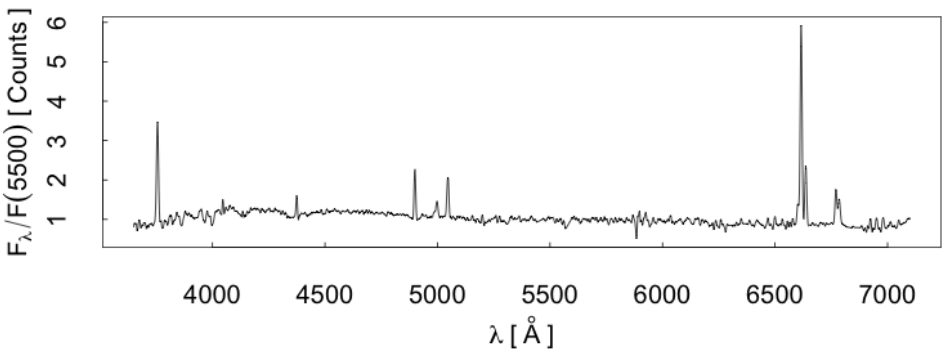

Figure 5: An example of a spectrum of a star-forming galaxy NGC 2276 excerpted from Kennicutt (1992). This spectrum shows the example of prominent emission lines that we can observe from star-forming galaxies including Hα, Hβ, Hγ, [OIII], and [OII].

galaxy spectra is the 4000 Åbreak, which arises from the combination of Balmer continuum absorption from stars and metal absorption lines. The 4000 Åbreak is another key feature to identify quiescent galaxy spectra. Figure 6 shows the rest frame spectra of quiescent galaxies.

The acquisition of quiescent galaxy spectra is crucial in our understanding of the connection between SFR and environmental density. The absence of prominent emission lines in these galaxies makes the measurements of specz considerably more challenging, leading to the bias toward specz measurements from star-forming galaxies. Therefore, the acquisition of specz from quiescent galaxies is one of the primary objectives of this research.

1.5 Quantifying Density

After obtaining both photoz and specz from galaxies, we can utilize both redshifts and angular coordinates to determine the local number density of galaxies. However, creating three-dimensional density maps of galaxies poses a critical complication due to the bias of specz and uncertainty of photoz (Darvish et al. 2015). Despite its reliability, specz introduces a bias since it is easier to acquire spectra from bright objects, skewing the density estimates toward these objects. On the other hand, photoz still carries an uncertainty of approximately $\delta z = 0.03$, which corresponds to

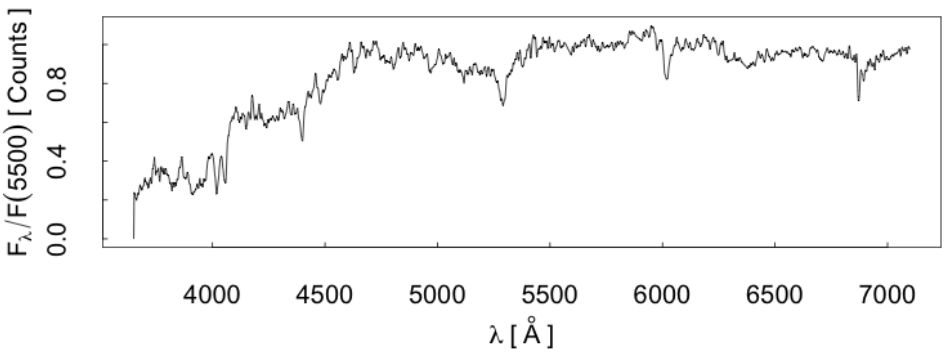

Figure 6: An example of a spectrum of a quiescent galaxy NGC 4486 excerpted from Kennicutt (1992). This spectrum shows the spectral features of quiescent galaxies including Ca K & H, G band, 4000 $\mathring{A}$ break, Mg I, and Na I absorption lines.

the length scale of 100 comoving Mpc which is larger than the typical size of structures such as galaxy clusters. To solve this issue, we narrow our focus from three-dimensional density estimation to the study of 2D surface density Σ. This process involves creating multiple slices in redshift space (z-slice) with the width based on the precision of photoz at that redshift range and the scale of the structure we want to capture. Moreover, each redshift slice has a half-bin overlap with the previous slice to include the contribution of galaxies near the boundaries of each z-slice.

After creating a map of 2D surface density Σ, we can compare the local Σ with the median value of the surface density of the entire map Σ_{median} to calculate the overdensity $(1+\delta)$ using the Eq. 3.

$$1 + \delta = \frac{\Sigma}{\Sigma_{median}} \tag{3}$$

Eq. 3 shows the variation of the local surface density from the median value. The positive values of $1+\delta$ indicate that the region is an overdense region, with an excess number of galaxies, while the negative values imply that the region is an underdense region with fewer galaxy densities. The quantification of the overdensity $1+\delta$ can help astronomers find structures such as galaxy clusters and voids

There are various methods that can be used to measure the 2D surface density of galaxies. In this study, we will introduce four different density estimation techniques based on the work of Darvish et al. (2015).

1.5.1 Weighted Adaptive Kernel Estimator

The Weighted Adaptive Kernel Estimator is the method of density estimation usually based on Gaussian Kernel smoothing as described in Breiman et al. (1977). To calculate the surface density of the field $\Sigma(r)$, we first estimate the surface density field around the i^{th} galaxy $\hat{\Sigma}_i$ using the positions of j^{th} galaxies ($j \neq i$) and applying the Gaussian Kernel to the i^{th} galaxy. The surface density field $\hat{\Sigma}_i$ can be calculated using Eq. 7 (Darvish et al. 2014).

$$\hat{\Sigma}_i = \frac{1}{\sum_{i=1}^{N} w_j} \sum_{i=1}^{N} w_i K(r, r_i, h) \tag{4}$$

where $K(r, r_i, h)$ is the Gaussian kernel defined as follow.

$$K(r, r_i, h) = \frac{1}{2\pi h^2} e^{-\frac{|r_i - r_j|^2}{2h^2}} \tag{5}$$

where h is the Kernel width, usually defined based on some physical scales such as the size of typical galaxy clusters and groups.

Upon obtaining the surface density associated with each galaxy, the next step involves calculating the surface density field $\Sigma(r)$ on a 2D grid. The resolution of this grid depends on the desired density calculation, typically within the range of 50 - 75 kpc. This is achieved by adapting the kernel width for each galaxy h_i based on the corresponding value of $\hat{\Sigma}_i$. The new Kernel width for each galaxy h_i is calculated based on the method by Silverman (1986) as follows:

$$h_i = h \times (G/\hat{\Sigma}_i(r_i))^{0.5} \tag{6}$$

where G is the geometric mean of all values of $\hat{\Sigma}_i$. After acquiring the kernel width from each galaxy, we can calculate the surface density field $\Sigma(r)$ by repeating the calculation in Eq.7, but

change the fixed kernel width h to adaptive width h_i as follows

$$\Sigma(r) = \frac{1}{\sum_{i=1}^{N} w_i} \sum_{i=1}^{N} w_i K(r, r_i, h_i) \tag{7}$$

The overdensity for each z-slice is then calculated using Eq.3 on a grid size defined in each calculation.

This density estimation method mitigates the effect of random clustering of foreground and background sources, as well as the influence of Poisson noise. However, the effectiveness and accuracy of this approach hinge on the selection of the global kernel size h. The small kernel tends to result in an overestimation of the density in regions populated by numerous galaxies, while a large kernel size smoothes out distinct overdensity features.

1.5.2 Weighted k-Nearest Neighbors (k-NN) Estimator

In this method, we use the inverse area containing the k^{th} nearest neighbors to each galaxy to estimate the local surface density. For the i^{th} galaxy, we can determine the surface density around it by counting the number and distance of neighboring galaxies until we reach the k^{th} nearest galaxy. The surface density of the i^{th} galaxy $\Sigma(r_i)$ can be determined using Eq. 8 (Darvish et al. 2015).

$$\Sigma(r_i) = \frac{\sum_{j=1}^{k} j w_{ij}}{\pi \sum_{j=1}^{k} w_{ij} d_{ij}^2} \tag{8}$$

where d_{ij} is the angular distance between galaxy i and j, and w_{ij} is the probability weight based on photoz.

This method is the fastest method out of the four in terms of computation time. However, this density estimation method can be greatly influenced by the chosen number of neighboring galaxies. If the number of neighboring galaxies is too small, the Poisson noise and random clustering of uncorrelated galaxies can significantly affect the density field. On the other hand, the large number of neighboring galaxies k can result in the oversmoothing of the galaxy distribution (Darvish et al. 2015).

1.5.3 Weighted Voronoi Tessellation

The Voronoi tessellation method is the density estimation method based on space segmentation, which involves dividing the z-slice into a series of non-overlapping polygons, known as the Voronoi cells, around each galaxy (nucleus). Each Voronoi cell represents the region of space closer to the nucleus than other neighboring galaxies (Icke & van de Weygaert 1987). The process of this space segmentation around a nucleus is shown in Figure 7.

In a dense region, many galaxies are clustered together, resulting in smaller Voronoi cells. On the other hand, the Voronoi cells tend to be larger in a less dense region. Therefore, we can use the area of Voronoi cells A_i to quantify the surface density of the i^{th} galaxy using the equation below.

$$\Sigma(r_i) = \frac{1}{A_i} \tag{9}$$

To smooth the density map and to create the weight for each galaxy, we need to find a systematic method to assign a weight for each galaxy. One common method is to use the Monte-Carlo acceptance-rejection process to select galaxies into each z-slice based on the photoz distribution. Using this method, we define a grid of any desired resolution on the redshift slice to be the region to assign the surface density value. Then, we randomly select galaxies from the photoz distribution and create Voronoi tessellation density maps from each z-slice. Then, this process is repeated N times to generate randomized density distribution from photoz of each galaxy. After N iterations, the median of the surface density value $\Sigma(r_i)$ is used as the final surface density that we assign to a point on a grid.

This method of density estimation is scale-independent, making it to be a versatile technique for identifying galaxy density over various ranges of physical scales. Furthermore, Unlike Adaptive Kernel Estimator and k-Nearest Neighbors Estimator, this method is non-parametric as it does not make any assumption on the morphology and structures of the density fields (Darvish et al. 2015). However, this method can be slow and computationally expensive due to the nature of the Monte Carlo technique. Nevertheless, this method is still superior compared to the first two methods.

1.5.4 Weighted Delaunay Triangulation

The weighted Delaunay triangulation serves as the density estimation technique based on space segmentation, which involves dividing the z-slice into triangles with galaxies as the vertices of these triangles. The triangulation is performed in a way that the circumcircle of these vertices does not overlap with any other neighboring galaxies (Darvish et al. 2015). Like Voronoi tessellation, in Delaunay triangulation, the area of triangles surrounding the galaxy is smaller for the denser region. Hence, we can use the area of neighboring triangles to identify the surface density. For example, if the i^{th} galaxy is surrounded by k surrounding triangles, the surface density can be calculated as follows.

$$\Sigma(r_i) = \sum_{j=1}^{k} \frac{1}{a_j} \tag{10}$$

where a_j is the area of the j^th triangle adjacent to the i^{th} galaxy.

To assign the weight to each galaxy, we can perform the Monte-Carlo acceptance-rejection process the same way as the weighted Voronoi tessellation method.

The Delaunay triangulation method shares both advantages and disadvantages with the Voronoi tessellation method. However, this method has the tendency to overestimate surface density in densely populated regions while underestimating it in less dense areas. For this reason, the Voronoi tessellation method is more widely accepted for density estimation. The comparison between space segmentation techniques using Voronoi tessellation and Delaunay triangulation is shown in Figure 7.

According to the simulation of various density estimation methods performed in Darvish et al. (2015), the adaptive kernel, k-NN, and Voronoi tessellation methods offer accurate surface density estimation in each z-slice. However, the Delaunay triangulation method tends to overestimate the density values in dense regions and underestimates the density in less dense regions. Additionally, while the k-NN method offers relatively higher computational efficiency, and the adaptive kernel method is less susceptible to shot noise, both methods rely on assumptions about the density structure of the z-slice. This reliance presents a challenge in density estimation across a broad

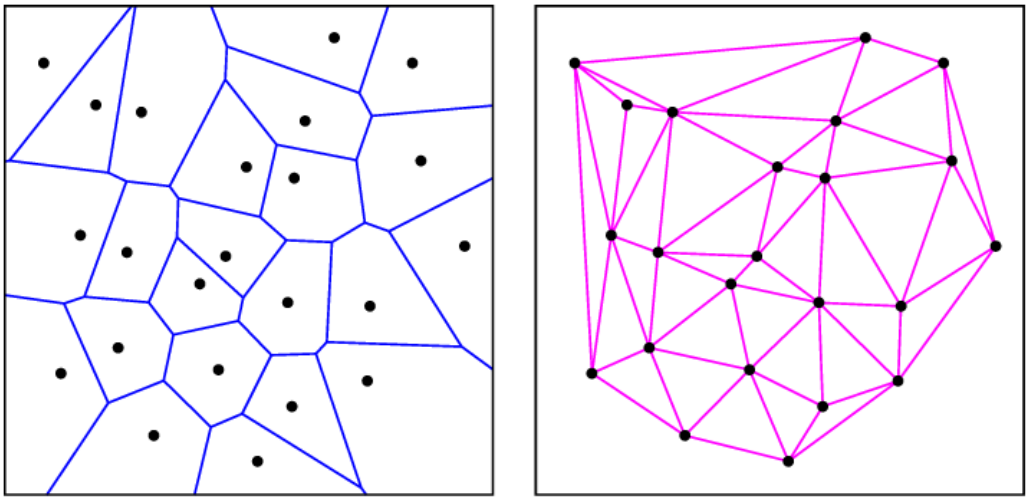

Figure 7: Comparison of two space segmentation techniques: Voronoi tessellation and Delaunay triangulation excerpted from Attali & Boissonnat (2004). Both methods can be used to determine surface density around random points on a 2D plane based on space segmentation. Voronoi tessellation (left) divides space into polygonal cells in a way that all points within a cell are closer to its nucleus than any other nuclei. Delaunay triangulation (right) connects three vertices (galaxies) in a way that no other galaxy exists within the circumcircle of these vertices. In both methods, surface density can be determined using the inverse area of Voronoi cells or Delaunay triangles.

range of scales. As a result, the Voronoi tessellation method remains suitable for our study due to its non-parametric and scale-independent nature despite its computational intensity. Therefore, we will focus on using the Voronoi tessellation technique to calculate the overdensity of our galaxy samples. The detailed analysis of the Voronoi tessellation technique will be in Chapter 4 of this thesis.

1.6 Measurements of the Star Formation Rates

The Star Formation Rate (SFR) is the measurement of the rate at which a galaxy creates new stars through the conversion of gas and dust into stellar mass. This parameter has a close relation with stellar mass and the gas reservoir of the galaxy. Hence, it is a parameter that can be used to track the galaxy formation and evolution, including the quenching processes (Boquien et al. 2014). SFR can be measured by various methods such as star counting, emission line diagnostics, and Spectral Energy Distribution (SED) fitting.

1.6.1 Star Counting

For resolved galaxies, SFR can be directly measured by counting the number of stars at different mass ranges or fitting isochrones to a color-magnitude diagram Kennicutt & Evans (2012). For galaxies at a distance further than the Magellanic Clouds, massive O-type stars, Wolf-Rayet stars, and the full color-magnitude diagram are used to measure SFR since individual low-mass stars cannot be resolved for those galaxies.

Since this study focuses on galaxies at intermediate redshift range out to $z \sim 1.7$, we need to focus on the SFR estimation methods based on the collective flux of galaxies. The review by Kennicutt (1998) summarizes multiple methods to approximate SFR from photometry of both emission line intensities, and SED continuum at different bands across the electromagnetic spectrum.

1.6.2 Emission Line Diagnostic

Star formation activities produce ionizing photons that induce the formation of HII regions inside galaxies. These HII regions give rise to emission line features within spectra. The intensity of emission lines, along with the intensity ratios of different emission lines can be used as a tracer for SFR. For example, Kennicutt et al. (1994) and Madau et al. (1998) have established the empirical relationships that allow the conversion of Hα flux into SFR for galaxies at solar metallicity and a Salpeter IMF spanning the range of 0.1-100 solar masses (Salpeter 1955). The relation can be expressed as follows:

$$SFR(M_{\odot} yr^{-1}) = 7.9 \times 10^{-42} L(H\alpha)\ (erg\ s^{-1}) \tag{11}$$

However, as the Hα line shifts out of the optical window at redshifts beyond $z > 0.5$, astronomers usually resort to using [OII] 3727 emission line to trace SFR. Astronomers use this line due to its brightness, its well-established calibration with a large sample of galaxies, and its observability in the optical band out to $z \sim 1.6$ (Kennicutt 1998). The SFR can be calculated from the [OII] line luminosity $L[OII]$ through Eq. 12.

$$SFR(M_\odot\, yr^{-1}) = (1.4 \pm 0.4) \times 10^{-41} L[OII]\, (erg\, s^{-1}) \tag{12}$$

1.6.3 Ultraviolet (UV) Continuum

The presence of massive, short-lived stars that emit primarily ultraviolet (UV) photons serves as an indicator of ongoing star formation. Hence, the UV continuum luminosity can be utilized to estimate the SFR. Using the ultraviolet (UV) continuum calibration from Madau et al. (1998) with Salpeter IMF spanning from stellar mass 0.1 to 100 solar masses, we obtain the relation between SFR and UV specific luminosity as follows:

$$SFR(M_\odot\, yr^{-1}) = 1.4 \times 10^{-28} L_\nu\, (ergs^{-1}\, Hz^{-1}) \tag{13}$$

1.6.4 Far-infrared (FIR) Continuum

Apart from using emission from stars and nebula to determine the SFR, we can also utilize the thermal infrared emission from dust to estimate the SFR. The UV photons from young stars can be absorbed by dust and re-emitted in the far-infrared (FIR) range. This physical process provides a reliable tracer for star formation activity. However, while this method is effective for dusty starburst galaxies, the FIR radiation from galaxies can also be influenced by AGN and older stellar populations (Kennicutt 1998). Using the model excerpted from Leitherer & Heckman (1995) with the Salpeter IMF, we obtain the relationship between SFR and FIR luminosity L_{FIR} for starburst galaxies as follows:

$$SFR(M_\odot\, yr^{-1}) = 4.5 \times 10^{-44} L_{FIR}\, (ergs^{-1} Hz^{-1}) \tag{14}$$

1.6.5 SED Fitting

Another approach to determine the SFR of galaxies involves utilizing broad-band photometric data. In this approach, we construct the spectral energy distribution (SED) of galaxies using data from photometric observations across different wavelengths. This SED provides insights into

various properties of galaxies, including SFRs, star formation histories (SFH), stellar metallicity, stellar initial mass function (IMF), AGN characteristics, and dust properties (Conroy 2013). By simulating various properties of galaxies, astronomers can identify the best-fitting model that aligns with the galaxy's SED, enabling the identification of galaxy properties, including the SFRs.

Several SED fitting codes are available for the determination of various galaxy properties. In our preliminary study, we use the SFR obtained through various SED fitting codes such as FAST, zphot, and SpeedyMC as shown in Nayyeri et al. (2017) because it's available across the entire photometric catalog used in this research.

2 CHESS Observations

To ensure that we have a diverse set of deep multiwavelength data, we need to study galaxies from extragalactic fields that already have deep multiwavelength data ranging from X-ray to radio. Over the past two decades, there have been numerous deep extragalactic surveys with various fields of view. Figure 8 shows a size comparison of various important extragalactic survey fields including the National Optical Astronomy Observatory (NOAO) Deep Wide Field (Jannuzi & Dey 1999), the Great Observatories Origin Deep Survey (GOODS) North and South fields, the Cosmic Evolution Survey (COSMOS) (Scoville et al. 2007), the UKIRT Infrared Deep Sky Survey (UKIDSSS) (Lawrence et al. 2007), the All-Wavelength Extended Groth Strip International Survey (AEGIS) (Davis et al. 2007), and many more (Madau & Dickinson 2014).

The extragalactic fields that best suit our study are the fields shown in the yellow boxes in Figure 8. These specific fields are a part of the Cosmic Assembly Near-Infrared Deep Extragalactic Legacy Survey (CANDELS) (PIs: Faber & Ferguson), which is a 902-orbit Hubble Space Telescope (HST) Multi-cycle Treasury (MCT) program that contains more than 250,000 galaxies over the redshift range from $z = 1.5$ to $z = 8.0$ (Grogin et al. 2011; Koekemoer et al. 2011). This survey is a two-tiered survey, encompassing both a wide survey in five distinct sight lines and a deep survey comprising two distinct sight lines (refer to section 2.1). The design of this survey allows us to address multiple science goals ranging from the exploration of the reionization era, the study of the peak of star formation, and the assessment of the rate of supernovae type Ia at high redshifts.

In this chapter, we discuss the brief summary of the CANDELS survey fields and delve into the details of the CHESS observing program including instruments, observing runs, and target selection. This detailed analysis explores the process of data acquisition for this study.

2.1 The CANDELS Fields

The CANDELS survey consists of two distinct survey depths: "CANDELS/Wide" and "CANDELS/Deep" (Grogin et al. 2011). The CANDELS/Wide field consists of five distinct fields including a portion of the Cosmic Evolution Survey (COSMOS) field, the Ultradeep Survey (UDS)

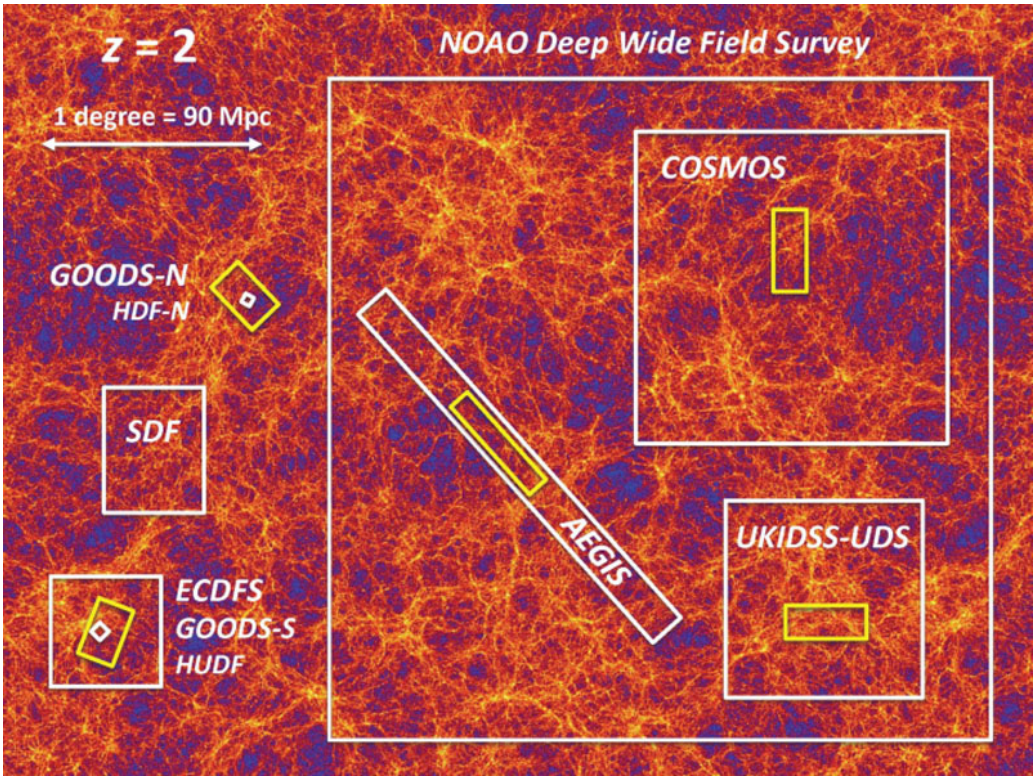

Figure 8: The diagram showing the angular sizes of different important extragalactic surveys derived from Madau & Dickinson (2014). This figure shows the many famous survey area including GOODS, SDF, AEGIS, COSMOS, UKIDSS-UDS, and NOAO Deep Wide Field Survey. Our research focuses on the CANDELS fields which are the yellow boxes embedded within these famous survey areas.

field, two Great Observatories Origin Deep Survey fields (GOODS-N and GOODS-S fields), and the Extended Groth Strip (EGS) field. The total area spanned by the CANDELS/Wide fields is approximately ~ 720 arcmin^2. On the other hand, the CANDELS/Deep fields cover the total area of ~ 130 arcmin^2 within the GOODS-N and GOODS-S fields.

In our study, we utilize the data from all five CANDELS fields, including COSMOS, UDS, EGS, GOODS-N, and GOODS-S, ensuring the diverse population of galaxies. The use of five separate fields reduces the impact of the mean density variation of matter, known as the cosmic variance (CV), due to the use of a larger volume of the universe (Grogin et al. 2011). Besides, the use of five separate fields also creates a statically robust dataset with stellar mass extending down to $10^9 M_{\odot}$, reaching out to redshifts $z \sim 2.5$ (Grogin et al. 2011).

Furthermore, the use of CANDELS fields holds significant importance for our study because these fields have the deepest far-IR data from Herschel (PIs: D. Elbaz, M. Dickinson) (Elbaz et al. 2011). The Herschel data allows us to obtain an unbiased measurement of SFR at high redshifts, given that most of the energy emitted by star-forming galaxies at high redshift is in the far-IR wavelength. Apart from the deep Herschel data, all five CANDELS fields also contain a large amount of multiwavelength photometric data from both space telescopes and ground-based telescopes ranging from X-ray to radio (see section 2.1.1 - 2.1.5). By combining the Herschel data with other multiwavelength observations, we can attain a comprehensive multiwavelength photometric dataset of galaxies for our studies.

Another reason that the CANDELS fields are useful for our study is that they already have a large amount of existing spectroscopy and publicly available redshifts. Since our objective is to increase the spectroscopic completeness of sources that lack spectroscopy, the existing photometric data, when combine with our newly obtained spectroscopic data, can be used to delve deeper into the study of galaxy properties as described in Chapter 1.

The five distinct lines of sight, a large set of multiwavelength data, and existing spectroscopic data make the CANDELS fields ideal to study the overall properties of galaxies including the relation between SFR and environmental density. The summary of the coordinates and sizes of the five extragalactic fields that we will use in our study is shown in Table 1.

Table 1: The summary of coordinates and field of views of CANDELS fields based on Grogin et al. (2011)

Field name	RA (hr)	DEC (deg)	Field of view (arcminutes^2)
COSMOS	10:00:27.92	+02:12:03.50	$9'.0 \times 22'.4$
UDS	02:17:37.50	-05:12:00.00	$9'.0' \times 22'.0$
EGS	14:19:18.00	+52:49:30.00	$6'.4 \times 30'.5$
GOODS-N	12:36:54.87	+62:14:18.86	$9'.7 \times 16'.4$
GOODS-S	03:32:29.46	-27:48:18.32	$9'.9 \times 14'.9$

2.1.1 COSMOS

The Cosmic Evolution Survey (COSMOS) is the largest extragalactic survey performed by the Hubble Space Telescope, with an area of 2 square degrees over the redshift range from $0.5 < z < 6.0$, making this survey ideally suited for the study of the evolution of Large Scale Structure (LSS), SFR, individual galaxies, and AGN Scoville et al. (2007). The CANDELS COSMOS fields is located at RA (J2000) = $10^h00^m28^s.92$, DEC (J2000) = $+02°12'03".50$ with the field of view of $9'.0 \times 22'.4$. This field has multiwavelength data throughout the electromagnetic spectrum including X-ray data from XMM-Newton (Hasinger et al. 2007), UV data from Galaxy Evolution Explorer (GALEX) (Zamojski et al. 2007), mid-IR data from Spitzer (Sanders et al. 2007), submillimeter data from the Caltech Submillimeter Observatory (Aguirre & Bolocam Galactic Plane Collaboration 2007), and radio data from the Very Large Array (VLA) (Schinnerer et al. 2004, 2007).

Furthermore, the COSMOS field also has optical and near-IR imaging from many ground-based telescopes such as optical data in deep Subaru/SuprimeCam in the B, g', V, r', i', and z' bands, and near-IR data from the Ultra-VISTA project (PI: J. Dunlop) in the Y, J, H, and K_s bands Grogin et al. (2011).

In addition to photometric data, the COSMOS field also contains spectroscopic data from various spectroscopic surveys including zCOSMOS (Lilly et al. 2007), PRIsm MUlti-object Survey (PRIMUS) (Coil et al. 2011), the Large Early Galaxy Astrophysics Census (LEGA-C) survey (van der Wel et al. 2021), the MOSFIRE Deep Evolution Field (MOSDEF) survey (Coil et al. 2015), 3D-HST (Momcheva et al. 2016) and many more.

2.1.2 UDS

The Ultra Deep Survey (UDS) field is the deepest sky region studied by the UKIDSS (Lawrence et al. 2007). The CANDELS UDS field is located at RA (J2000) = $02^h17^m37^s.50$, DEC (J2000) = $-05°12'00".00$, with a field of view of $9'.0 \times 22'.0$. This field contains multiwavelength photometric data from various surveys such as the Subaru/XMM-Newton Deep Survey (Sekiguchi et al. 2004), Spitzer Ultra-Deep Survey (PI: J. Dunlap), and the Spitzer Extended Deep Survey (SEDS) program (Ashby et al. 2013), and 1.4 GHz radio observations from the VLA (Simpson et al. 2006).

Furthermore, the UDS field also contains optical imaging in various bands including B, V, R, i, and z bands imaging using Subaru/SuprimeCam (Furusawa et al. 2008), observations in U-band using the MegaCam on the Canada-France-Hawaii Telescope (CFHT) (PI: O. Almaini), and deep J, H, and K imaging using the UKIRT Wide Field Camera (Grogin et al. 2011).

In addition to multiwavelength photometric data, the UDS field also contains spectroscopic data from various surveys including UDSz survey (Bradshaw et al. 2013), VANDELS (Garilli et al. 2021), 3D-HST (Momcheva et al. 2016), MOSDEF survey (Coil et al. 2015), and many more.

2.1.3 EGS

The Extended Groth Strip (EGS) field is a part of the region studied by the AEGIS survey field (Davis et al. 2007). This field is a long strip with an angular size of $6'.4 \times 30'.5$, centered at RA (J2000) = $14^h19^m18^s.00$, DEC (J2000) = $+52°49'30".00$. The CANDELS EGS field contains multiwavelength photometric data including X-ray data from Chandra ACIS observations with a 200 ks integration time (Laird et al. 2009; Nandra et al. 2015), UV observations from GALEX, IRAC and MIPS infrared observations using the Spitzer telescope (Ashby et al. 2013), and both 1.4 and 4.8 GHz radio observations from the VLA (Willner et al. 2006; Ivison et al. 2007).

Furthermore, the EGS field also contains optical and near-IR imaging from various bands including B-, R-, and I-band imaging from the CFHT 12K mosaic camera (Cuillandre et al. 2001; Coil et al. 2004), and J and K_s bands imaging from the Wide-Field Infrared Camera on the Palomar 5 m telescope (Grogin et al. 2011).

The spectroscopic survey included in the EGS field includes DEEP2 (Newman et al. 2013),

3D-HST (Momcheva et al. 2016), MOSDEF (Coil et al. 2015), and many more.

2.1.4 GOODS-N

The Great Observatories Origin Deep Survey fields (GOODS) are the two regions (GOODS-N and GOODS-S) on the sky that contain both CANDELS/Wide and CANDELS deep observations. The GOODS-N field is located in the northern part of the sky near the northern Hubble Deep Field (Williams et al. 1996). The center of the field is located at RA (J2000) = $12^h36^m54^s.87$, DEC (J2000) = $+62°14'18".86$. The angular size of this field is $9'.7 \times 16'.4$. This field contains various multiwavelength data from various surveys including the optical data from the GOODS Hubble Treasury Program in B, V, i, and z bands, IR data from the GOODS Spitzer Legacy Program in the IRAC 3.6, 4.5, 5.8, and 8.0 μm bands (Grogin et al. 2011), mid-IR data from the SEDS program (Ashby et al. 2013), X-ray data from Chandra observations with a total integration time of 2 Ms (Alexander et al. 2003), and 1.4 GHz deep radio observations from the VLA (Morrison et al. 2010).

In addition to multiwavelength data, this field also contains optical and near-IR imaging using ground-based telescopes such as U-band imaging from the MOSAIC camera on the KPNO Mayall 4m telescope (Capak et al. 2004), and near-IR imaging in the H K' band from the QUIRC camera on the University of Hawaii 2.2 m telescope (Capak et al. 2004).

Moreover, the GOODS-N field also contains spectroscopic information from various surveys such as MOSDEF (Coil et al. 2015), 3D-HST (Momcheva et al. 2016), MOIRCS Deep Survey (Yoshikawa et al. 2010), and many more.

2.1.5 GOODS-S

The GOODS-S is located in the southern region of the sky near the Chandra Deep Field (Giacconi et al. 2002). The center of the field is located at RA (J2000) = $03^h32^m29^s.46$, DEC (J2000) = $-27°48'18".32$. The angular size of the field is $9'.9 \times 14'.9$. The GOODS-S field contains multiwavelength data from various telescopes including the X-ray data from Chandra observations with an integration time of over 4Ms Grogin et al. (2011), optical data in the B, V, i, and z bands as a part of the GOODS Hubble Treasury Program (PI: M. Giavalisco), mid-IR data in the IRAC

3.6, 4.5, 5.8, and 8.0 mum from the GOODS Spitzer Legacy Program, Spitzer/IRAC (3.6-8.0 μm) from the SEDS program (Ashby et al. 2013), the Spitzer/MIPS (24 μm) from the Far-Infrared Deep Extragalactic Legacy Survey (FIDEL) (PI: M. Dickinson), submillimeter data from the LABOCA instrument on the Apex telescope (Weiß et al. 2009), and 1.4 and 4.8 GHz radio data from the VLA (Kellermann et al. 2008).

Furthermore, the GOODS-S field also contains the optical and near-IR data from ground-based telescopes including the U-band imaging from the Visible Multi-Object Spectrograph (VIMOS) on the Very Large Telescope (VLT) (Nonino et al. 2009), near-IR observations in the Y band using the HAWK-I (Castellano et al. 2010), and J, H, and K bands imaging with Infrared Spectrometer and Array Camera (ISAAC) on the VLT (Retzlaff et al. 2010).

In addition to photometric data, the GOODS-S field also contains spectroscopic data from various surveys including VANDELS (Garilli et al. 2021), 3D-HST (Momcheva et al. 2016), MOSDEF (Coil et al. 2015), Multi Unit Spectroscopic Explorer Wide (MUSE-Wide) survey (Urrutia et al. 2019), and many more.

2.2 CHESS Observing Program

Despite having the most diverse multiwavelength data ranging from X-ray to radio, the data in CANDELS fields cannot be used to fully investigate the impact of the environment on galaxy evolution due to insufficient spectroscopy in CANDELS COSMOS, UDS, and EGS fields. We quantify the spectroscopic completeness as the ratio between the number of sources with known spectroscopic redshifts and the total number of sources. The overall spectroscopic completeness in these three fields is approximately $\sim 60\%$ as shown in Figure 9. However, the study of mock catalogs from the ORELSE survey by Hung et al. (2019) underscores that to effectively detect large-scale structures, the level of spectroscopic completeness of around 80% is necessary.

To rectify this limitation, we introduce the CANDELS-Herschel Environmental Spectroscopic Survey (CHESS), which is the completed multi-semester Keck DEIMOS observing program that focuses on collecting spectra from galaxies in CANDELS COSMOS, UDS, and EGS fields to increase the level of spectroscopic completeness for massive galaxies at $0.5 < z < 1.7$ (PI: J. Kartaltepe). In

this study, we aim to reach $\sim 85\%$ completeness at I magnitude of $I < 24$ to identify all overdensity structures.

The CHESS observations took place from 2020 to 2022 over 7 nights, covering a total area of approximately 600 arcmin^2 with 21 masks. By combining our spectroscopic survey with the existing spectroscopy in these fields, plus the GOODS data, we aim to obtain an intensive spectroscopic sampling of the local density field across five distinct extragalactic fields with data from HST, Herschel, and Spitzer observations. This program allows us to investigate the evolution of the total SFR activity and morphological transformation across diverse environments for the first time.

For the CHESS observing program, the author of this thesis participated in four nights of observing runs, including November 29th, 2021, January 7th, 2022, February 27th, 2022, and March 29th, 2022. Furthermore, the author of this thesis was responsible for the data reduction process, the coordination of specz measurements, and the stacking of spectra. The in-depth processes of these tasks are elaborated on in the subsequent sections of this thesis.

The objective of CHESS is to investigate the relationship between SFR and the environmental density of galaxies at $0.5 < z < 1.7$. This redshift range covers the peak and the drop of the cosmic star formation rate density and has prominent emission lines in the optical part of the spectrum. However, at this redshift range, there is a potential for the selection bias of galaxies as obtaining data from faint galaxies becomes more difficult at intermediate redshift as shown in the distribution of stellar masses as a function of photoz in Figure 10. This figure shows that the galaxies at stellar mass $M^* > 10^{10}$ solar masses maintain 90% completeness until the redshift of around $z \approx 2.5$. Hence, we conclude that selecting galaxies with $M^* > 10^{10}$ solar masses will ensure a full spectroscopic sampling at our redshift range of $0.5 < z < 1.7$. Selection of galaxies at this stellar mass range not only enhances the reliability of the sampling of galaxies, but this mass range also allows us to select galaxies that are the main contributors to the cosmic SFR density at $z > 0.5$ (Heavens et al. 2004; Gruppioni et al. 2013).

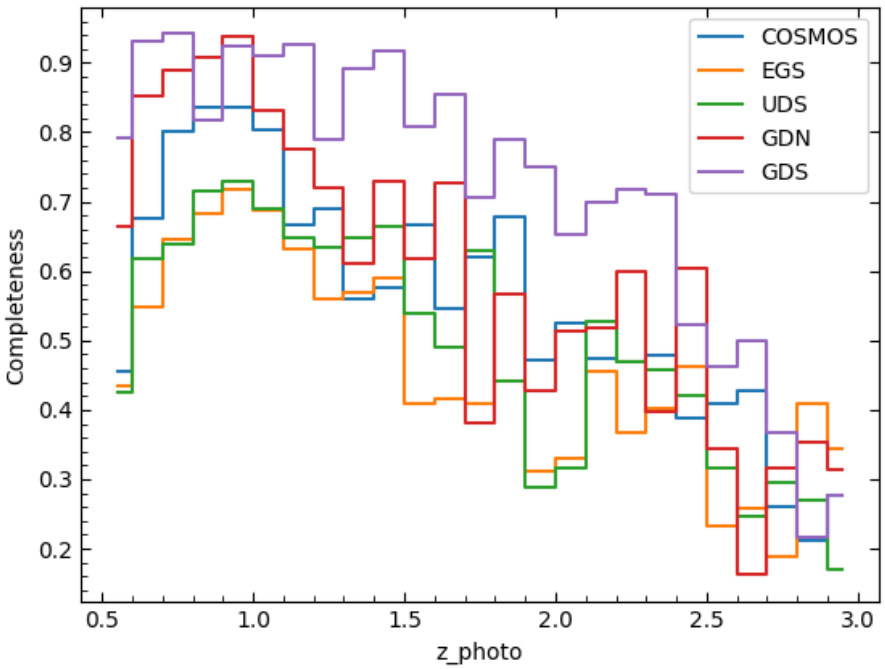

Figure 9: Spectroscopic completeness of all five CANDELS fields for galaxies with stellar mass $M^* > 10^{10}$ solar masses. This plot demonstrates that the CANDELS COSMOS, UDS, and EGS fields exhibit relatively lower spectroscopic completeness for massive galaxies at the redshift range $0.5 < z < 1.7$ compared to the GOODS-N, and GOODS-S fields. This disparity in spectroscopic completeness motivates the creation of the CHESS spectroscopic catalog.

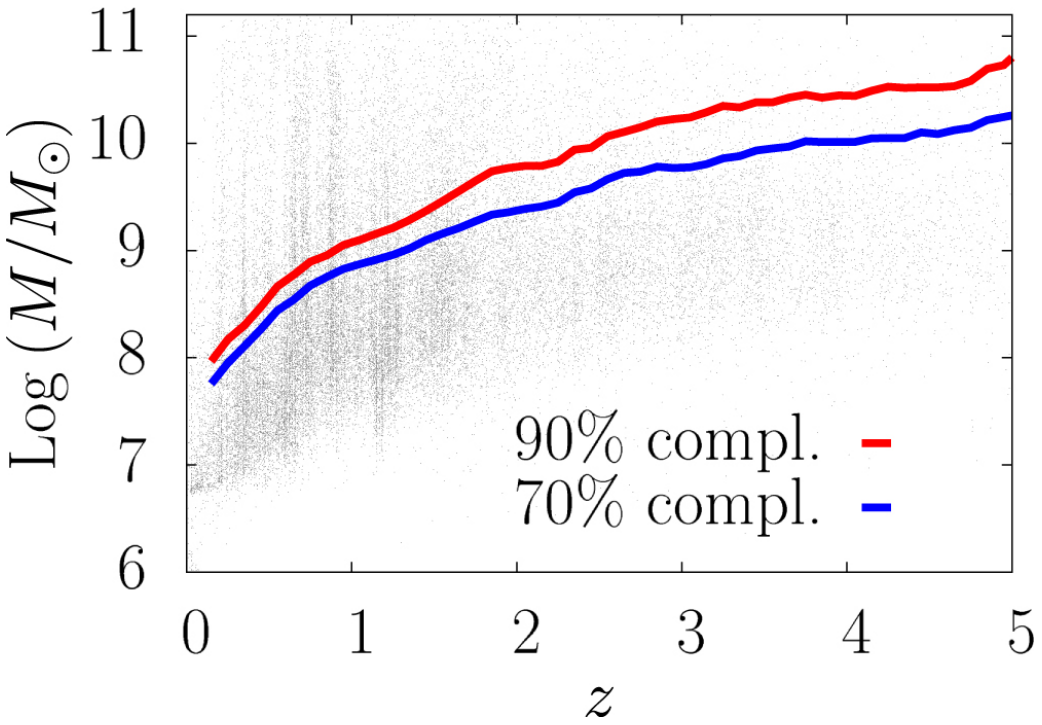

Figure 10: The stellar mass distribution as a function of redshift, excerpted from the work of Nayyeri et al. (2017). This plot shows the stellar mass from a galaxy sample within the CANDELS COSMOS field. The red and blue lines represent the 90% and 70% completeness limits. These limits are defined as the mass limit that 90% (or 70%) of galaxies can be observed without being missed in the low-mass end of the mass distribution.

2.2.1 Instruments

The CHESS observing program aims to acquire optical spectra from approximately 1400 Herschel-selected galaxies in CANDELS COSMOS, UDS, and EGS fields that have stellar mass $M* > 10^{10}$ solar masses at the redshift range $0.5 < z < 1.7$. These galaxies are selected from the total area of 600 arcmin^2 in all three target fields. To accomplish this task, we need a telescope located at the location that can observe all three distinct fields effectively. Furthermore, that telescope needs to be large enough to be able to obtain spectra of faint galaxies ($I \sim 24$) with a reliable signal-to-noise ratio. The observatory that matches these criteria is the W.M. Keck Observatory in Hawaii due to its location near the equator, and its two 10-meter telescopes.

Another reason that makes the Keck Observatory suitable for this program is the DEep Imaging Multi-Object Spectrograph (DEIMOS, PI: S. Faber) instrument on the Keck II telescope due to its multiplexing ability that allows 80-150 slits per mask with the field of view of $16'.7 \times 4'$ (Faber et al. 2003). The 600 l/mm grating with a slit size of 1" also enables us to obtain the wavelength coverage of $0.5 - 1.0$ μm with a 0.65 Å per pixel dispersion and spectral resolution of 4.6 Å. This wavelength coverage allows the simultaneous observation of the combination of [OII] doublet at 3726 and 3729 Å, [OIII] doublet at 4959 and 5007 Å, and Hβ emission lines to fall on the spectra, enabling us to identify star-forming galaxies at our target redshift range of $0.5 < z < 1.7$.

In addition, the DEIMOS instrument also enables the observation of various absorption features within our target redshift range, including Ca H and K, G-band, MgI, NaI, and 4000 Å break. These absorption features provide insights into massive quiescent galaxies—a primary focus of the CHESS observing program. These lower SFR systems are often challenging to detect and necessitate deep spectra to identify absorption lines. The exclusion of these quiescent galaxies could introduce a bias toward sources with higher SFRs. Hence, the Keck DEIMOS capability to detect absorption lines from quiescent galaxies is crucial for the comprehensiveness of our galaxy sample.

The spectral features from our observations are detected and recorded using the DEIMOS science detector, which is the detector mosaic comprised of 8 separate CCDs. Figure 11 shows the CCD mosaic that consists of two modes: Direct and Spectral readout modes. In the direct mode, only

the CCDs at the bottom row (CCD1-CCD4) are used for imaging. In the spectral mode, all eight CCDs are used for reading spectra from the slitmask (Faber et al. 2003). Each DEIMOS spectrum spans the length of two CCDs. The CCDs that detect the short wavelength wing of the spectrum (blue) are annotated as CCD1, CCD2, CCD3, and CCd4. On the other hand, the CCDs that detect the long wavelength wing of the spectrum (red) are annotated as CCD5, CCD6, CCD7, and CCD8.

To gather spectra, DEIMOS CCDs are covered by a slitmask which comprises 80-150 slits that aligns with the position of target galaxies. The slitmask is aligned using the help of alignment stars, allowing accurate positioning of sources on slits. The example of DEIMOS slitmask is shown in Figure 12.

Although the DEIMOS instrument is a suitable instrument for this study, there is an issue with DEIMOS CCD5 that emerged in February 2020 that affects the quality of our acquired data substantially. During the time of the CHESS program, CCD5 displayed a bias-like response when exposed to photons as documented in Figure 13. This issue affects all spectra in slits placed on the CCD5. This positioning renders the spectra on the blue wing, which corresponds to the location of CCD5, susceptible to bias-like noise as shown in the SpecPro software (Masters & Capak 2011) display in Figure 14. This issue affects $\sim 24\%$ of the total spectra on a slitmask. Some spectral features of the objects with this issue can still be identified on the red side of the spectrum, but they would have to be bright sources.

2.2.2 Target Selection and slitmask design

Our primary objective is to gather spectra of galaxies with known photometric redshifts, but without existing spectroscopic redshifts at the redshift range $0.5 < z < 1.7$. To ensure that we include all the main contributors to the cosmic SFR density up to $z \approx 1.7$ while maintaining unbiased spectroscopic sampling, we prioritize galaxies with stellar mass $M* > 10^{10}$ solar masses. To fill up the remaining slits in each mask, we insert filler targets into our slitmask which consists of additional Herschel-selected sources, high-z sources with Ly-α line that falls in the DEIMOS wavelength range, lower-mass photoz selected sources, and galaxy pair candidates.

Throughout our two-year observing program, we want to cover the full area of all target fields

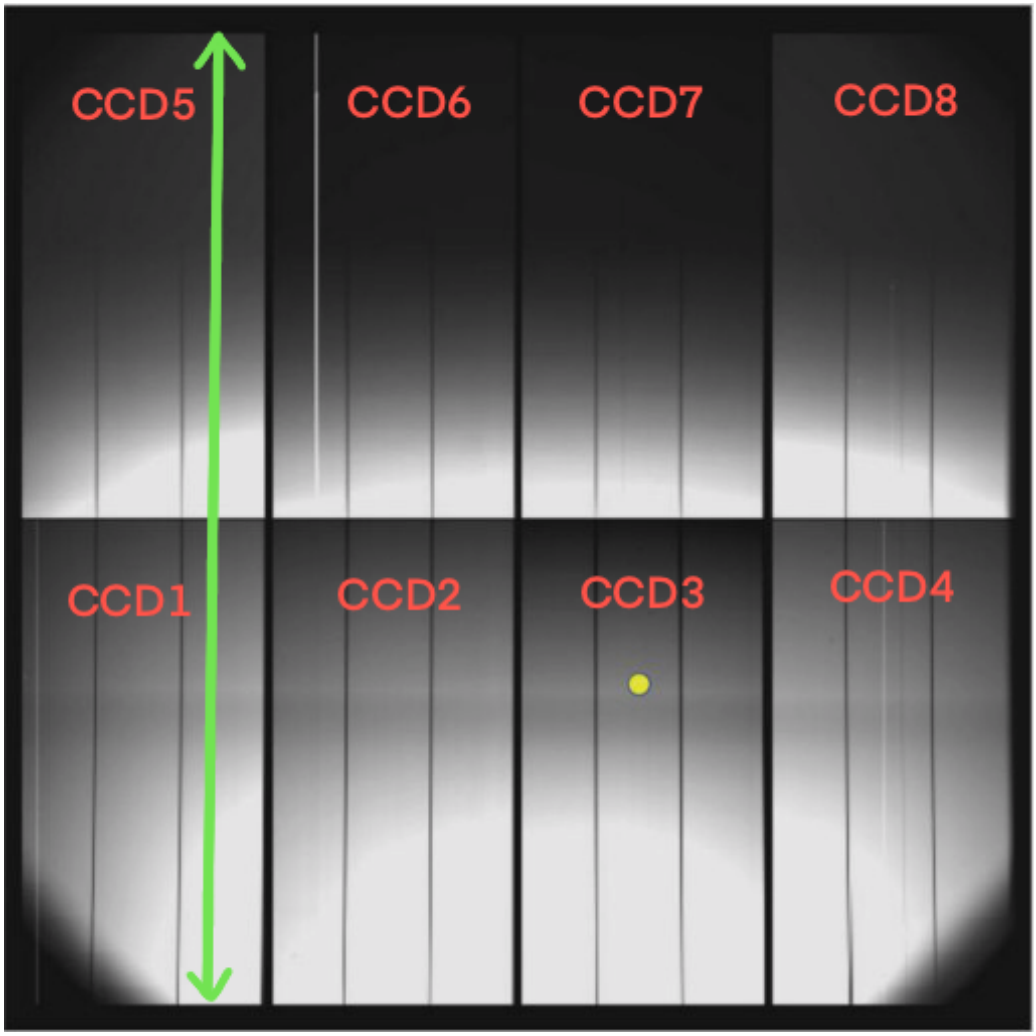

Figure 11: The flat image showing the layout of all 8 DEIMOS CCDs. The green arrow shows how a spectrum can be placed on the CCD. CCD 1-4 represents the blue wing of the spectrum and CCD 5-8 represents the red wing of the spectrum. Image credit: W.M. Keck Observatory

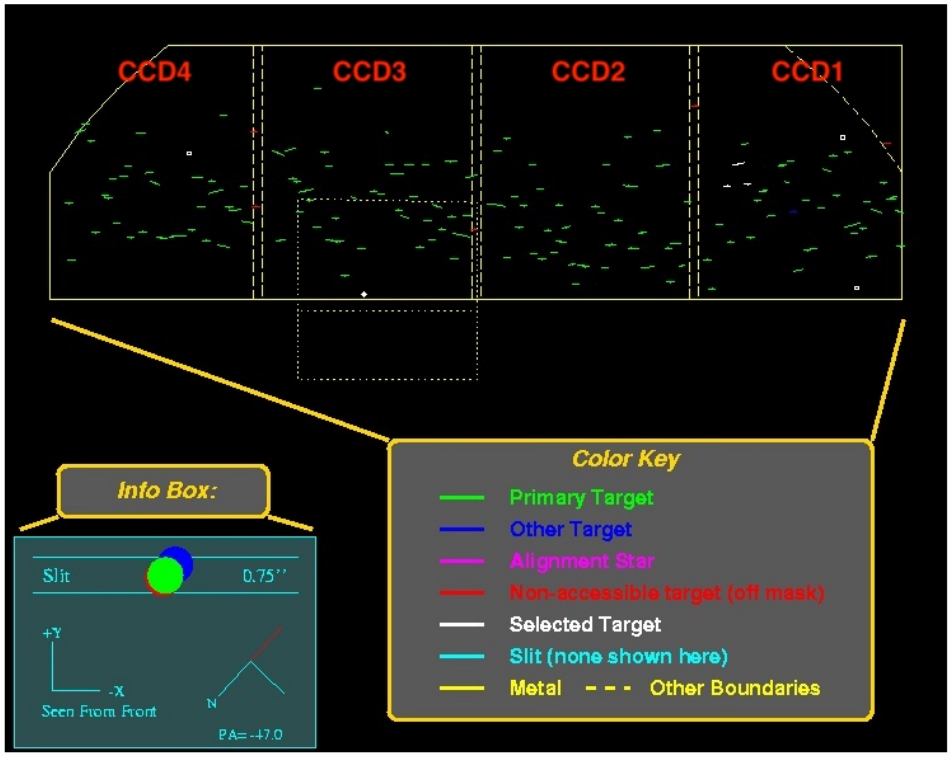

Figure 12: The slitmask on CCD1 to CCD4, which are direct-mode CCDs. This detector layout is rotated 180° from the detector layout shown in Figure 11. The slit in green shows the position of the slitmask of the primary target. The alignment stars are shown in the white boxes. Image credit: W.M. Keck Observatory

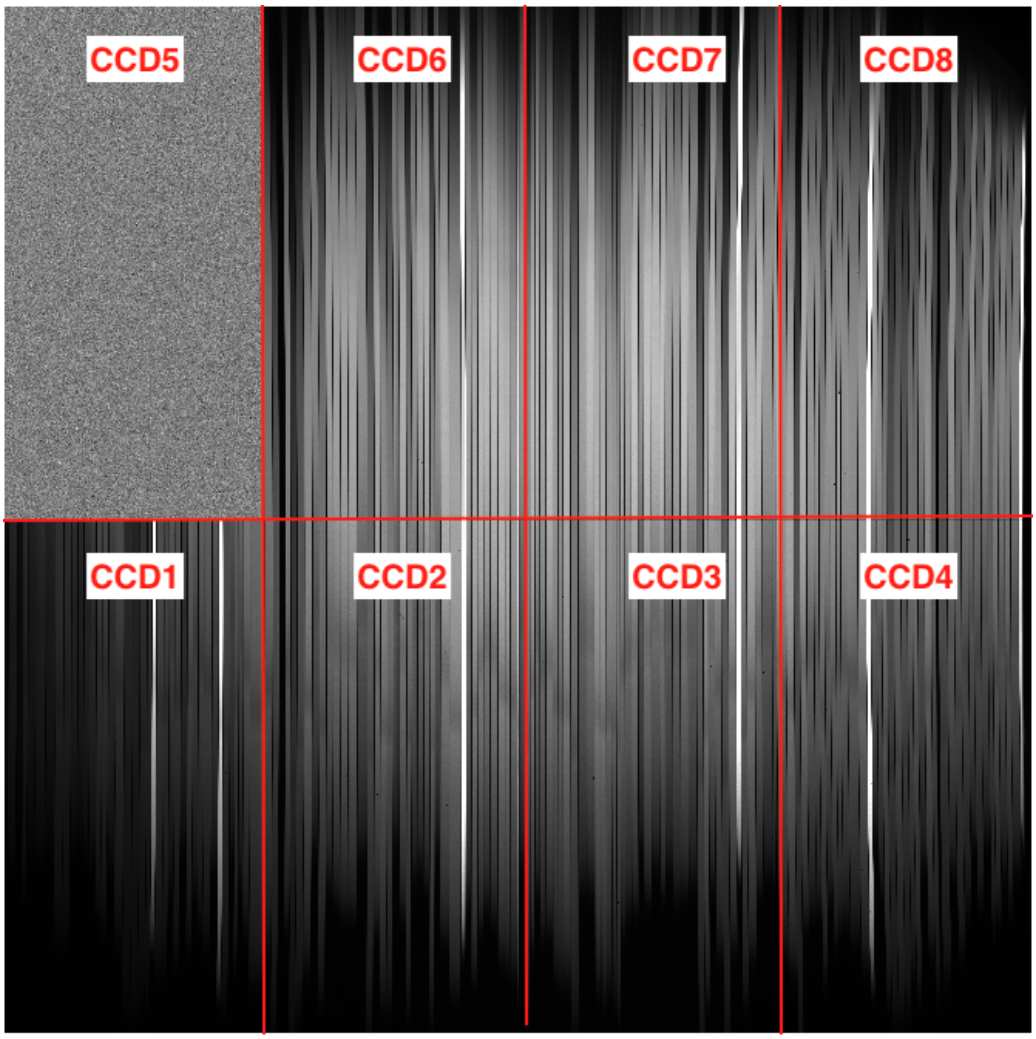

Figure 13: The mosaic image of a spectral flat taken by the DEIMOS instrument with a slitmask installed. This flat image shows an issue with CCD5 that emerged in February 2020. Image credit: W.M. Keck Observatory.

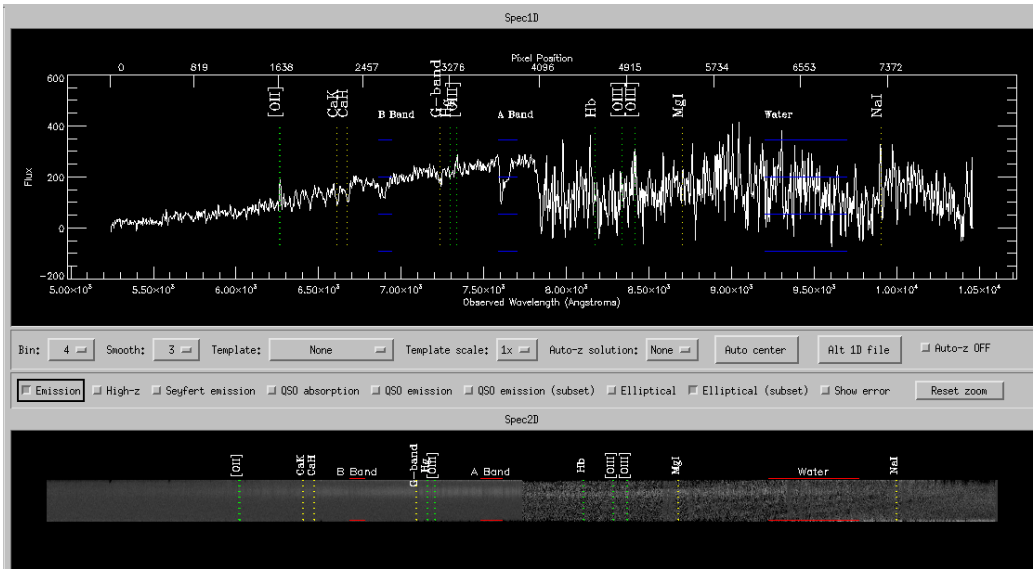

Figure 14: The effect of a bad CCD on the quality of a spectrum in the red wing depicted in the software SpecPro (Masters & Capak 2011). The red wing of the spectrum shown in this figure is placed on CCD5, resulting in the noise on the right-hand side.

as much as possible. Furthermore, we also want to observe faint sources multiple times to increase the total exposure time and thus the total signal-to-noise ratio for these sources. Considering the DEIMOS field of view of $16'.7 \times 4'$, each field requires multiple masks to cover the total area. The CANDELS COSMOS and UDS fields, subtending $9' \times 22'$, can be covered completely using 6 masks with overlapping regions between them. Similarly, the CANDELS EGS field with the area of $6' \times 30'$ can be covered with 4 masks. For the final observation, the COSMOS field is observed using 11 masks. The UDS field is observed using 7 masks. Unfortunately, due to adverse weather conditions, the EGS field is observed using only 3 masks instead of the planned 4 masks. The overlays of slitmasks on the HST mosaic of the three target CANDELS fields (Grogin et al. 2011; Koekemoer et al. 2011) are also depicted in Figure 15, 16, and 17.

2.2.3 CHESS Observing Runs

The CHESS observing runs were scheduled for a total of 10 nights spanning from 2020 to 2022. The dates for these scheduled observations are listed as follows: 28-Feb-2020, 27-Mar-2020, 11-Dec-2020, 18-Jan-2021, 15-Feb-2021, 06-Mar-2021, 29-Mar-2021, 08-Jan-2022, 27-Feb-2022, and 29-Mar-2022. However, the acquisition of the CHESS spectra was accomplished from only 7 nights of observations.

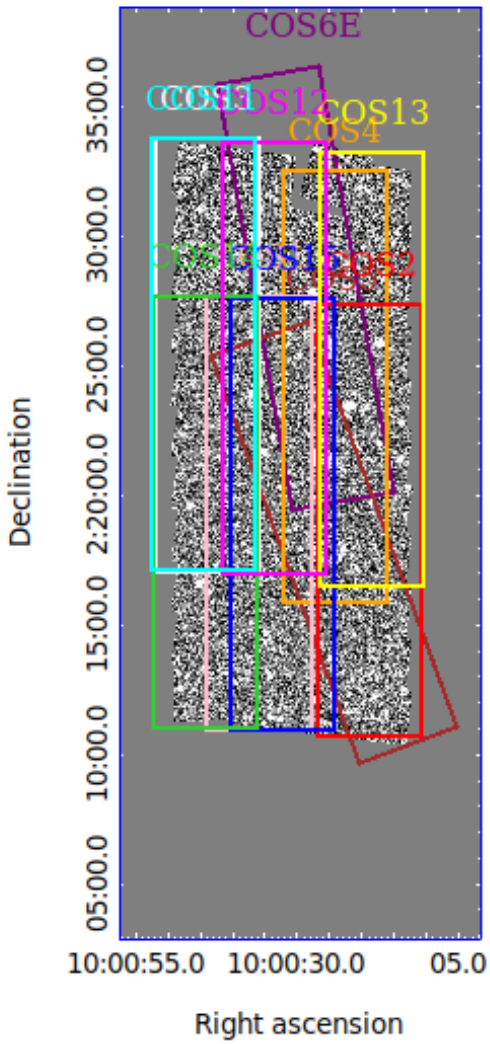

Figure 15: The layout of all 11 slitmasks of the COSMOS fields on top of the HST WFC F160W mosaic image (Grogin et al. 2011; Koekemoer et al. 2011).

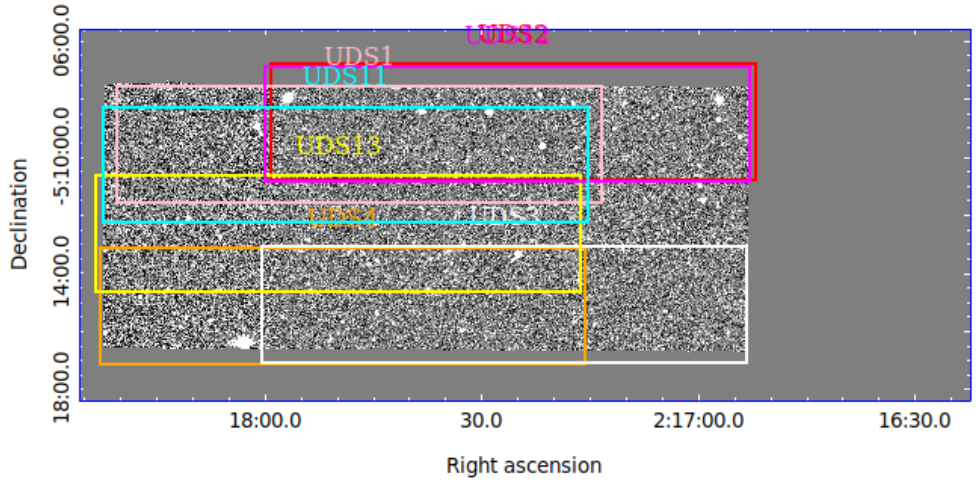

Figure 16: The layout of all 7 slitmasks of the UDS fields on top of the HST WFC F160W mosaic image (Grogin et al. 2011; Koekemoer et al. 2011).

Two of the planned runs (28-Feb-2020 and 29-Mar-2022) were aborted due to weather. Moreover, the observing run on 27-Mar-2020 was canceled due to the COVID-19 pandemic. The author of this thesis contributed to the CHESS observations during the four observing runs 29-Mar-2021, 08-Jan-2022, 27-Feb-2022, and 29-Mar-2022.

Since the period of the CHESS observing runs coincided with the global COVID-19 pandemic, the observing runs were conducted remotely to ensure safety. During these remote observing runs, we established multiple video calls with telescope operators at the W.M. Keck Observatory. The telescope was controlled using the Keck Virtual Network Computing (VNC) software.

Before the start of each observing run, we followed multiple many systematic procedures to ensure the correct calibrations of the telescope and DEIMOS instrument. Firstly, we took bias frames to calibrate readout noise. Then, we performed a focus check by generating a focus map and aligning the telescope's focus. Subsequently, wavelength calibration was accomplished by imaging known spectra of calibration lamps. Then, we proceeded to take flat frames to calibrate the effects of the vignette, sensitivity of CCDs, and telescope artifacts.

After performing these procedures, we aligned the slitmask to the target field using alignment stars. To ensure a sufficient signal-to-noise ratio, each source requires a minimum exposure time of

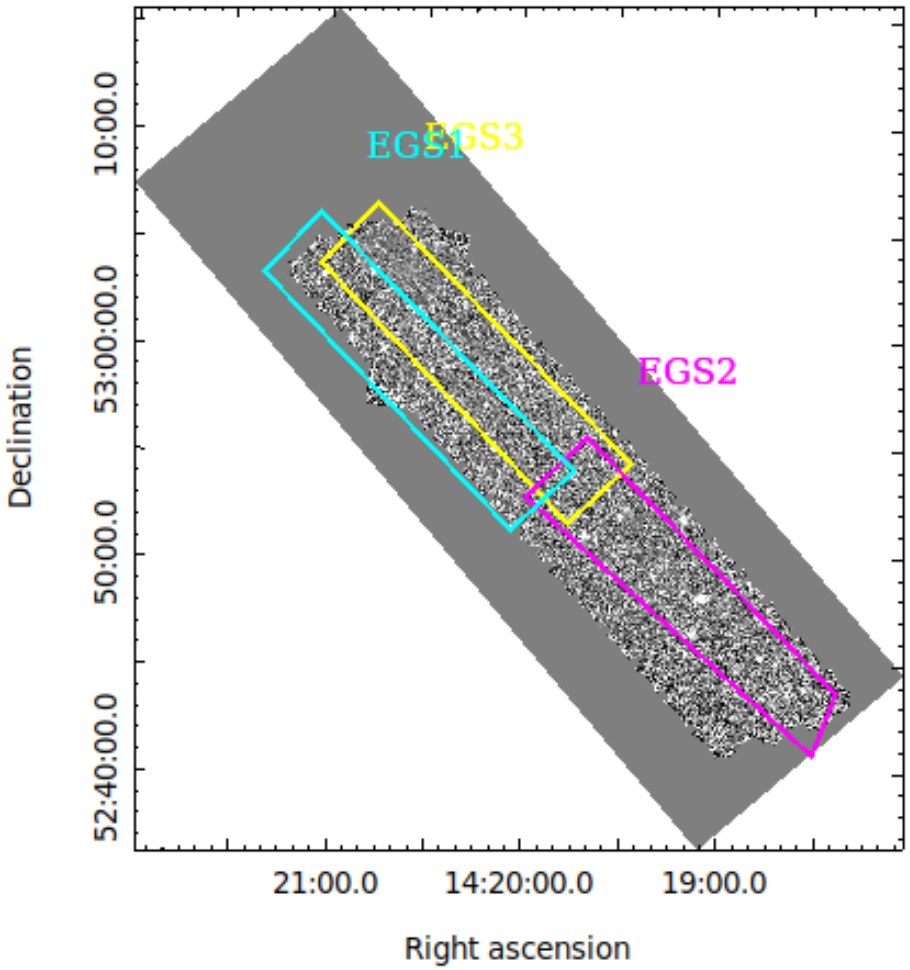

Figure 17: The layout of 3 out of 4 observed slitmasks of the EGS fields on top of the HST WFC F160W mosaic image (Grogin et al. 2011; Koekemoer et al. 2011).

120 minutes. For fainter objects, we use the strategy involving placing objects in the overlapping regions between slitmasks to have multiple observations. Then, we stack the images to achieve a higher total integration time. By using this technique, the deepest observations can have a maximum exposure time of up to 12 hours, allowing us to reach a high level of completeness at the faint end ($I > 24$). In each observing run, we observed 2-5 slitmasks depending on the weather conditions. After a total of 7 successful observing runs, we obtain spectra from 11 slitmasks in the COSMOS field, 7 slitmasks in the UDS field, and 3 slitmasks in the EGS field. Table 2 shows the summary of all CHESS observations including the date of observation, mask name, center coordinates (RA, DEC), number of sources observed, and exposure time.

Table 2: The summary of the CHESS observations including the details about slitmasks and spectroscopic sources. The dates with asterisk are the dates with poor weather.

Date of observation	Mask name	RA (hr)	DEC (deg)	Number of sources	Exposure time (s)
11-Dec-2020	COS1	10:00:35.63	+02:19:15.4	145	8922
11-Dec-2020	COS2	10:00:18.42	+02:18:57.4	144	4800
11-Dec-2020	UDS1	02:17:46.740	-05:09:37.5	144	7200
11-Dec-2020	UDS2	02:17:25.45	-05:08:49.5	138	7200
11-Dec-2020	UDS3	02:17:26.66	-05:15:07.6	143	3150
18-Jan-2021	COS3	10:00:43.64	+02:25:21.5	146	9301
18-Jan-2021	COS4	10:00:23.94	+02:24:09.5	150	7200
18-Jan-2021	COS5	10:00:24.28	+02:18:11.6	153	6000
18-Jan-2021	UDS4	02:17:49.15	-05:15:10.0	141	6600
15-Feb-2021	COS1	10:00:35.63	+02:19:15.4	145	2345
15-Feb-2021	COS3	10:00:43.64	+02:25:21.5	146	7200
15-Feb-2021	COS6E	10:00:28.67	+02:27:59.4	133	7200
6-Mar-2021	COS5	10:00:24.28	+02:18:11.6	153	7200
6-Mar-2021	EGS1	14:20:32.07	+52:58:39.8	145	7200
6-Mar-2021	EGS2	14:19:10.79	+52:48:15.8	152	8400
29-Nov-2021*	COS12	10:00:33.34	+02:25:11.3	137	1200
29-Nov-2021*	UDS11	02:17:48.70	-05:10:18.5	154	14496
8-Jan-2022	COS11	10:00:44.31	+02:25:24.2	137	10800
8-Jan-2022	COS12	10:00:33.34	+02:25:14.5	137	12000
8-Jan-2022	UDS12	02:17:26.29	-05:08:54.2	149	7200
8-Jan-2022	UDS13	02:17:49.69	-05:12:39.5	149	3600
27-Feb-2022	COS13	10:00:18.18	+02:24:48.8	152	7200
27-Feb-2022	COS14	10:00:43.95	+02:19:16.9	153	7200
27-Feb-2022	COS15	10:00:31.90	+02:19:11.9	146	7200
27-Feb-2022	EGS3	14:20:14.48	+52:59:04.2	157	7927

3 Making the Spectroscopic Redshift Catalog

From the CHESS observations, we obtain data as the combination of all spectra in a slitmask, as shown in Figure 18. However, this initial dataset contains sky lines and cosmic ray artifacts and is not yet wavelength calibrated. To obtain individual reduced and calibrated spectra from this raw image, the author of this thesis uses the DEEP2 DEIMOS data reduction pipeline (Cooper et al. 2012) to clean and combine science frames and perform wavelength calibration. Then, we inspect the reduced spectra to identify all spectroscopic features for redshift measurements. In this chapter, we describe the process of data reduction, redshift measurements, and finalizing the CHESS spectroscopic redshift catalog.

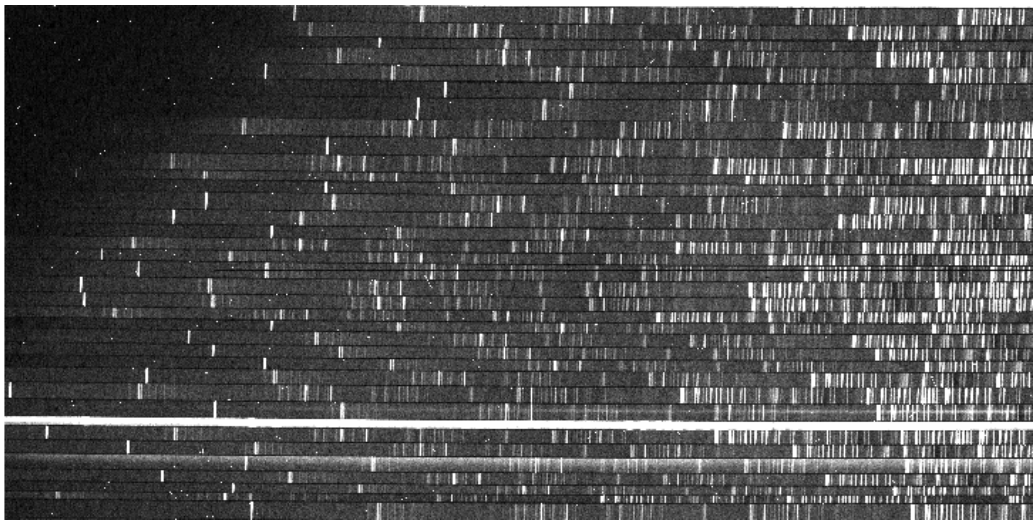

Figure 18: Raw science frame from COS1 slitmask. This image is rotated 270° from its ds9 image display orientation. Bright vertical lines shown in this image are atmospheric sky lines. Additionally, the short streak of light on the science frame indicates the cosmic ray artifacts. These artifacts need to be subtracted from the raw image before specz measurements can be performed. One bright row in this image is one of the alignment stars used for slitmask alignment.

3.1 DEEP2 DEIMOS Data Reduction Pipeline

The DEEP2 DEIMOS Data Reduction Pipeline (spec2d) is an IDL-based script for reducing data obtained from the DEIMOS instrument on the Keck telescope (Cooper et al. 2012). This software was originally developed as a part of the DEEP2 survey (Newman et al. 2013). The pipeline runs in five distinct stages that generate its own output files: `calibSlit`, `DEIMOS_MASK_CALIBRATE`, `DEIMOS_2DREDUCE`, `SPSLIT_COMBINE`, and `EXTRACT1D`.

3.1.1 Data Reduction Preparation

The data reduction process starts by generating a text file with the extension .plan called the `"planfile."` This file defines all necessary files for data reduction including flat frames, arc frames, and science frames, thereby laying the groundwork for data reduction.

In the next step, the data reduction pipeline reads each of the 8 DEIMOS CCDs independently by utilizing flat frames and arc frames to create `calibSlit files.` These `calibSlit` files contain critical information for analysis including flat frame information, 2-d wavelength solution, and the distribution of slitlets on the CCD array (Newman et al. 2013).

After creating the `calibSlit` files, the DEEP2 pipeline cross-correlates the position of each pixel with the wavelength values by applying optical models to arc frames. The pipeline models the relation between wavelength values and pixel positions as Legendre polynomials of up to fifth order. Then, the pipeline applies linear regression to find these Legendre polynomial coefficients. This method yields a wavelength solution with the precision of 0.007 $\mathring{A}$ RMS level. This level of precision is necessary because the accurate OH-line subtraction of this pipeline requires errors below ~ 0.01 $\mathring{A}$ RMS (Newman et al. 2013).

In the subsequent step of data reduction, the pipeline generates the inverse-variance image based on the photon read noise and bad pixel maps. The maps of a bad pixel contain information about the imperfect corrections of vignetting and cosmic rays, resulting in a non-zero value of inverse variance. These maps serve as flag information about the quality of each pixel.

3.1.2 Sky Subtraction

After obtaining the `calibSlit` files and flag information, the pipeline performs the sky subtraction process. The sky subtraction can be done by the calculation of the sky background level including bright OH lines as a function of pixel position and wavelength. To determine the wavelength shift relative to the arc frame solution, the pipeline cross-correlates science frames against a high-resolution night sky spectrum. Then, the pipeline fits the B-spline model encompassing the sky intensity as a function of wavelength to the sky regions of the slitlet (Newman et al. 2013). From this process, the pipeline outputs the `spSlit` file per slitlet per chip containing the reduced two-dimensional spectra derived from each science frame and bspline fit information.

3.1.3 Combining Images

For each observation, a series of science images were taken. In this step, we combined each science image into one inverse-variance-weighted mean, sky-subtracted, cosmic ray-cleaned image using the `SP-SLIT_COMBINE` procedure. To combine data, the pipeline subtracts the B-spline sky model from the science image flux. Then, all sky-subtracted images are combined by adding the flux values together, weighted by the values of inverse variance maps from the preceding stages. As a result, the pipeline outputs a single slit file for each slitlet for each chip containing the two-dimensional spectrum (spec2d). Then, 1D spectra are extracted from 2D spectra using both "optimal" and "boxcar" extraction techniques.

3.2 Measurements of Spectroscopic Redshift

We measure spectroscopic redshift using the IDL-based software called SpecPro, developed by Masters & Capak (2011). This software provides a user-friendly method to measure the redshift from both reduced 1D and 2D spectra. The spectroscopic feature templates provided in this software enable us to match the templates with our dataset for several galaxy types. Furthermore, this software also reads the sky subtraction data contained in the dataset to determine the positions of sky lines before data reduction. This feature helps us distinguish real spectral features from residual

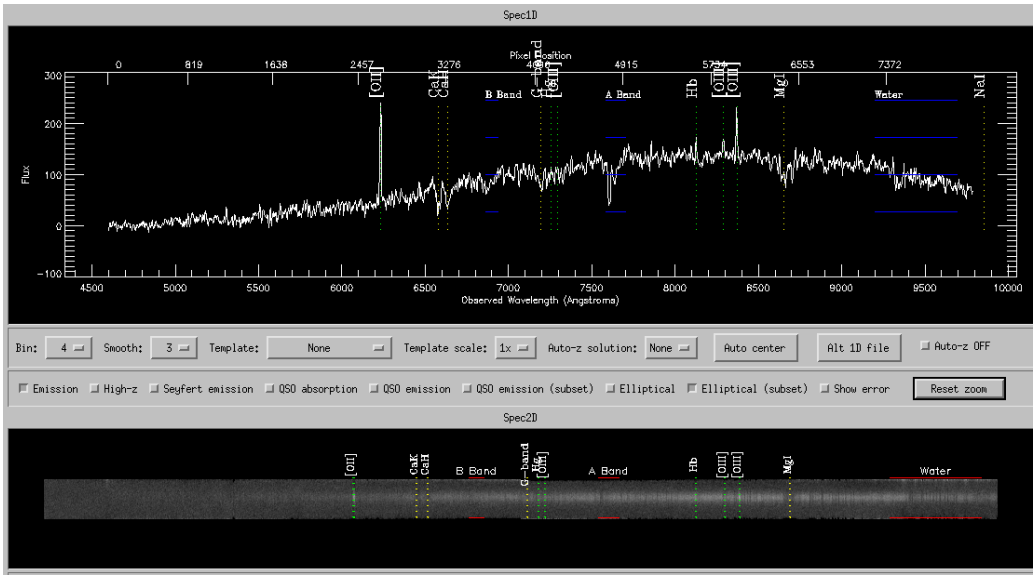

Figure 19: 1D spectrum and 2D spectrum of a star-forming galaxy in the display of SpecPro software. This figure shows the ability of SpecPro to match emission line features such as the [OII] doublet, Hβ, and the [OIII] doublet from star-forming galaxies.

sky lines and artifacts. The example of the SpecPro user interface is shown in Figure 19 and 20.

Since there are many faint galaxies in our dataset, most galaxies do not have spectral features that are easy to identify. To keep track of the quality of spectra, we assign quality flags (Q_f) which are the integers 4, 3, 2, 1, and 0 to indicate the quality of spectra based on the zCOSMOS 10k-bright spectroscopic sample (Lilly et al. 2009). A quality flag of 4 means there is more than one clear spectroscopic feature. The quality flag of 3 means there is more than 1 spectroscopic feature but not as clear as the quality flag of 4. The quality flag of 2 represents a likely redshift, but we are unsure about its reliability. The quality flag of 1 indicates an insecure value of redshift. The quality flag of 0 means we are unable to identify any spectroscopic feature to measure specz.

Apart from quality flags 4, 3, 2, 1, and 0, we also use special quality flags to note certain objects. For example, we designate the object with only one ambiguous emission line that can be either [OII] 3727 or Hα 6563 with the quality flag of 9. Table 3 summarizes the definitions of quality flags used in this study.

Since the spectroscopic redshifts are measured manually in SpecPro software, it carries a potential for human error. To mitigate such uncertainties, we implement a cross-check protocol between two researchers for every slitmask. In this process, two researchers independently measure specz

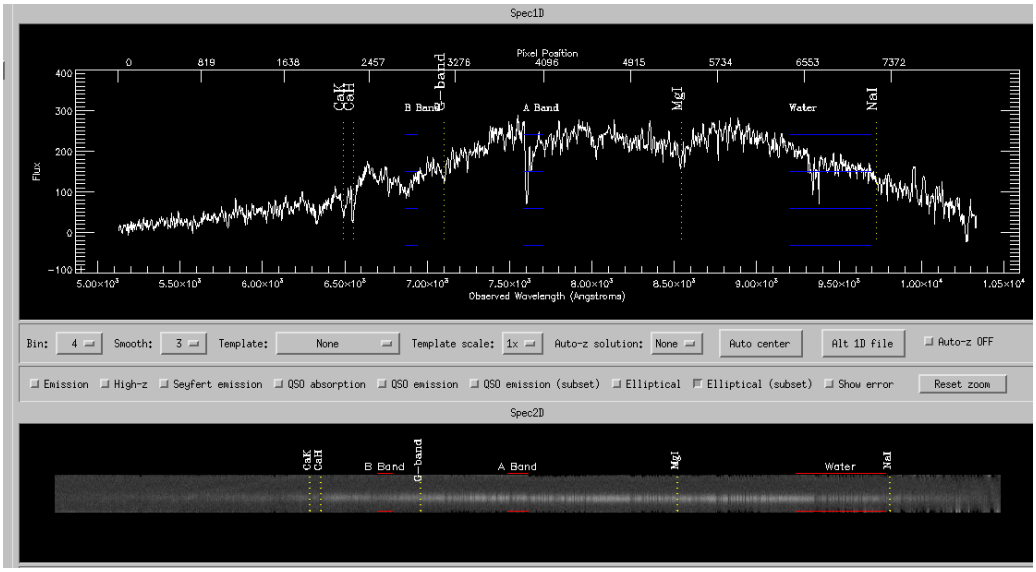

Figure 20: 1D spectrum and 2D spectrum of a quiescent galaxy in the CANDELS fields. This figure shows that SpecPro can also detect absorption features of quiescent galaxies, enabling us to measure spectroscopic redshifts using both emission features and absorption features.

Table 3: Definitions of quality flags Q_f used in the CHESS spectroscopic catalog based on zCOSMOS 10k-bright spectroscopic sample (Lilly et al. 2009).

Quality Flags Q_f	Definition
4	Secure redshift based on multiple spectroscopic features
3	Secure redshift
2	Need additional inspection
1	Insecure redshift
9	Secure single emission line feature that can be either [OII] 3727 or Hα 6563
0	Unable to measure specz

and Q_f for the designated dataset. Upon completion of individual measurements, the dataset from two researchers are compared to identify any discrepancies and then any mismatches between the measurements are then reconciled. At the end of this process, both researchers work toward reaching a consensus on the finalized redshift measurements of the designated slitmask. This cross-checks procedure enhances the reliability of manually measured specz using the expertise of two researchers.

After measurements of specz in 21 masks in the CANDELS COSMOS, UDS, and EGS fields, we obtained a total specz of 3717 sources. We obtained only 677 high-quality ($Q_f = 3$ and $Q_f = 4$) spectra. We can detect star-forming galaxies, quiescent galaxies, foreground stars, high-z sources, and serendipitous sources. By matching coordinates with photometric data, we are able to match these CHESS spectroscopic objects with our existing photometric data described in Section 2.1. Figure 21 shows the comparison between specz and photoz of objects with high-quality spectra from the CHESS observation program. We also show the distribution of specz of high-quality spectra at $0.5 < z < 1.7$ in Figure 22. To determine the accuracy of the specz obtained from the CHESS observing program, we calculate the residual $(z_{photo} - z_{spec})/(1 + z_{spec}) = \Delta z/(1 + z_{spec})$ to visualize how z_{photo} agrees with z_{spec}. Furthermore, we fit a Gaussian distribution to the residual to determine the uncertainty of photoz compared to specz using the CHESS data. From this procedure, we obtain the best fit of the standard deviation $\sigma_{\Delta z/(1+z_{spec})} = 0.015$. This value can be used as the uncertainty of photoz compared to our specz from the CHESS observations.

3.3 Stacking of Spectra

The process of spectra stacking is necessary for combining slitmasks that underwent multiple observations, or objects observed across multiple masks. Some slitmasks such as COS1, COS3, COS5, and COS12, were observed on multiple nights due to poor weather conditions and observational issues. To enhance the quality of spectra from these masks, we used the `SP-SLIT_COMBINE` procedure from the DEEP2 pipeline to combine the entire slitmask taken from different nights. This procedure was applied to COS1, COS3, and COS5 slitmasks to stack the spectra taken from multiple nights. However, in the case of the COS12 mask, we decided to exclude the data obtained on

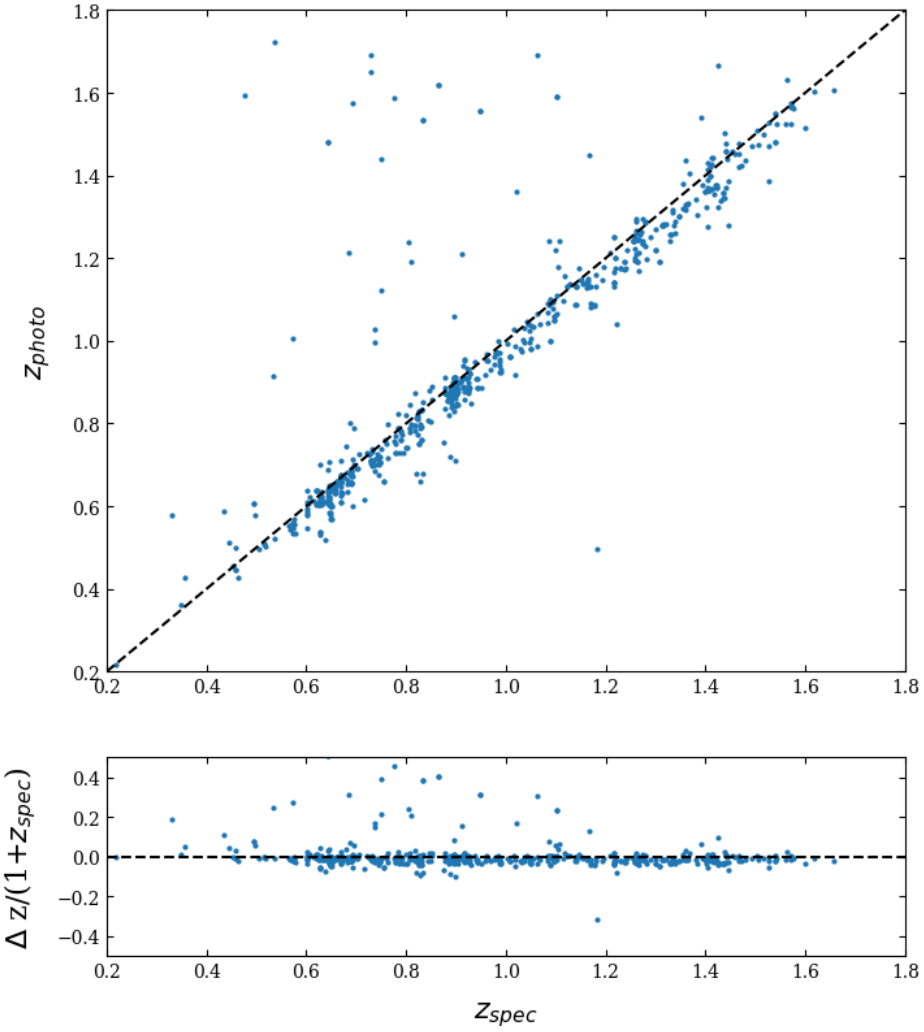

Figure 21: Comparison between photoz z_{photo} and specz z_{spec} from high-quality spectra obtained from the CHESS observing program.

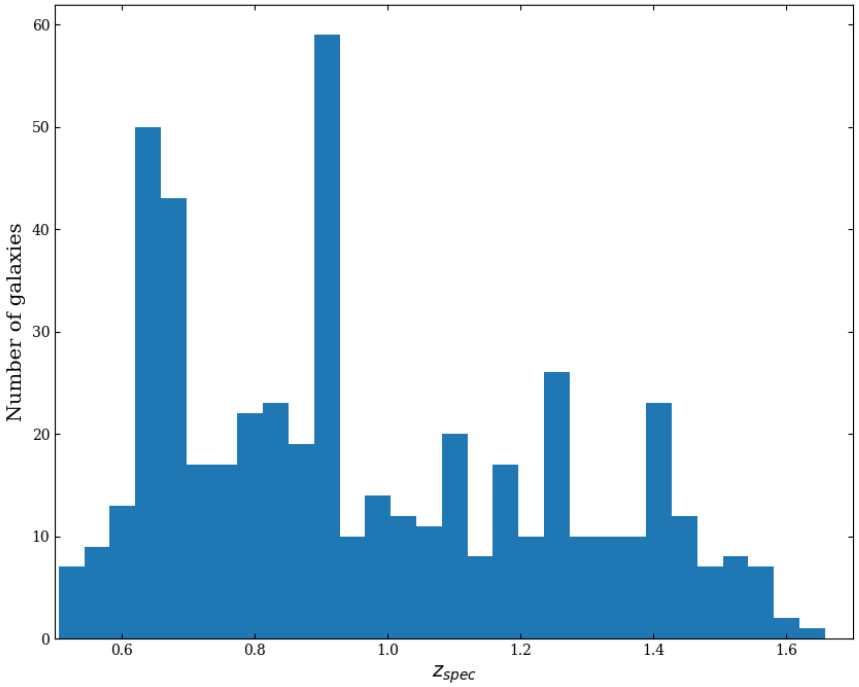

Figure 22: The histogram showing the distribution of specz in our preliminary CHESS catalog at redshift $0.5 < z < 1.7$. This histogram also shows two peaks of specz at redshift $z \sim 0.65$ and $z \sim 0.90$, implying the cluster of galaxies at these redshifts.

November 29th, 2021 due to the effect of poor weather conditions that affected the data quality. As a result, we used only the data from COS12 acquired on the night of January 8th, 2022.

Additionally, many objects were observed numerous times across different masks. These objects are the faint objects that were placed within the overlapping regions between slits for multiple observations as discussed in section 2.2.1. The multiple observations of these objects allow us to increase the signal-to-noise ratio of these objects by coadding multiple 1d spectra of the same object obtained from different slitmasks. To add the flux values among all spectra, we assigned the weight of each flux value based on the exposure time. Given that our standard exposure time for the CHESS observation is at 7200 seconds, we define the weight value as $w = t_{exp}/7200$, ensuring that the weight of an object with an exposure time of 7200 seconds would be equal to 1.

There are a total of 529 faint spectra with multiple observations (278 spectra in COSMOS, 215 spectra in UDS, and 36 spectra in EGS). The stacking process was successfully performed using a Python script to interpolate the wavelength scale and combine 1D spectra. The in-depth examination and analysis of these stacked spectra will be performed as the future work of this thesis.

3.4 Serendipitous Spectra

While pointing the telescope at primary sources, the spectra of nearby objects can inadvertently contaminate the slitlet, resulting in the capture of more than one spectrum on a single slit as shown in Figure 23. We refer to these extra spectra as "serendipitous spectra." We plan to include some of the serendipitous objects in our catalog. Nevertheless, since these objects are typically located at the edge of the slit, it is difficult to pinpoint the precise coordinates of these serendipitous sources. Therefore, it is necessary to conduct a thorough inspection of galaxies in the vicinity of the primary target to identify the nearby sources as shown in Figure 24. This task was performed by the summer REU student Jonathan Diaz. By inspecting both 2d spectra, image cutouts of the area surrounding the primary galaxy, and photoz, we were able to deduce 31 possible sources (18 from COSMOS, 4 from UDS, and 9 from EGS) of serendipitous spectra, and added these sources to our preliminary catalog. The comparison between photoz and specz of our dataset with serendipitous sources is

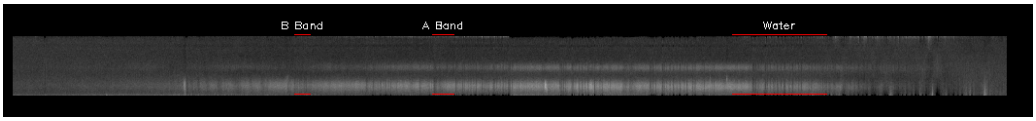

Figure 23: The serendipitous spectrum of a galaxy near the primary target COS_23969. We note the serendipitous spectra at the bottom of the image correspond to a galaxy at redshift $z = 0.6975$.

shown in Figure 25

Adding the 31 serendipitous sources out of 54 total serendipitous sources to our spectroscopic catalog, we now have 677 high-quality spectra in total for the preliminary CHESS spectroscopic catalog.

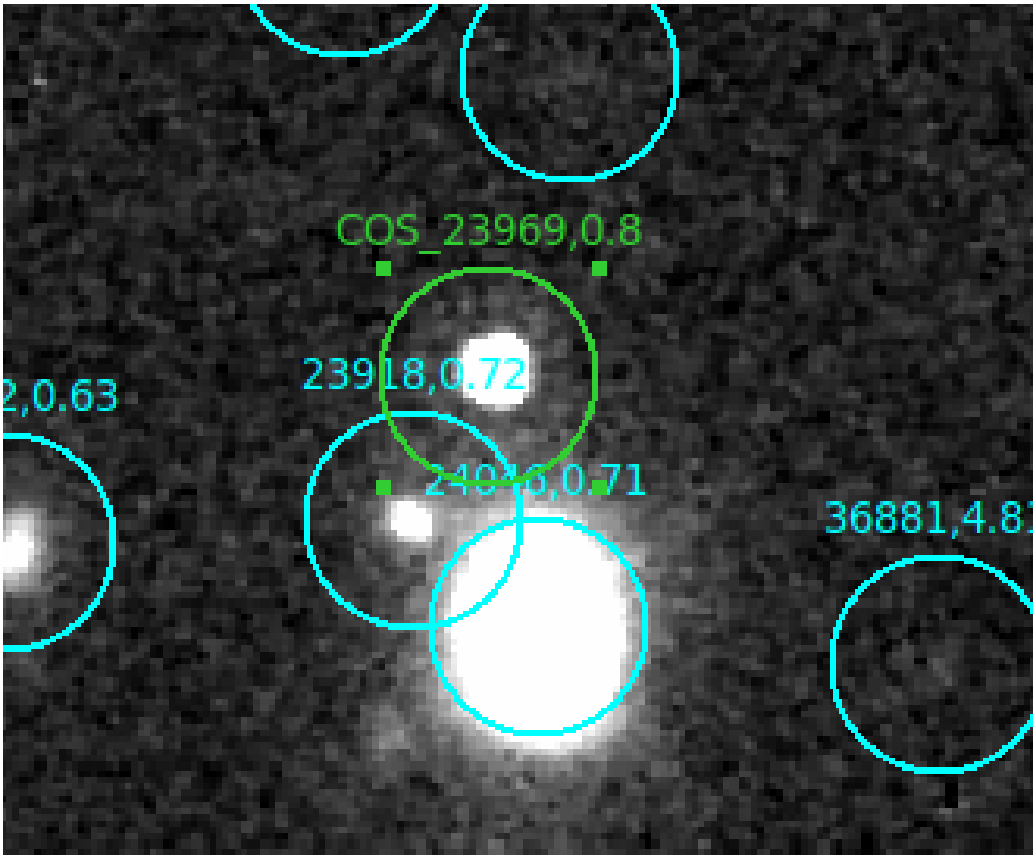

Figure 24: The stamp image associated with the object COS 23969 with spectrum shown in Figure 23. By inspection of both 2d spectrum and stamp image, we concluded that the object that the possible object for this serendipitous spectrum is COS24016

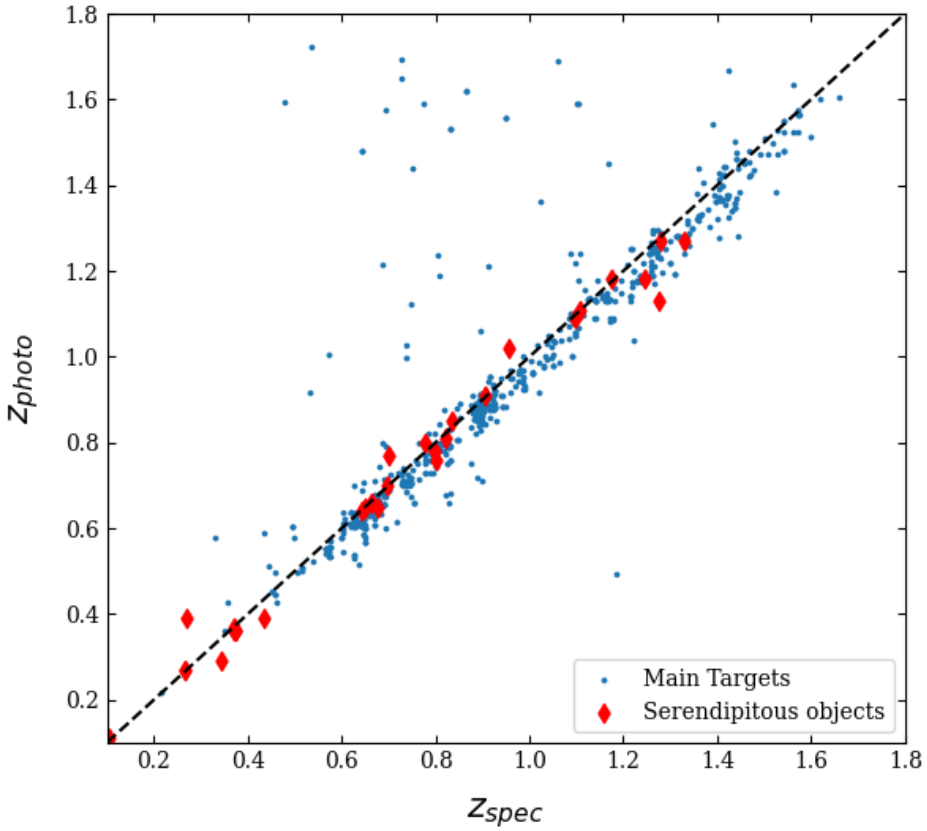

Figure 25: The photoz and specz of serendipitous objects that were added to the CHESS spectroscopic catalog.

4 Creating Density Maps

In this chapter, we describe the process to construct improved environmental density maps and the SFR-density relation following the acquisition of new specz from the CHESS observation program. To create new density maps, we first combine the CHESS specz into the existing archival spectroscopic catalog. Then, we match the photometric archival data with the spectroscopic data to construct the full dataset describing both the spectroscopic and photometric properties of galaxies.

Using the complete dataset, we generate new density maps and overdensity maps of galaxies across all five CANDELS fields using the Voronoi Monte-Carlo technique described in Chapter 1.5. We also study the impact of the CHESS catalog on environmental density mapping by generating density maps both with and without the inclusion of the CHESS specz. By performing this task, we are able to assess how additional data enhances the accuracy of the environmental density mapping process.

Furthermore, the last step of this study is to construct the preliminary SFR-density relation to identify environmental density impacts the SFR of massive galaxies. Through these processes outlined in this chapter, we aim to gain a better understanding of the relationship between the local environment with the properties of galaxies within the CANDELS fields.

4.1 Spectroscopic and Photometric Data Selection

In this study, we improve the existing archival spectroscopic catalog by incorporating the new spectroscopic catalog obtained from the CHESS program. Following this process, we match the spectroscopic data with the CANDELS photometric data. This section outlines the overview of the steps involved in this process including the criteria to select spectroscopic data and the methodology to ensure the precise combination of these selected objects with the photometric dataset.

4.1.1 Combined Spectroscopic Dataset

We incorporate the CHESS specz with spectroscopic catalog obtained from various surveys, such as 3D-HST (Momcheva et al. 2016), PRIMUS (Coil et al. 2011), MOSDEF (Coil et al. 2015),

Table 4: A table showing the comparison between the number of spectroscopic sources contained within the CHESS catalog and the total number of spectroscopic sources within the combined catalog, focusing on the redshift range of $0.5 < z < 1.7$

Field	Total sources	Total CHESS sources	Percentage of the CHESS sources
COSMOS	1,179	77	6.53 %
UDS	863	84	9.73 %
EGS	828	68	8.32 %

zBRIGHT (Lilly et al. 2009), and other catalogs mentioned in Chapter 2.1. At this step of our study, we included the spectroscopic redshifts from the CHESS catalog that have the quality flag Q_f of 3 and 4.

To evaluate the impact of the CHESS catalog on the total number of spectroscopic sources in the CANDELS COSMOS, UDS, and EGS fields within the redshift range of $0.5 < z < 1.7$, we compare the number of sources within the CHESS catalog and the cumulative count of sources in the combined spectroscopic catalogs for our target redshift range. The corresponding result is shown in Table 4.

4.1.2 Photometric Dataset Matching

To have a comprehensive sample with both photometric and spectroscopic information, we combine our combined spectroscopic catalog with existing photometric catalogs in all CANDELS fields including COSMOS (Nayyeri et al. 2017), UDS (Galametz et al. 2013), EGS (Stefanon et al. 2017), GOODS-N (Barro et al. 2019), and GOODS-S (Guo et al. 2013). These photometric catalogs contain photometric data from various bands from UV to mid-infrared including HST/WFC 105W, F125W, and F160W, Spitzer IRAC, and VLT K-band (check all the bands in all 5 catalogs again). Furthermore, these photometric catalogs also contain stellar mass (M^*), photoz distribution, and SFR information acquired through various SED fitting codes. (include more details here) The information about these five photometric catalogs is shown in Table 5.

To correctly match objects in spectroscopic and photometric catalogs, we define the selection criterion based on the sky coordinates of objects. In this approach, the objects are considered

Table 5: The summary of CANDELS photometric catalogs

Field	Number of sources
COSMOS	38,671
UDS	35,932
EGS	41,457
GOODS-N	35445
GOODS-S	34,930

matched when the positions of objects in both catalogs coincide within a separation of 1 arcsecond. This criterion ensures the accurate pairing of objects across both catalogs. Furthermore, we also apply the mass cut criterion by selecting objects with stellar mass $M^* > 10^{10}$ solar masses. We use this mass cut to exclusively select galaxies that contribute to the overall SFR density, as well as to ensure full spectroscopic completeness at our redshift range. The histogram shown in Figure 26 demonstrates the mass cut of the objects with $M* > 10^{10}$ solar masses. This value of mass cut is roughly complete at all redshift ranges considered.

Since our spectroscopic catalogs contain data collected from various surveys, there are many duplicated objects that were observed in various surveys. We address this problem by generating a list of duplicated objects from the spectroscopic catalog. Then, we select galaxies based on quality flags Q_f, and the hierarchy of spectroscopic surveys. At the start of this procedure, we select objects with higher quality flags, indicating a more reliable specz. If multiple galaxies have high-quality flags, we proceed to the second selection criterion based on the hierarchy of spectroscopic surveys. This criterion prioritizes galaxies observed by instruments that have higher spectroscopic resolution.

This second criterion takes instruments employed in surveys into consideration. Surveys that utilize 8-10 m class telescopes such as Keck and Subaru are given higher priority in galaxy selection. On the other hand, surveys that involve grism and prism such as PRIMUS are ranked lower due to their lower spectral resolution. Using this criterion, we ensure that galaxies with more reliable specz are selected to match with photometric data. The final combined dataset is used for generating density maps in CANDELS fields.

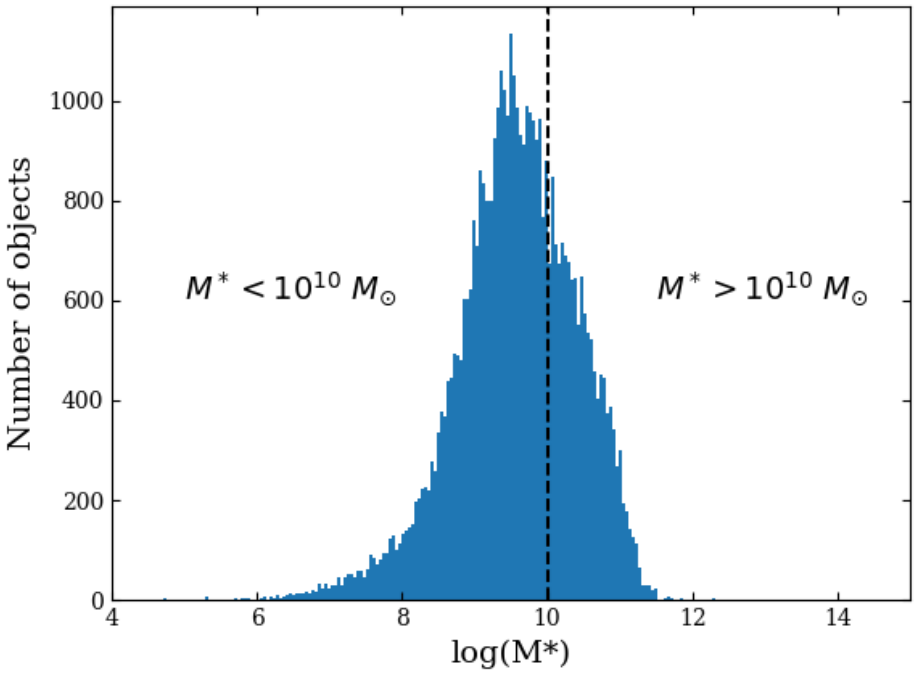

Figure 26: Histogram showing stellar mass distribution of galaxies from all five CANDELS fields. The dash line depicts the criterion of mass selection at $M^* > 10^{10}$ solar masses.

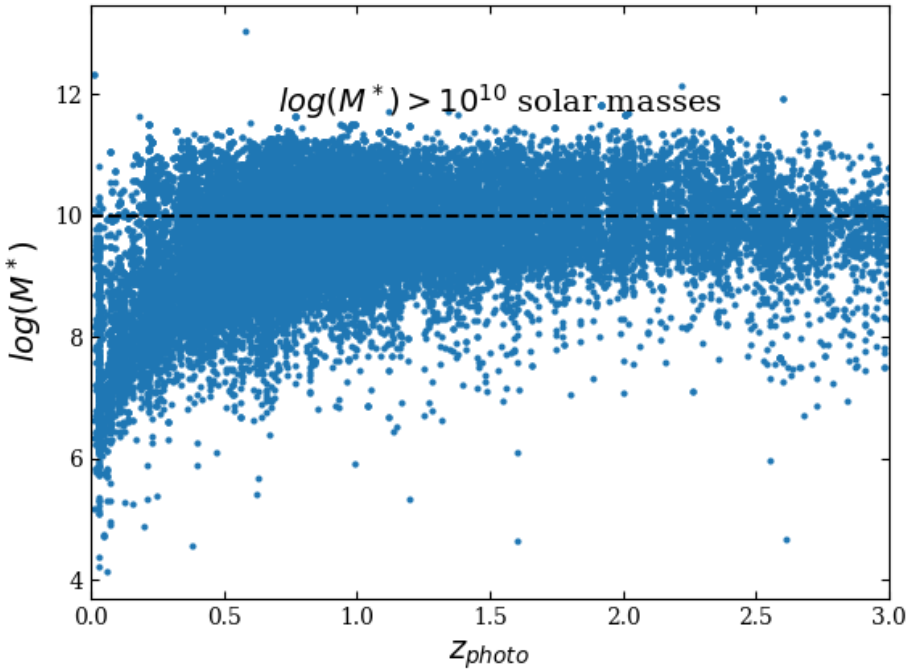

Figure 27: Stellar mass as a function of redshift using combined photometric data in all five CANDELS fields. This plot shows that galaxies at mass $M^* > 10^{10}$ solar masses can provide an unbiased spectroscopic sampling for our study.

4.2 Generating Density Maps

We generate surface density maps using the weighted Voronoi tessellation method outlined in Chapter 1.5.3 due to its non-parametric and scale-independent nature. In this study, we follow the procedure of the Voronoi Monte Carlo (VMC) technique described in Lemaux et al. (2018); Hung et al. (2019). There are many procedures involved in this procedure, including sample selections, defining redshift slices, Voronoi tessellation, and finalizing density/overdensity maps.

4.2.1 Sample Selection

Since not all galaxies in our samples have reliable spectroscopic redshift, it is necessary to take redshift uncertainties into account. For galaxies with reliable specz ($Q_F = 3, 4$), we consider these specz as the true redshift of galaxies. However, for galaxies with unreliable specz ($Q_F = 2, 1$) or galaxies with no spectroscopic data, we assign the redshift values of these galaxies based on their photoz distribution using the Monte Carlo technique described in Hung et al. (2019).

In this Monte Carlo procedure, we assume that the photoz probability density function (PDF) is a Gaussian distribution centered at the original photoz. The variance σ of this distribution is assumed to be the square of the photoz uncertainties. In each realization, we randomly pick the value of photoz from this PDF to be the redshift values that we use for the Voronoi tessellation process. By having fixed specz and randomized photoz in each Monte Carlo realization, this procedure employs the uncertainty of photoz into account as well as emphasizes the importance of specz in surface density estimation. After selecting values of photoz and specz for our Monte Carlo sample, we put our samples into different redshift slices (z-slices).

4.2.2 Defining Redshift Slices

To ensure the density map coverage up to a redshift of $z = 3.0$, we partition this redshift range into many z-slices from $z = 0.3$ to $z = 2.9$ in each Monte Carlo realization. This redshift range also covers the primary redshift coverage of the CHESS program $0.5 < z < 1.7$, allowing us to evaluate the impact of the CHESS spectroscopic catalog on the improvement of density maps. To create a z-slice, we define the width of each z-slice based on the uncertainty of photoz and the scale of

the structure that we aim to map. In this preliminary study, we adopt a constant z-slice width of $\Delta z = 0.1$. Moreover, we also set a half-bin overlap between each z-slice to ensure continuity between each slice, as well as to include galaxies at the boundary of the z-slice. By using the z-slice width of $\Delta z = 0.1$ with a half-bin overlap, we use a total number of 51 redshift slices to represent density maps from the redshift range of $0.3 < z < 2.9$.

To set up the density resolution of each z-slice, we create a grid of 75×75 kpc proper kpc pixels as the sample of local density distribution Lemaux et al. (2018). This grid represents the pixel size of each density map that we use to study the underlying structures inside all CANDELS fields. After defining the z-slice, we then proceed to perform the Voronoi tessellation procedure to calculate surface density.

4.2.3 Voronoi Tessellation

As defined in Chapter 1.5.3, this density estimation process relies on the partitioning of the area around objects into polygonal cells called Voronoi cells (Vavilova et al. 2021). The Voronoi cell of an object is the region that is closer to that particular object than other objects in the 2D plane. We can use the inverse area of Voronoi cells to represent surface densities Σ since dense regions exhibit smaller Voronoi cells as shown in Figure 28.

In this study, we repeat this Voronoi tessellation process for 100 realizations to account for uncertainties in photoz. Then, we obtain the finalized local overdensity maps in 75×75 proper kpc grids by using the median value of surface density Σ from 100 Monte Carlo realizations to be local pixel density. Finally, the local density $(1 + \delta)$ of pixel (i,j) of the 75×75 proper kpc grid can be calculated using the equation below (Hung et al. 2019).

$$log(1 + \delta) = log(1 + \frac{(\Sigma_{i,j} - \Sigma_{median})}{\Sigma_{median}}) \tag{15}$$

where $\Sigma_{i,j}$ is the pixel's surface density and Σ_{median} is the median density of all pixels in that z-slice.

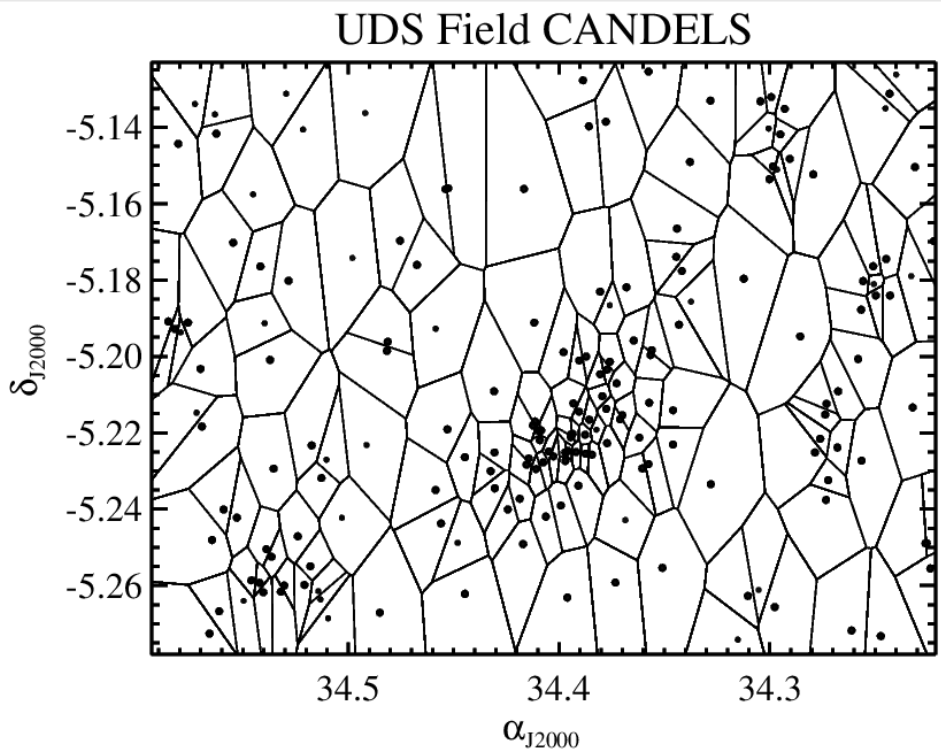

Figure 28: The Voronoi tessellation map of the UDS field at redshift slice $0.6 < z < 0.7$ from one of the Monte Carlo realizations. This plot also shows that Voronoi cells are smaller in dense regions.

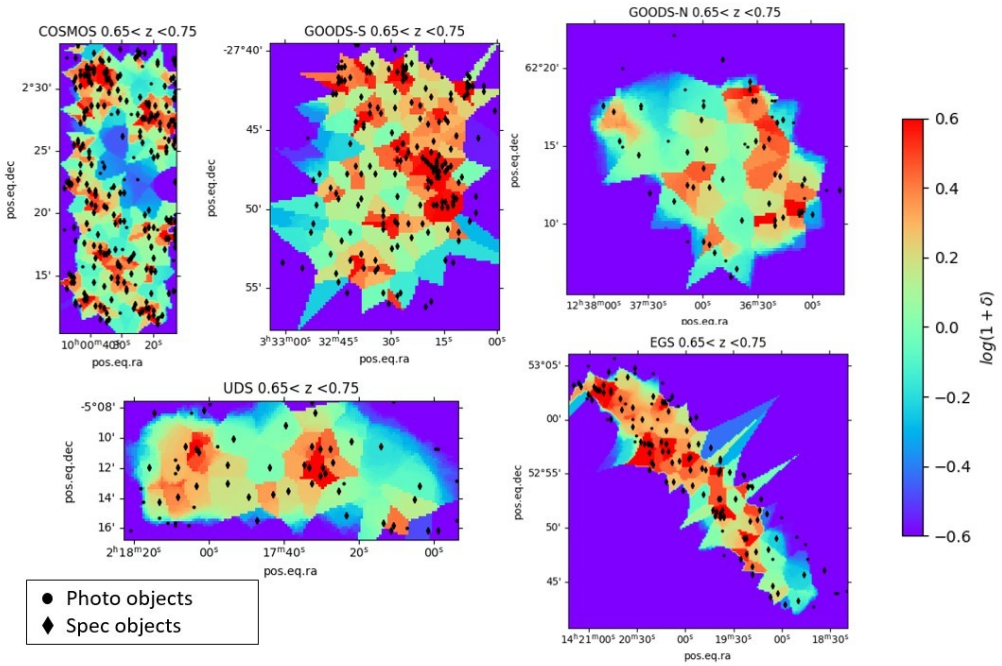

Figure 29: Overdensity maps of CANDELS fields at redshift $0.65 < z < 0.75$ created by 100 realizations of Monte Carlo Voronoi tessellation. Coordinates of objects from our combined photometric and spectroscopic catalogs are also overlayed on top of overdensity maps. These maps show that the overdense regions are the regions where many galaxies cluster together.

4.3 Overdensity Maps

After performing the procedure mentioned in the previous section across all five CANDELS fields, we successfully generate local overdensity fields in the redshift range of $0.3 < z < 2.9$. Furthermore, we also overlay the coordinates of objects derived from the combined photometric and spectroscopic catalogs onto the maps as depicted in Figure 29. This figure demonstrates that the regions with high concentrations of galaxies have higher values of overdensity.

Subsequently, we match the coordinates of overlayed galaxies with the values of local overdensity. This task is crucial in generating the SFR-density relation, which will be discussed in the next chapter.

5 Discussion, Conclusions, and Future Work

In this study, we create a preliminary version of the CHESS spectroscopic catalog. Then, we combine the CHESS spectroscopic catalog with existing archival spectroscopic catalogs and photometric catalogs to generate local overdensity maps at the redshift range $0.3 < z < 2.9$. This chapter summarizes the results and physical interpretations of our research.

5.1 The CHESS Spectroscopic Catalog

Our preliminary CHESS spectroscopic catalog contains specz of 949 identifiable objects. In these identifiable spectra, there are a total of 677 reliable spectra. Figure 30 shows the distribution of the specz, M^*, and 3.6 μm Spitzer IRAC magnitude of the CHESS sample. This sample was created after matching the CHESS spectroscopic catalog with archival photometric data.

Upon a thorough inspection of the specz distribution, we notice that the distribution peaks at $z \sim 0.65$ and $z \sim 0.90$. These peaks suggest a concentration of galaxies at these specific redshifts, indicating the possible presence of galaxy clusters. To confirm the presence of these clusters, a more in-depth investigation will be required in our future work on this study.

Furthermore, the bimodal shapes of stellar mass distribution and IRAC magnitude reflect the target selection employed in the CHESS observing program. As mentioned in Chapter 2.2.2., we prioritize sources with stellar mass $M^* > 10^{10}$ solar masses. Nevertheless, the filler sources, including Herschel-selected sources, high-z sources, galaxy pair candidates, and lower-mass photoz selected sources, contribute to an additional mass distribution peak at $M^* \sim 10^9$ solar masses. The impact of these filler sources is also apparent in the second peak observed in the IRAC magnitude at $IRAC \sim 23$. The overall summary of the CHESS spectroscopic catalog is provided in Appendix A.

5.2 Spectroscopic Completeness Improvement

In section 2.2, we show that the spectroscopic completeness of galaxies with $M^* > 10^{10}$ solar masses in CANDELS COSMOS, UDS, and EGS is small compared to the spectroscopic completeness in

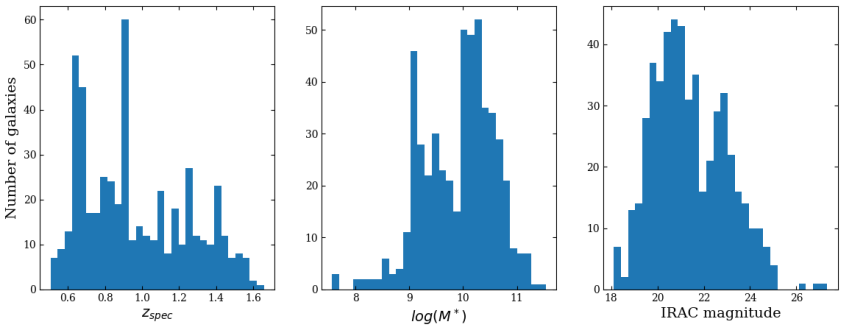

Figure 30: The overview of the CHESS spectroscopic catalog. This figure shows the distribution of specz, stellar masses, and 3.6 μm Spitzer IRAC magnitude of galaxies within the redshift range of $0.5 < z < 1.7$.

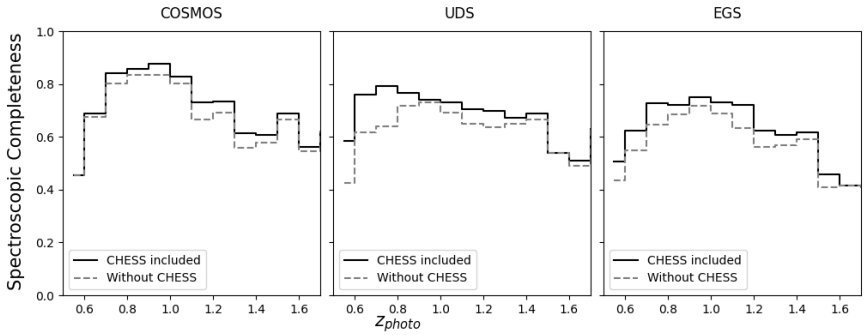

Figure 31: The comparison between spectroscopic completeness in CANDELS COSMOS, UDS, and EGS fields before and after adding specz from the CHESS observing program. This plot shows that the CHESS spectroscopic catalog improves the spectroscopic completeness in CANDELS COSMOS, UDS, and EGS fields.

GOODS-N, and GOODS-S as shown in Figure 9. Hence, we propose the CHESS observing program. After including high-quality spectra from the CHESS program in the existing archival spectroscopic catalog, we recreate the spectroscopic completeness plots for CANDELS COSMOS, UDS, and EGS at the redshift range of $0.5 < z < 1.7$ to evaluate the enhancement of spectroscopic completeness. We find that the CHESS spectroscopic catalog improves the spectroscopic completeness at the redshift range of $0.5 < z < 1.7$ as shown in Figure 31.

The overall completeness in CANDELS fields for galaxies with $M^* > 10^{10}$ solar masses are now shown in Figure 32

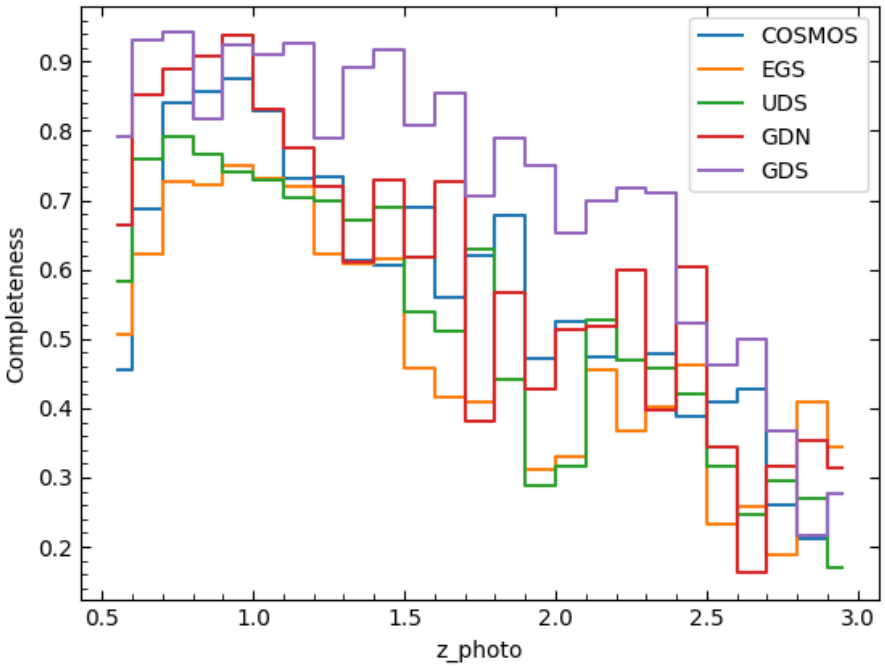

Figure 32: Spectroscopic completeness of all 5 CANDELS fields with CHESS data. By combining the CHESS specz into our existing spectroscopic archival data, we are able to raise the spectroscopic completeness of the CANDELS COSMOS, UDS, and EGS fields closer to GOODS-N and GOODS-S fields.

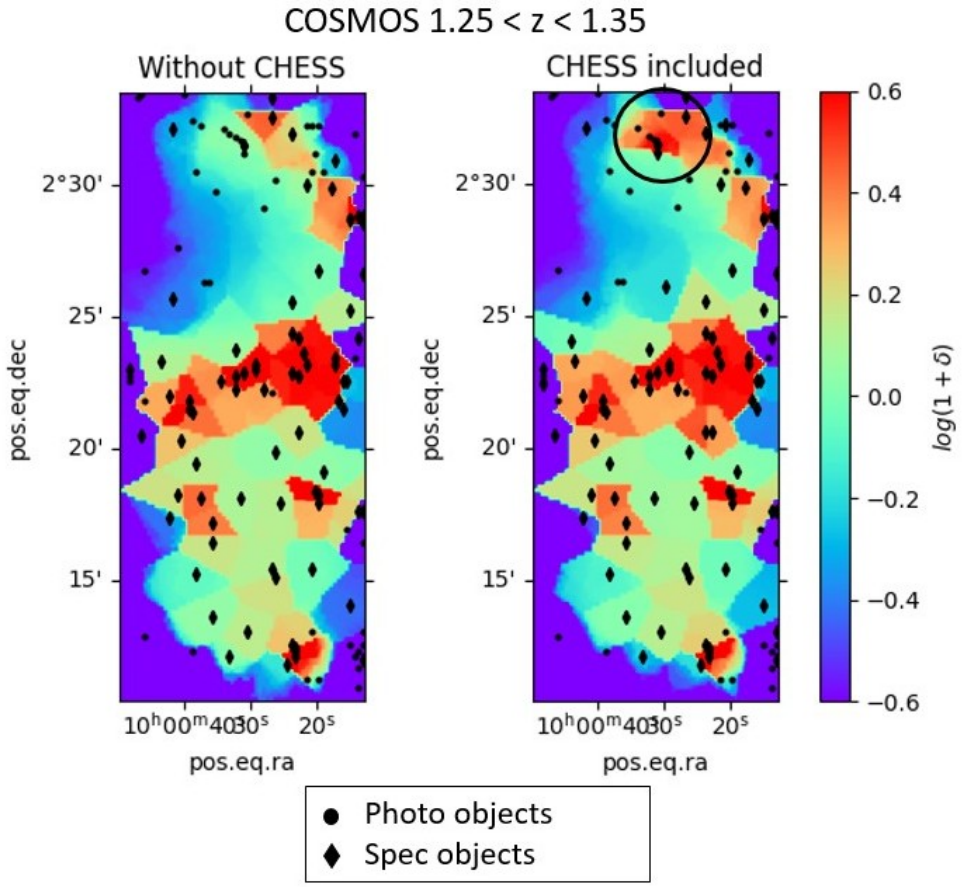

Figure 33: Comparison between overdensity maps before and after adding the CHESS spectroscopic data in COSMOS field

5.3 The Improved Overdensity Maps

We also evaluate how the CHESS spectroscopic catalog improves the measurements of overdensity by comparing the local overdensity maps before and after including data from the CHESS program. Comparing the results from the VMC process between the archival spectroscopic catalog without CHESS data and the results from the VMC process after adding the CHESS data, we are able to detect many new overdensity regions at the redshift range $0.5 < z < 1.7$ as shown in Figure 33, 35, and 34.

These density maps show the CHESS catalog added specz to sources without photometric redshift. Since the number of sources with specz increased due to the CHESS catalog, the overdensity

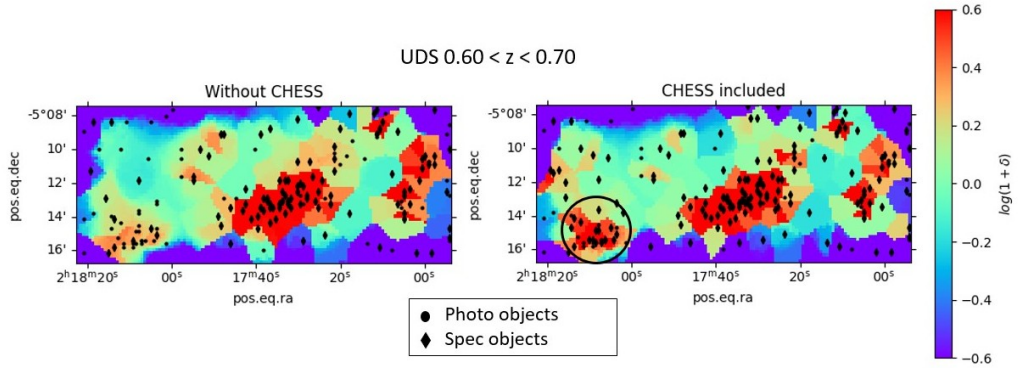

Figure 34: Comparison between overdensity maps before and after adding the CHESS spectroscopic data in UDS field

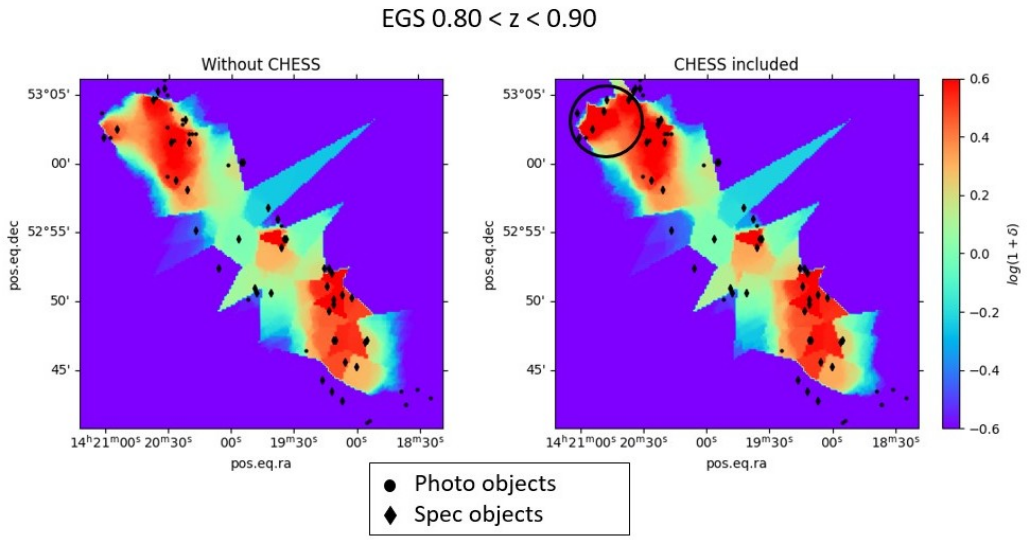

Figure 35: Comparison between overdensity maps before and after adding the CHESS spectroscopic data in EGS field

regions become more stand out.

5.4 The Relation Between SFR and Local Density

Upon completing our new local overdensity maps, we are able to create a preliminary version of the SFR-density relation. At this step of our study, we have not performed SED fitting of photometric data to determine the SFR of our galaxy sample yet. Nevertheless, we can still rely on the existing SFR from the existing photometric catalog mentioned in section 4.1. In our study, we use the SFR excerpt from the SED fitting method 2_*tau* described in Nayyeri et al. (2017). Using this SFR data, we are able to match the SFR with the density data we calculated in the preceding steps.

To study how SFR-density relation evolves with redshift, we plot SFR-density relation across different redshift ranges including $z < 1.0$, $1.0 < z < 1.5$, $1.5 < z < 2.0$, and $z > 2.0$. Since we prioritize star-forming galaxies that contribute to the overall SFR of the universe, we select galaxies that have SFR greater than $log(SFR) > 10^{-4}\ M_{\odot}/yr$. Besides, since we focus on the overall relation between the SFR of galaxies and environmental overdensity, we bin the overdensity $log(1+\delta)$ into seven different bins. The SFR we use in each bin is obtained from the mean SFR within the bin. The uncertainty is then calculated from the standard error of the mean of SFR within the bin. Figure 36 shows the SFR-density relation at different redshift ranges.

In this preliminary SFR-density relation shown in Figure 36, we notice that the SFR of galaxies at high redshift is typically higher than the SFR of galaxies at lower redshift. The SFR-density relation appears flat at the redshift range $z < 1.0$ and $1.0 < z < 1.5$. However, we observe the reversal of the SFR-density relation at redshift range $1.5 < z < 2.0$, and $z > 2.0$. Nevertheless, since this SFR-density relation is still in a preliminary state, we only used the archival SFR data which is still incomplete. Hence, the relationship between SFR and environmental density still requires further investigation.

5.5 Future Work

As of now, the CHESS spectroscopic catalog is still in its preliminary stage. Before we proceed with the public release of this spectroscopic catalog, many tasks must be completed to ensure its

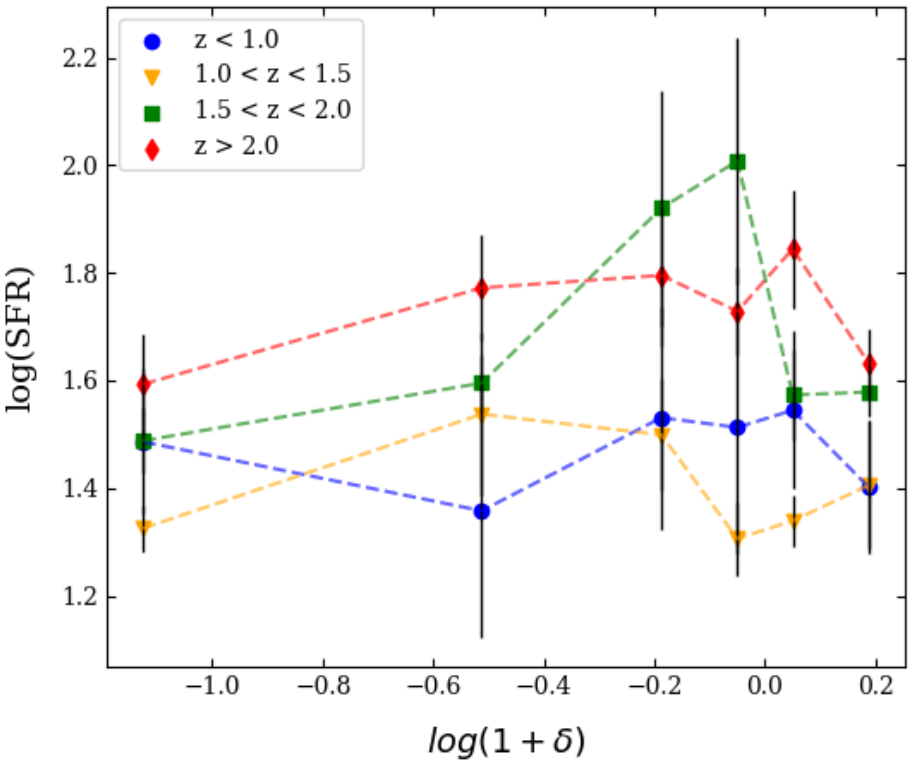

Figure 36: Preliminary SFR-density relation across different redshift ranges. At the redshift bins of $z < 1.0$ and $1.0 < z < 1.5$, the SFR-density relation appears flat at low overdensity. However, the SFR-density relation exhibits the reversal of the SFR-density relation at the redshift bins of $1.5 < z < 2.0$ and $z > 2.0$.

quality. The future critical tasks for the CHESS catalog are shown in the list below:

1. **Extraction of additional specz from faint objects:** As explained in Chapter 3.3, numerous faint objects were deliberately placed within the overlapping regions between slitmasks for repeated observations. In this preliminary study, the task of additional redshift measurements from stacked spectra has not been completed yet, as this task will be carried out in our future work.

2. **Investigation of objects with unusual spectral features:** Another important future task of this research involves an examination of objects with unusual spectral features. For example, some objects such as P_14187 in UDS1 slitmask exhibit a doublet feature that resembles the MgII doublet without other prominent features such as the [OII] doublet. Appendix B showcases some of these anomalous spectra that need more careful inspection before we add them to our catalog.

3. **Examination of serendipitous objects with unclear positions:** At the current step of this study, there remain some serendipitous spectra that are difficult to identify their precise sources. To acquire additional specz from these objects, an ongoing effort of serendipitous spectra and stamp image inspection are required.

Upon the completion of the CHESS spectroscopic catalog, we plan to shift our focus to an in-depth study of the impact of local environmental density on the physical properties of galaxies including SFR and AGN fraction. By exploring these properties, we hope to gain new insights into the process of environmental quenching using our improved density measurements. The following list indicates the upcoming phases of our research.

1. **Further improvement of the local overdensity maps:** The future task of this study involves the enhancement of our local overdensity maps. In our preliminary study, we fix the z-slice width to be at a constant value of $\Delta z = 0.1$. To refine the overdensity maps, we plan to adjust the width of our z-slice based on the scale of the structure we want to study. Furthermore, we also aim to incorporate the measurement reliability of specz into

account by devising a system to select and reject specz based on Q_f during the Monte Carlo process (Lemaux et al. 2018). This procedure will increase the reliability of our density maps significantly.

2. **The contribution of lower mass galaxies on the SFR-density relation** In this research, we prioritize the analysis of the galaxies with stellar mass $M^* > 10^{10}$ solar masses to ensure an unbiased spectroscopic sampling. However, we still need to investigate how galaxies with $M^* < 10^{10}$ solar masses contribute to the local overdensity and SFR distribution of galaxies. Therefore, we aim to extend our analysis to galaxies with lower masses in our future work.

3. **SFR measurements in CANDELS fields:** Accurate SFR measurements are critical for environmental quenching studies. While this preliminary study utilizes SFR values derived from archival photometric catalogs, these datasets lack comprehensive SFR measurements. The next step of our studies involves measuring the SFR of galaxies within overdensity maps using the deep Herschel data (Elbaz et al. 2011). We plan to use the SED fitting codes such as CIGALE (Boquien et al. 2019) and MAGPHYS (da Cunha et al. 2008) to obtain the SFR from the Herschel data. By performing this task, we aim to acquire more reliable SFR measurements to generate accurate SFR-density relations.

4. **Measurements of AGN fraction:** It is well-established that the central black hole's growth is closely linked to the evolution of its host galaxy. The study of black hole accretion shows that the black hole accretion history couples with the cosmic star formation history (Madau & Dickinson 2014). Moreover, the relationship between supermassive black hole mass and velocity dispersion σ of a galaxy, known as the $M - \sigma$ relation, and between black hole mass and bulge mass of a galaxy also imply an intricate relation between the central black hole's evolution and that of the entire galaxy (Ferrarese & Merritt 2000; Schutte et al. 2019). Furthermore, several studies also show that AGN hosts are more likely to reside in the dense environment (Hatch et al. 2009; Venemans et al. 2006). Hence, to have a full picture of environmental quenching, it is important to investigate the impact of local overdensity on both the SFR and the accretion of the central supermassive black holes in galaxies.

In our future work, we aim to take the effect of AGN into account when we determine the SFR of our galaxy sample. We will identify AGN using multiwavelength data including X-ray (Chandra & XMM-Newton), Infrared (IRAC & WISE), optical/near-infrared (Ground-based observatories), and radio (E-VLA). We also plan to combine the AGN template with Herschel and Spitzer observations to place a constraint on the AGN contribution to galaxy spectral energy distribution (Delvecchio et al. 2015; Mullaney et al. 2011).

With these tasks, we hope to acquire an in-depth understanding of the interplay between the physical properties of galaxies with the environment they reside in.

5.6 Conclusions

Uncovering the intricate relationship between overdensity and SFR can be difficult due to the complexity of precisely identifying overdensity regions. In this study, we address this problem by introducing the CHESS spectroscopic catalog to increase the spectroscopic completeness and improve environmental density estimation in CANDELS COSMOS, UDS, and EGS fields.

Our data acquisition was performed using the DEIMOS instrument on the Keck II telescope. The survey spans over the area of 600 arcmin^2 using 21 slitmasks (11 slitmasks in COSMOS, 7 slitmasks in UDS, and 3 slitmasks in EGS). These observations were conducted throughout 7 nights of observation from December 2020 to February 2022. This survey focuses on gathering spectra from star-forming and massive quiescent galaxies at the redshift range $0.5 < z < 1.7$ since these galaxies are bright galaxies that we can observe them with full completeness up to $z \sim 3.0$, providing comprehensive data collection.

Over 3700 spectra were collected from the CHESS program. These spectra were inspected and analyzed by many volunteers in our research group to obtain specz. Ultimately, we obtain a total number of 677 high-quality spectra primarily at the redshift range $0.5 < z < 1.7$. With this preliminary catalog, we are able to increase spectroscopic completeness for massive galaxies at our redshift range as shown in Figure 31.

Following the completion of the CHESS catalog, we create local overdensity maps based on the

VMC technique mentioned in Hung et al. (2019); Lemaux et al. (2018) at redshift range $0.3 < z < 2.9$. This redshift range also encapsulates the redshift range of the CHESS survey, allowing us to assess the ability of the CHESS survey in the improvement of the overdensity mapping. By combining the CHESS specz into the existing archival spectroscopic catalog, we are able to identify several new overdensity regions as shown in Figure 33, 34, and 35. Ultimately, we are able to create the preliminary SFR-density relation using data from all five CANDELS fields.

This research serves as the foundation for further investigation of the physical processes behind environmental quenching. In our future work, we aim to delve deeper into the direct measurement of SFR and AGN fractions to see how these parameters related to the local environmental density measured in this study. In conclusion, through this research, we aspire to acquire a more comprehensive understanding of the interplay between galaxy properties and the environment they reside in using our new spectroscopic catalog.

6 Appendix A: The full CHESS Spectroscopic catalog

This appendix shows the full CHESS spectroscopic catalog including the photometric ID, slitmask, sky coordinates, specz, stellar masses, and IRAC (3.6 μm) magnitude in CANDELS COSMOS, UDS, and EGS fields.

6.1 The CHESS COSMOS Data

ID	Mask	spec RA	spec Dec	photoz	specz	Q_f	log(M*)	IRAC (3.6 μm) mag
50	COS5	150.056284	2.177477	0.98	1.051	3	9.29288	23.7705
250	COS5	150.062853	2.182541	0.86	0.886	3	9.07884	23.5209
543	COS5	150.083031	2.186648	0.788	0.783	4	10.5346	19.7353
836	COS1	150.151731	2.188684	0.92	0.927	3	10.5496	19.5227
910	COS14	150.158207	2.190113	0.92	0.926	3	10.6189	19.6104
969	COS15	150.111603	2.187164	0.7189	0.8894	3	10.7321	20.5693
1051	COS1	150.15901	2.191276	0.9302	0.9237	3	10.428	20.3238
1236	COS1	150.169921	2.195733	0.7377	0.75	4	7.97681	27.3373
1247	COS15	150.14334	2.192638	0.82	0.799	4	11.1319	18.9968
1301	COS2	150.0784	2.194738	0.923	0.991	3	10.5487	19.6772
1673	COS15	150.147021	2.1989	0.655	0.664	4	10.5905	19.7582
1674	COS5	150.06207	2.199368	1.359	1.436	3	10.0181	21.6941
2016	COS1	150.17991	2.203646	1.139	1.1535	3	10.2745	20.856
2913	COS14	150.193125	2.212808	0.66	0.665	3	9.3118	21.8384
2990	COS5	150.057093	2.214588	1.27	1.328	3	8.5332	24.603
2997	COS2	150.056344	2.213945	1.241	1.329	3	10.2937	20.7355
3016	COS14	150.188882	2.214361	0.37	0.372	4	8.37894	23.6542
3139	COS14	150.130875	2.215134	0.88	0.8465	3	10.3376	20.6043
3282	COS15	150.093706	2.216802	0.912	0.925	3	10.0737	20.6841
3320	COS14	150.142317	2.21652	0.63	0.659	4	9.57167	21.1058

ID	Mask	spec RA	spec Dec	photoz	specz	Q_f	log(M*)	IRAC (3.6 μm) mag
3478	COS2	150.111313	2.219354	1.27	1.279	3	9.19075	23.8537
3580	COS14	150.200522	2.218306	0.87	0.88	3	10.6561	19.5943
3835	COS2	150.10685	2.223145	1.088	1.177	3	9.36287	23.1084
4064	COS5	150.06501	2.225362	1.088	1.139	3	9.83629	21.5726
4124	COS5	150.09128	2.225479	1.177	1.24	3	10.5851	20.0713
4151	COS5	150.066616	2.226266	1.13	1.1408	3	10.0401	21.2552
4280	COS1	150.203928	2.225656	0.8752	0.879	3	11.2035	18.9393
4455	COS15	150.102258	2.230143	0.698	0.732	3	9.3126	22.3711
4472	COS14	150.201099	2.228936	0.65	0.66	4	10.2251	19.5631
4556	COS15	150.091122	2.232207	0.652	0.6825	3	9.08349	22.754
4745	COS2	150.084634	2.234949	1.2657	1.2602	3	9.00674	24.2659
4819	COS1	150.204972	2.23503	0.91	0.879	3	10.2072	20.6853
4875	COS15	150.081482	2.236358	0.635	0.683	3	9.58133	21.6671
4883	COS5	150.081782	2.23702	1.93	0.6825	4	9.09225	-99
4893	COS5	150.064988	2.23697	0.29	0.345	4	7.6654	-99
4895	COS1	150.131999	2.236819	1.4784	1.4667	3	9.15442	24.3174
5127	COS5	150.08043	2.238979	0.97	0.9805	3	10.0946	21.0458
5244	COS1	150.195755	2.239657	0.6687	0.678	3	10.0603	21.3798
5812	COS2	150.1136	2.247406	1.193	1.2585	3	9.54214	22.6649
6131	COS5	150.12922	2.251464	0.76	0.7885	3	9.54349	21.8216
6227	COS15	150.11733	2.253364	0.9999	0.9854	3	8.6274	24.6495
6750	COS14	150.175743	2.258832	1.165	1.2175	3	10.8101	19.8085
6935	COS14	150.17582	2.262308	0.898	0.9235	4	9.19516	23.0267
7074	COS5	150.106395	2.26436	1.22	1.099	3	9.12717	23.9984
7191	COS15	150.155282	2.265552	0.77	0.7775	4	8.58182	24.5537
7388	COS5	150.11535	2.267393	0.83	0.825	3	10.2056	20.9623
7434	COS1	150.162555	2.268088	0.91	0.906	4	9.4671	22.3715

ID	Mask	spec RA	spec Dec	photoz	specz	Q_f	log(M*)	IRAC (3.6 μm) mag
7510	COS14	150.133036	2.268477	0.882	0.905	3	10.102	20.773
8148	COS15	150.14659	2.27657	0.996	1.0475	3	9.77308	21.5019
8304	COS15	150.147135	2.27823	1.024	1.048	4	9.63942	21.7516
8401	COS13	150.087695	2.280013	1.372	1.405	3	9.48871	23.3202
8503	COS2	150.054426	2.281715	0.949	0.938	3	9.52567	21.847
8625	COS2	150.113217	2.28315	1.179	1.1953	3	9.0228	24.2756
8725	COS15	150.135358	2.283006	0.66	0.668	4	10.0961	20.9398
8999	COS2	150.08649	2.286195	1.21	1.2605	3	9.99235	21.4119
9043	COS14	150.179965	2.285958	1.26	1.3395	3	10.4287	20.6224
9058	COS15	150.096017	2.287713	1.214	1.2085	3	9.59095	22.561
9087	COS1	150.189516	2.288241	0.85	0.834	4	8.51966	23.97
9156	COS2	150.07908	2.288213	1.69	1.062	3	10.9771	20.4496
9732	COS13	150.10971	2.295693	1.258	1.331	3	10.0064	21.6459
9797	COS11	150.203799	2.296556	0.78	0.798	3	8.65607	23.3685
10013	COS15	150.135623	2.298892	1.5	1.517	3	10.3422	21.3624
10308	COS13	150.088543	2.302533	1.04	1.222	3	9.22232	23.4205
10614	COS15	150.11051	2.305368	1.42	1.4665	3	9.81265	22.3723
10694	COS14	150.155559	2.307134	0.855	0.883	3	8.31819	24.731
10753	COS15	150.10036	2.307628	1.5555	0.949	4	9.61028	23.3407
10999	COS13	150.05572	2.309086	0.69	0.689	4	10.2751	19.8347
11038	COS3	150.1782	2.311199	0.88	0.925	3	8.66006	25.1643
11079	COS14	150.171658	2.311634	1.29	1.3395	3	9.25465	23.4203
11194	COS14	150.161898	2.313051	0.752	0.761	4	9.11594	22.7487
11330	COS15	150.15123	2.314515	1.13	1.216	3	9.62783	22.9982
11449	COS1	150.1515	2.314926	1.081	1.17	3	10.0663	21.1948
11645	COS11	150.1674	2.315815	0.859	0.852	3	10.6517	19.9019
11700	COS11	150.17381	2.318358	1.029	0.736	3	10.1019	20.7083

ID	Mask	spec RA	spec Dec	photoz	specz	Q_f	log(M*)	IRAC (3.6 μm) mag
11869	COS13	150.065939	2.319643	0.71	0.73	3	10.6871	19.8344
11965	COS13	150.122523	2.321752	1.34	1.431	3	9.11391	24.1825
12294	COS11	150.199282	2.323936	0.502	0.517	3	9.19217	23.0291
12797	COS13	150.055328	2.332555	1.595	0.477	4	9.98989	22.4836
12935	COS6E	150.121347	2.334154	0.876	0.899	3	9.53158	22.0932
12951	COS5	150.133347	2.334868	0.8853	0.926	4	8.52523	24.4752
13020	COS11	150.151859	2.334602	1.2136	0.6856	3	11.0088	19.3822
13055	COS4	150.059155	2.336034	0.64	0.658	3	9.12854	22.7703
13210	COS13	150.092157	2.337311	0.63	0.656	4	9.46738	21.5964
13711	COS2	150.091511	2.343784	1.476	1.442	3	9.15198	23.8604
13766	COS14	150.19114	2.34402	2.7451	0.663	4	9.75512	23.5851
13782	COS3	150.124569	2.344414	0.89	0.924	3	9.23862	23.0458
13928	COS15	150.111965	2.346341	0.992	1.0035	3	9.03735	23.6419
13931	COS5	150.176989	2.346513	1.533	0.833	3	9.10378	-99
14110	COS4	150.056124	2.347755	1.19	1.2362	3	10.258	20.8344
14212	COS5	150.13118	2.348859	0.218	0.217	3	9.78654	21.0108
14809	COS15	150.10147	2.356194	2.8184	0.335	4	9.57454	23.6997
14877	COS3	150.194132	2.356512	0.638	0.621	3	10.0625	21.2203
14935	COS1	150.16255	2.356702	0.66	0.661	4	10.7538	19.7404
14984	COS15	150.110038	2.358	1.451	1.458	3	10.0957	21.7385
15041	COS11	150.17053	2.358477	0.68	0.687	4	9.69686	21.7887
15091	COS14	150.195652	2.359959	1.043	1.0845	3	9.08885	23.5152
15138	COS12	150.16178	2.358464	0.951	0.9625	3	10.452	20.2818
15160	COS5	150.10328	2.36075	1.62	0.864	3	10.1614	22.3449
15252	COS15	150.094273	2.36133	0.706	0.747	4	9.10481	22.8823
15339	COS13	150.054144	2.360021	0.91	0.917	3	10.5073	20.2298
16023	COS1	150.13053	2.370629	2.7191	0.217	4	10.2491	22.4763

ID	Mask	spec RA	spec Dec	photoz	specz	Q_f	log(M*)	IRAC (3.6 μm) mag
16027	COS2	150.130928	2.370423	0.64	0.643	4	8.96476	23.0385
16048	COS3	150.204259	2.370626	1.19	1.2632	3	10.1257	21.2885
16068	COS12	150.130867	2.370895	1.48	0.643	3	10.0433	22.0046
16196	COS2	150.0701	2.372566	1.241	1.257	3	10.1237	21.5231
16245	COS11	150.175457	2.371218	0.68	0.688	4	10.3906	19.3457
16675	COS12	150.102756	2.377718	1.24	1.25583	3	10.0653	21.4315
17088	COS11	150.202192	2.382422	1.07	1.084	3	10.2405	21.1447
17184	COS3	150.199538	2.384559	1.133	1.1232	3	9.3783	22.9419
17210	COS11	150.183141	2.385404	1.65	0.7285	3	9.30507	24.6235
17308	COS12	150.152665	2.385281	0.893	0.8992	3	10.1228	21.3658
17496	COS15	150.075652	2.387737	1.29	1.262	3	10.3795	20.8297
17576	COS12	150.15003	2.389616	0.874	0.9024	4	9.2557	22.8407
17625	COS11	150.165456	2.389294	0.898	0.9	4	10.4639	20.5776
17691	COS13	150.06166	2.390687	1.133	1.1705	3	10.0717	21.2598
17825	COS3	150.149906	2.392446	1.44	1.4438	3	10.2695	21.182
17831	COS3	150.15938	2.39106	0.885	0.9	3	11.1126	18.8191
17919	COS13	150.066699	2.393546	0.89	0.894	3	10.207	20.5582
18109	COS5	150.149084	2.396521	0.8985	0.907	3	9.29541	22.2973
18188	COS11	150.1678	2.396654	0.685	0.69	4	10.1741	20.2481
18204	COS5	150.15665	2.395309	0.91	0.899	3	10.6198	20.1541
18323	COS2	150.106245	2.397184	0.61	0.626	3	10.0443	20.9035
18325	COS3	150.185425	2.398347	1.22	1.2995	3	10.5213	20.5724
18435	COS12	150.135932	2.399566	0.87	0.899	3	10.035	21.2429
18581	COS3	150.173327	2.401162	0.36	0.374	4	8.62014	22.6812
18597	COS1	150.186268	2.402313	0.882	0.901	3	9.47215	22.5973
18621	COS11	150.19251	2.401826	0.66	0.661	4	9.14358	22.6072
18659	COS3	150.187552	2.402308	0.9	0.901	3	9.91371	21.7541

ID	Mask	spec RA	spec Dec	photoz	specz	Q_f	log(M*)	IRAC (3.6 μm) mag
18738	COS15	150.150915	2.403696	1.06	0.896	3	10.1615	20.8325
18752	COS15	150.152976	2.394422	0.897	0.898	4	11.5344	18.1263
19059	COS13	150.06073	2.407211	0.916	0.533	4	9.60778	22.4392
19065	COS11	150.197492	2.406222	0.9	0.904	3	10.3869	20.1228
19114	COS11	150.192275	2.407896	1.147	1.1505	3	10.2522	20.8455
19410	COS12	150.15222	2.411407	0.91	0.8976	3	10.333	20.9282
19437	COS3	150.166675	2.412231	1.46	1.441	3	9.52866	23.0374
19636	COS6E	150.156159	2.414913	0.68	0.833	3	9.00033	22.6003
19755	COS3	150.167744	2.416226	0.657	0.69	4	8.55684	24.3647
19771	COS12	150.146281	2.414807	0.888	0.8965	3	10.3218	20.1809
19810	COS15	150.085378	2.416508	0.872	0.888	3	9.42486	22.617
19922	COS15	150.086219	2.418128	1.472	1.5275	3	9.78859	22.3083
19948	COS11	150.183296	2.417748	0.71	0.7298	3	10.067	21.0249
20029	COS4	150.108995	2.418756	0.659	0.756	3	9.47352	22.8613
20066	COS1	150.180918	2.419868	0.7	0.737	3	9.14114	23.1284
20238	COS11	150.181543	2.421366	0.7265	0.725	4	10.4161	20.3112
20294	COS15	150.104212	2.42192	0.71	0.898	4	10.3096	20.1651
20358	COS4	150.121495	2.424295	1.31	1.335	3	9.18255	23.9218
20435	COS1	150.172489	2.423897	0.852	0.833	3	10.7168	19.6159
20530	COS3	150.182132	2.42644	0.27	0.265	4	7.94349	24.3584
20794	COS12	150.117144	2.429673	1.098	1.1138	3	9.42933	22.5516
20859	COS3	150.178497	2.431701	1.14	1.216	3	9.17026	23.7277
21148	COS12	150.10307	2.43459	0.87	0.89	3	9.68672	21.6195
21233	COS3	150.195624	2.434746	0.878	0.902	3	9.58272	21.6941
21295	COS12	150.102433	2.433138	0.9	0.893	3	10.3922	21.1363
21332	COS13	150.07746	2.437006	0.89	0.852	3	9.94639	21.5171
21570	COS12	150.133062	2.440937	1.276	1.405	3	9.20412	23.5026

ID	Mask	spec RA	spec Dec	photoz	specz	Q_f	log(M*)	IRAC (3.6 μm) mag
21641	COS15	150.125764	2.441709	1.138	1.1275	3	9.48181	22.802
21825	COS11	150.16854	2.44334	0.792	0.832	4	9.66191	21.5741
21866	COS6E	150.100157	2.44496	1.3168	1.3348	3	9.02875	23.8787
22057	COS12	150.12584	2.447062	1.514	1.5995	3	10.0112	22.1076
22084	COS3	150.176958	2.447308	1.2	1.2205	3	9.72102	22.6129
22108	COS14	150.167475	2.447132	0.85	0.9	4	9.63184	21.7575
22125	COS11	150.192468	2.44565	0.621	0.606	3	10.3919	19.9897
22208	COS13	150.07932	2.448336	1.39	1.4035	3	9.98733	21.7199
22270	COS11	150.19115	2.449584	0.862	0.888	4	9.60611	21.8795
22278	COS4	150.055816	2.449584	0.74	0.731	3	10.2073	20.7539
22360	COS15	150.137552	2.451479	1.59	1.102	3	10.2083	22.2741
22372	COS6E	150.114797	2.451629	1.28	1.336	3	9.04643	24.1181
22408	COS3	150.182848	2.451103	0.69	0.701	4	10.2507	20.8806
22620	COS13	150.061732	2.454709	1.692	0.729	4	10.6313	20.9292
22745	COS11	150.152023	2.455309	0.834	0.831	3	10.6068	20.1092
22764	COS11	150.18791	2.456752	0.496	0.506	4	8.81823	22.9328
22889	COS3	150.17378	2.458382	1.25	1.217	3	10.6695	20.0315
22897	COS12	150.09965	2.457926	0.73	0.7208	3	10.1359	21.0221
22928	COS12	150.149073	2.460007	1.09	1.17	3	9.07707	23.8324
22955	COS4	150.070842	2.459831	0.704	0.729	4	9.12724	22.8422
23063	COS11	150.16606	2.460919	1.13	1.168	3	10.208	20.9358
23368	COS3	150.13831	2.466236	0.97	0.981	4	10.2395	20.64
23775	COS12	150.099301	2.473452	0.36	0.3707	4	7.70799	25.4082
23798	COS12	150.099212	2.473052	0.558	0.573	3	9.09871	22.7205
23904	COS13	150.055195	2.47263	1.25	1.259	3	11.2898	19.0857
23954	COS6E	150.120021	2.475847	1.257	1.2695	3	9.48874	22.7554
23969	COS12	150.150354	2.475807	0.8	0.687	3	10.0835	21.3811

ID	Mask	spec RA	spec Dec	photoz	specz	Q_f	log(M*)	IRAC (3.6 μm) mag
24005	COS13	150.05534	2.476624	1.2602	1.26	3	9.83036	21.921
24194	COS12	150.147287	2.478214	0.87	0.888	4	10.3981	20.5881
24223	COS3	150.154095	2.479974	0.988	1.0625	3	9.09171	23.5399
24291	COS12	150.160215	2.480156	1.064	1.063	3	10.4745	20.5934
24320	COS6E	150.103972	2.481168	0.704	0.7485	4	9.01715	22.9709
24407	COS4	150.06287	2.480689	0.97	0.9875	3	10.1751	20.5825
24624	COS3	150.195022	2.484585	0.51	0.516	4	9.08342	22.6822
24679	COS3	150.174105	2.486136	0.76	0.832	4	9.02082	23.2478
24733	COS6E	150.113858	2.486678	0.605	0.6035	4	9.61362	21.1169
24818	COS6E	150.113215	2.48836	1.265	1.271	3	9.4574	22.7941
24842	COS4	150.073388	2.487788	1.129	1.163	3	10.0564	21.2163
24902	COS3	150.14307	2.489613	0.86	0.89	3	9.70573	22.1897
24913	COS6E	150.138915	2.490188	0.884	0.89	3	9.87695	21.4798
24922	COS3	150.143108	2.490149	1.18	1.176	3	9.8099	21.7332
24969	COS3	150.170343	2.491266	1.13	1.164	3	9.0819	23.8177
25014	COS4	150.056625	2.491243	0.85	0.89	4	9.47549	21.941
25212	COS12	150.156892	2.496925	0.674	0.672	4	10.6113	19.8056
25297	COS6E	150.164722	2.496587	1.1426	1.1636	3	9.77481	22.3216
25323	COS13	150.123792	2.49638	1.11	1.109	3	8.92627	23.5792
25444	COS4	150.079801	2.498637	0.88	0.9257	3	9.60893	22.3303
25453	COS11	150.205362	2.499287	0.904	0.9109	3	10.7041	20.1013
25469	COS3	150.150932	2.498795	0.743	0.801	4	9.05268	23.0543
25515	COS11	150.181878	2.500811	0.79	0.6945	3	10.7666	19.202
25647	COS4	150.109573	2.501394	1.27	1.301	3	9.09621	23.565
25779	COS12	150.15164	2.503606	1.149	1.165	3	10.1085	21.0567
25929	COS3	150.155134	2.505652	1.324	1.425	3	9.23615	23.3418
26015	COS6E	150.177592	2.508381	0.954	0.988	3	9.39185	23.1134

ID	Mask	spec RA	spec Dec	photoz	specz	Q_f	log(M*)	IRAC (3.6 μm) mag
26042	COS3	150.130524	2.507479	0.64	0.655	4	9.4101	21.8791
26115	COS12	150.097145	2.50879	1.21	0.911	3	10.6138	20.8502
26140	COS11	150.178658	2.50854	1.5888	0.775	4	10.2621	22.0321
26254	COS13	150.05629	2.511313	0.61	0.602	3	10.1036	20.3364
26512	COS3	150.149966	2.514162	1.14	1.163	3	9.80316	21.7468
26527	COS11	150.147852	2.515035	0.843	0.898	4	9.65771	21.5944
26564	COS6E	150.129562	2.514253	0.93	0.989	3	9.01273	23.98
26586	COS4	150.087815	2.514767	0.82	0.8845	3	9.12261	22.4668
26626	COS6E	150.146179	2.515339	0.655	0.6895	4	9.2632	22.4274
26686	COS3	150.13291	2.516831	1.28	1.312	3	10.141	21.3658
26768	COS11	150.194945	2.518263	0.83	0.897	3	10.0698	20.7444
26812	COS11	150.166647	2.525272	0.6	0.693	4	11.2022	18.2997
26823	COS12	150.14303	2.520016	0.909	0.8956	3	10.6262	20.2302
26899	COS4	150.096286	2.520069	0.712	0.737	3	9.14977	22.8366
26940	COS3	150.1312	2.521125	1.238	0.804	4	10.4722	20.7049
27005	COS3	150.13132	2.52379	1.282	1.321	3	11.1738	19.473
27011	COS6E	150.16658	2.524041	0.714	0.692	3	10.5405	20.1432
27036	COS6E	150.1679	2.525725	0.862	0.898	3	9.88356	21.0085
27305	COS12	150.101997	2.527241	0.89	0.887	3	10.5714	20.3169
27385	COS12	150.141758	2.528866	1.27	6.11	3	10.3006	20.7909
27454	COS4	150.08115	2.531788	0.87	0.884	3	10.5574	20.3599
27512	COS4	150.08118	2.530415	0.71	0.73	3	10.6661	19.9952
27693	COS6E	150.110594	2.532286	0.88	0.889	3	9.5667	22.2012
27881	COS4	150.08989	2.535635	1.28	1.3165	3	10.0783	21.6495
27894	COS11	150.185446	2.536098	0.806	0.85	3	10.1531	20.3386
27934	COS3	150.15714	2.536268	0.7	0.695	3	10.0132	21.4049
27983	COS11	150.18993	2.53809	0.701	0.738	4	10.5221	19.2921

ID	Mask	spec RA	spec Dec	photoz	specz	Q_f	log(M*)	IRAC (3.6 μm) mag
28074	COS3	150.180972	2.537803	0.8593	0.8903	3	9.53542	21.7457
28220	COS11	150.174615	2.540575	1.17	1.2665	3	9.93275	21.4482
28279	COS11	150.20363	2.542007	0.88	0.894	3	9.88181	21.1039
28292	COS11	150.168812	2.544538	0.73	0.787	3	10.2906	19.6424
28340	COS3	150.172163	2.542447	0.871	0.9	4	9.38503	22.4296
28396	COS6E	150.170333	2.543392	0.64	0.654	3	9.49504	21.2276
28407	COS12	150.129179	2.546475	1.4737	1.5067	3	10.0714	21.7999
28415	COS11	150.193943	2.551261	0.11	0.1065	4	8.74634	23.8066
28566	COS6E	150.140223	2.543987	0.84	0.891	3	9.23039	22.809
28585	COS11	150.188144	2.546019	1.458	1.4535	3	10.3517	21.363
28649	COS3	150.18581	2.547542	1.4506	1.1675	3	10.0426	21.3383
28655	COS6E	150.18622	2.556436	0.643	0.654	4	10.0661	20.4769
28778	COS6E	150.186617	2.55739	0.7	0.696	3	10.8555	18.4928
35101	COS13	150.059195	2.399244	0.77	0.7	4	8.2215	-99

6.2 The CHESS UDS data

ID	Mask	spec RA	spec DEC	photoz	specz	Qf	log(M*)	IRAC (3.6 μm) mag
527	UDS4	34.468473	-5.275178	0.844	0.905	3	10.49276	20.1063
579	UDS3	34.271284	-5.27479	1.19	0.809	4	10.32634	19.4385
724	UDS3	34.473486	-5.272819	1.724	0.5355	4	9.30963	24.6381
901	UDS4	34.504524	-5.273474	1.666	1.425	3	10.69108	19.7074
1193	UDS3	34.38474	-5.270358	1.039	1.068	3	9.04139	23.1092
1306	UDS4	34.368974	-5.269809	0.908	0.921	3	9.19033	22.4405
1354	UDS3	34.38612	-5.270487	0.772	0.8225	3	10.69984	19.7756

ID	Mask	spec RA	spec DEC	photoz	specz	Qf	log(M*)	IRAC (3.6 μm) mag
1507	UDS3	34.307506	-5.2689	0.727	0.705	4	9.15534	22.5611
1533	UDS3	34.381882	-5.269839	1.405	1.369	4	9.59218	21.5087
1543	UDS4	34.443867	-5.268338	1.51	1.5025	3	9.57749	22.6629
1584	UDS4	34.452809	-5.270059	0.903	0.908	3	10.41497	19.9105
1602	UDS4	34.509048	-5.268224	2.63	0.826	4	10.42325	20.7891
1641	UDS4	34.420108	-5.269048	0.925	0.9872	3	10.10721	20.708
1839	UDS3	34.369229	-5.267944	0.27	0.265	4	9.02119	21.4807
2172	UDS3	34.48498	-5.26711	0.595	0.602	4	10.14922	19.9395
2730	UDS4	34.510902	-5.261475	1.196	1.2821	3	9.53656	21.5768
3002	UDS3	34.310325	-5.262729	0.673	0.693	4	11.04532	18.798
3008	UDS4	34.540276	-5.261784	0.641	0.644	3	10.76268	19.445
3053	UDS4	34.39599	-5.263135	0.578	0.601	4	10.78319	19.196
3227	UDS4	34.531959	-5.261614	0.621	0.647	3	10.8055	19.361
3293	UDS4	34.520752	-5.259838	0.617	0.647	4	10.32222	20.1422
3324	UDS4	34.49234	-5.259536	1.527	1.528	3	10.24055	21.0903
3555	UDS3	34.311769	-5.256895	1.034	1.055	3	9.21219	22.9419
3707	UDS4	34.530373	-5.260015	0.606	0.649	4	11.03342	18.8213
3762	UDS4	34.545963	-5.258646	0.603	0.647	3	10.78247	19.2277
4251	UDS4	34.483612	-5.252642	1.376	1.4225	3	9.87332	22.1183
4276	UDS4	34.486173	-5.25455	0.909	0.9418	3	10.27416	20.2987
4494	UDS4	34.560026	-5.251104	1.037	1.049	3	9.33041	22.5117
4517	UDS4	34.53635	-5.252465	0.637	0.644	4	10.66652	19.6695
4654	UDS4	34.538834	-5.250476	0.632	0.644	3	10.26951	20.5613
4821	UDS3	34.247631	-5.249723	0.668	0.67	3	9.27184	22.5197
4873	UDS4	34.407013	-5.248343	1.414	1.405	3	9.13033	23.7296
5048	UDS4	34.564606	-5.248111	0.688	0.642	3	10.16137	20.8499
5221	UDS4	34.58308	-5.24693	1.006	1.049	4	9.9425	21.1226

ID	Mask	spec RA	spec DEC	photoz	specz	Qf	log(M*)	IRAC (3.6 μm) mag
5322	UDS3	34.226045	-5.248964	0.603	0.629	4	11.17026	18.3691
5502	UDS4	34.44525	-5.244926	0.875	0.817	3	8.45939	24.3811
5554	UDS4	34.478522	-5.244534	1.173	1.2385	3	9.44404	22.4003
5706	UDS4	34.466851	-5.243435	0.908	0.941	3	8.87622	23.479
5888	UDS4	34.575208	-5.242759	0.886	0.877	3	9.08279	23.0846
6122	UDS4	34.496335	-5.241093	1.192	1.309	3	9.44716	22.5558
6126	UDS4	34.552834	-5.242236	0.636	0.629	3	10.04922	20.0492
6737	UDS4	34.360687	-5.239207	0.81	0.824	3	10.41664	20.2139
6821	UDS4	34.584531	-5.238286	0.823	0.785	4	9.31387	22.3826
7355	UDS3	34.479923	-5.236412	0.512	0.445	4	10.233	20.1203
7753	UDS13	34.537155	-5.23371	0.72	0.748	4	10.20952	20.3391
7848	UDS4	34.430465	-5.234544	0.589	0.602	4	10.26717	19.5579
7891	UDS3	34.458523	-5.234976	0.649	0.651	4	10.18184	19.7174
8019	UDS4	34.567101	-5.232267	1.42	1.41	3	10.78032	19.8578
8067	UDS4	34.476053	-5.230864	1.29	1.28	3	9.03743	24.0062
8158	UDS13	34.498278	-5.231144	0.676	0.669	4	9.0086	22.9097
8163	UDS3	34.415456	-5.232016	0.885	0.943	3	10.35218	19.9964
8221	UDS3	34.435744	-5.231653	0.886	0.914	3	10.37107	19.8671
8364	UDS4	34.493694	-5.230464	0.621	0.629	4	9.08991	22.4212
8381	UDS4	34.512687	-5.231849	0.639	0.602	4	10.92376	18.6543
8565	UDS4	34.555685	-5.228391	0.967	0.961	3	9.08991	23.0683
8602	UDS4	34.568939	-5.228006	1.442	1.4125	3	10.02119	22.1102
8679	UDS13	34.535408	-5.22939	0.7	0.6275	3	10.18184	19.9458
8691	UDS13	34.501817	-5.227677	0.661	0.669	4	9.0607	22.6606
9101	UDS3	34.304356	-5.225821	1.426	1.413	3	10.05308	21.5443
9120	UDS3	34.256335	-5.227302	0.626	0.629	4	10.76938	19.0307
9244	UDS4	34.39186	-5.225039	0.568	0.649	3	10.15229	20.8575

ID	Mask	spec RA	spec DEC	photoz	specz	Qf	log(M*)	IRAC (3.6 μm) mag
9321	UDS3	34.421344	-5.225239	0.961	1.008	4	10.84011	19.763
9658	UDS4	34.49979	-5.221898	0.963	1.007	3	9.70157	21.7519
9699	UDS13	34.517319	-5.223323	0.666	0.669	4	10.27184	19.8551
9790	UDS13	34.322238	-5.221658	0.934	0.9225	3	9.43616	22.1542
9810	UDS4	34.507375	-5.222409	0.552	0.567	4	10.15836	19.8682
10004	UDS4	34.534958	-5.220623	0.917	0.9598	3	9.76343	21.2981
10289	UDS13	34.545604	-5.218359	0.612	0.615	4	9.00432	22.9089
10368	UDS4	34.516403	-5.220729	0.661	0.827	3	10.69897	19.0475
10413	UDS4	34.421713	-5.218212	0.939	0.987	4	10.06446	20.9393
10471	UDS4	34.40222	-5.217205	1.301	1.3472	3	9.0607	23.8711
10473	UDS13	34.452916	-5.219102	0.6	0.649	4	10.69197	19.5487
10713	UDS3	34.275997	-5.221577	0.626	0.6274	4	11.11059	18.3957
10744	UDS3	34.412354	-5.218083	0.641	0.6459	3	10.8109	19.4068
11004	UDS3	34.449542	-5.214906	0.651	0.65	3	9.46982	21.7996
11070	UDS13	34.465132	-5.214539	1.229	1.2788	3	9.36549	22.7986
11361	UDS1	34.377537	-5.21371	0.61	0.639	3	10.26951	20.6403
11480	UDS13	34.56527	-5.21259	0.579	0.331	4	10.06819	20.2364
11636	UDS3	34.313487	-5.211483	1.002	1.033	4	9.13033	22.8393
11815	UDS3	34.328744	-5.211274	0.669	0.67	4	9.87564	20.5632
12189	UDS3	34.300027	-5.207973	1.343	1.3815	3	9.64444	22.5828
12222	UDS3	34.272859	-5.210254	0.75	0.7775	3	10.84634	19.0281
12542	UDS4	34.373526	-5.205912	0.941	0.9138	3	9.08991	22.9869
12850	UDS1	34.33819	-5.206671	0.884	0.922	3	10.90363	19.0106
13395	UDS13	34.570065	-5.203277	0.711	0.67	4	10.48144	18.8071
13610	UDS1	34.375813	-5.201413	0.569	0.651	3	10.0086	20.9663
14059	UDS13	34.581467	-5.197879	6.475	6.1435	3	8.61805	26.6605
14227	UDS13	34.470917	-5.198445	0.605	0.494	4	10.14922	20.4202

ID	Mask	spec RA	spec DEC	photoz	specz	Qf	log(M*)	IRAC (3.6 μm) mag
14231	UDS1	34.465441	-5.197572	1.09	1.098	3	9.08279	23.1065
14287	UDS1	34.356533	-5.19965	0.604	0.645	3	10.06819	20.5382
14542	UDS2	34.264748	-5.196578	0.532	0.627	3	9.8739	21.1337
14743	UDS13	34.364497	-5.19585	0.64	0.65	3	10.50243	19.9545
14846	UDS13	34.503767	-5.193837	5.912	6.0275	3	9.40824	24.5902
14867	UDS1	34.481186	-5.19615	0.622	0.643	4	10.54033	20.0564
14922	UDS11	34.43526	-5.193962	3.22	3.223	3	10.53782	22.6783
14958	UDS1	34.418562	-5.19367	1.323	1.4015	3	9.1959	23.5107
15161	UDS11	34.411812	-5.193074	0.614	0.627	4	9.2878	22.0991
15226	UDS11	34.582226	-5.192831	0.58	0.601	3	10.44716	20.1343
15361	UDS13	34.549809	-5.191686	1.317	1.359	3	9.58771	22.4615
15538	UDS1	34.394748	-5.191059	1.354	1.418	3	10.14922	20.9767
15691	UDS1	34.334186	-5.190782	0.952	0.916	3	10.74974	19.4793
15721	UDS13	34.576023	-5.191152	0.546	0.602	4	10.4609	19.9158
16346	UDS1	34.321633	-5.185681	1.346	1.437	3	9.14613	23.2315
16509	UDS1	34.365681	-5.186302	0.535	0.572	3	10.15836	20.4979
16714	UDS2	34.395634	-5.184654	1.252	1.29	4	10.75358	20.0702
17018	UDS1	34.408851	-5.182571	1.333	1.365	3	10.11059	21.1278
17078	UDS12	34.395523	-5.181336	6.665	0.535	3	9.25527	25.1351
17162	UDS2	34.377072	-5.181148	1.005	0.5735	4	8.32222	24.7547
17277	UDS12	34.368453	-5.181222	0.601	0.651	3	9.11394	22.872
17390	UDS1	34.528271	-5.18019	0.635	0.668	3	10.05308	20.9878
17503	UDS1	34.503174	-5.179401	1.048	1.042	3	9.70927	21.6225
17629	UDS1	34.551491	-5.178602	2.92	2.7325	3	10.6902	21.2068
17646	UDS1	34.312296	-5.179665	0.677	0.6699	3	10.42813	19.5496
17971	UDS13	34.360262	-5.177836	0.578	0.649	3	9.90417	20.54
18087	UDS13	34.397219	-5.175689	5.974	6.119	3	9.73878	24.2229

ID	Mask	spec RA	spec DEC	photoz	specz	Qf	log(M*)	IRAC (3.6 μm) mag
18289	UDS12	34.266427	-5.175946	0.954	0.917	3	10.84011	19.885
18290	UDS12	34.331738	-5.177305	0.679	0.821	3	10.13354	20.0596
18305	UDS11	34.538158	-5.175509	0.614	0.633	3	9.77159	20.873
18349	UDS11	34.541626	-5.176441	0.585	0.647	3	10.36173	20.315
18390	UDS1	34.387786	-5.175381	1.378	1.42	3	10.4456	20.6762
18513	UDS1	34.389919	-5.175576	1.37	1.422	3	10.36361	20.7536
18547	UDS11	34.481147	-5.174333	1.234	1.275	3	10.63548	20.2302
18699	UDS2	34.245407	-5.172835	1.502	1.438	3	9.19033	23.881
19217	UDS2	34.361162	-5.170046	1.365	1.406	3	9.16732	23.7109
19220	UDS12	34.342894	-5.170655	1.1	1.09	3	9.47129	22.3392
19278	UDS1	34.34432	-5.173943	0.674	0.67	4	10.99695	18.3355
19546	UDS1	34.439971	-5.169346	1.444	1.416	3	10.64444	20.4594
19570	UDS13	34.554577	-5.170206	0.621	0.646	3	10.52504	19.4202
19754	UDS2	34.280745	-5.168216	0.858	0.9165	4	10.54777	19.8721
20155	UDS1	34.362745	-5.165288	1.058	1.098	3	9.88138	21.5172
20263	UDS13	34.548233	-5.165218	1.041	1.045	3	10.75435	19.9519
20313	UDS13	34.505827	-5.164312	0.95	0.988	3	9.50243	22.1448
20596	UDS2	34.325244	-5.162589	1.366	1.411	3	9.18752	23.3373
20775	UDS11	34.371823	-5.162398	0.797	0.8275	3	9.49831	21.7163
20802	UDS12	34.270307	-5.161927	0.912	0.896	4	9.32838	21.5222
21591	UDS2	34.268153	-5.157068	1.088	1.0858	3	9.09691	23.232
21824	UDS1	34.453807	-5.156206	0.64	0.6455	3	10.23805	20.711
21934	UDS13	34.512627	-5.15555	0.546	0.5715	4	9.62634	20.9708
22141	UDS12	34.333638	-5.155108	0.656	0.669	4	9.54777	21.2312
22153	UDS1	34.416972	-5.154744	1.362	1.398	3	10.07555	21.3821
22382	UDS2	34.326905	-5.152619	0.795	0.818	4	9.20952	22.7479
22551	UDS11	34.535078	-5.151734	1.287	1.278	3	9.06446	23.2231

ID	Mask	spec RA	spec DEC	photoz	specz	Qf	log(M*)	IRAC (3.6 μm) mag
22605	UDS2	34.27933	-5.152326	0.706	0.646	3	10.45025	19.7503
23089	UDS11	34.485422	-5.148983	1.429	1.405	3	9.29885	23.4196
23109	UDS12	34.23106	-5.150429	0.603	0.626	4	10.57749	19.0994
23274	UDS1	34.490365	-5.14304	1.246	1.267	3	10.27416	20.5405
23511	UDS1	34.422946	-5.146193	1.097	1.093	3	10.58092	20.4189
23645	UDS11	34.457415	-5.14552	0.837	0.877	3	9.41996	22.0857
23752	UDS1	34.501452	-5.147661	0.543	0.567	4	10.07918	20.5511
23876	UDS2	34.290441	-5.148261	0.538	0.628	4	10.33244	20.0476
23939	UDS12	34.275593	-5.126065	0.635	0.6455	3	9.70757	20.4373
24102	UDS2	34.388584	-5.12771	0.624	0.67	3	10.22272	20.0103
24122	UDS2	34.368408	-5.126579	0.917	1.019	3	9.39445	23.0093
24127	UDS2	34.417074	-5.127027	1.424	1.472	3	10.02938	21.7425
24197	UDS1	34.478604	-5.150949	0.753	0.876	3	10.17609	20.3479
24260	UDS2	34.387227	-5.126507	0.85	0.9303	3	8.4843	24.126
24336	UDS12	34.3044	-5.133208	0.617	0.647	4	10.34242	19.5144
24546	UDS2	34.292862	-5.135183	0.62	0.6275	4	11.19866	18.1196
24555	UDS2	34.312996	-5.128197	1.212	1.266	4	10.68395	20.2824
24597	UDS12	34.294029	-5.127845	0.813	0.8214	3	10.93702	18.954
24643	UDS2	34.305092	-5.12934	0.584	0.6472	4	9.71684	20.7849
24692	UDS2	34.274063	-5.129418	1.386	1.526	3	10.46538	20.8942
25096	UDS2	34.266706	-5.132782	0.781	0.818	4	10.71433	19.0332
25253	UDS12	34.279413	-5.133096	1.176	1.2285	3	10.1271	20.8794
25483	UDS12	34.297005	-5.134688	1.177	1.146	3	10.83442	19.8032
25543	UDS12	34.30908	-5.13418	1.471	1.4925	3	9.54654	22.8459
25640	UDS12	34.418592	-5.136093	1.05	1.097	3	10.27416	20.4668
25704	UDS11	34.471878	-5.133422	1.079	1.0947	3	10.04532	20.9508
25746	UDS2	34.35155	-5.135871	0.778	0.7886	4	9.14922	22.796

ID	Mask	spec RA	spec DEC	photoz	specz	Qf	log(M*)	IRAC (3.6 μm) mag
25815	UDS11	34.406069	-5.137347	0.65	0.651	4	8.79796	23.0409
26055	UDS1	34.507987	-5.138056	0.615	0.716	3	10.31387	20.4661
26097	UDS1	34.352786	-5.13757	1.4	1.41	3	9.26951	23.0674
26298	UDS1	34.316058	-5.139032	1.095	1.0925	3	9.39794	22.5882
26348	UDS12	34.294912	-5.139322	0.588	0.435	4	10.22011	20.7274
26373	UDS2	34.299858	-5.13979	1.606	1.65796	4	11.07188	19.7638
26384	UDS2	34.385796	-5.139738	0.609	0.67	4	10.14613	20.8788
26524	UDS1	34.429708	-5.139719	1.243	1.273	3	10.31175	20.7301
26525	UDS1	34.488697	-5.140328	1.364	1.405	3	9.7332	22.1904
26582	UDS1	34.43758	-5.139839	1.295	1.273	3	9.01703	23.648
26800	UDS1	34.404043	-5.141531	1.242	1.086	3	9.68664	22.4822
26801	UDS1	34.492737	-5.141916	1.24	1.106	3	10.44871	20.0981
26841	UDS11	34.554928	-5.141142	1.453	1.467	3	9.56703	22.6807
26952	UDS2	34.296085	-5.128668	0.82	0.822	4	10.50515	20.6859
27073	UDS1	34.504699	-5.142757	1.541	1.3905	3	9.02938	24.5165
28695	UDS3	34.249003	-5.251029	3.081	3.347	3	8.3927	-99.0
31947	UDS11	34.442312	-5.19364	5.978	1.265	3	9.53275	25.1466
34450	UDS12	34.384364	-5.150506	0.782	0.788	4	7.57519	26.2163

6.3 The CHESS EGS data

ID	Mask	spec RA	spec DEC	photoz	specz	Qf	log(M*)	IRAC (3.6 μm) mag
106	EGS1	215.297199	53.051868	0.685	0.736	3	10.146	20.9427
378	EGS1	215.28999	53.052352	1.134	1.138	3	10.0695	21.111
570	EGS1	215.186278	52.981484	1.362	1.022	3	10.3169	20.9309

ID	Mask	spec RA	spec DEC	photoz	specz	Qf	log(M*)	IRAC (3.6 μm) mag
853	EGS1	215.277085	53.04697	1.385	1.447	3	10.5208	20.7545
1053	EGS1	215.277466	53.047264	0.65	0.677	4	10.1654	20.1562
1064	EGS1	215.2313	53.017102	1.329	1.36	3	9.54936	22.5446
1290	EGS1	215.27894	53.051464	0.93	0.969	3	10.0414	21.0427
2000	EGS1	215.10864	52.93498	1.575	0.6925	3	10.8622	20.472
2021	EGS1	215.282332	53.055029	0.997	0.736	4	10.4536	19.1061
2496	EGS1	215.124199	52.948402	0.57	0.576	3	10.4937	19.5469
3112	EGS1	215.288132	53.069526	2.125	0.62	4	10.3813	20.4721
3695	EGS1	215.269395	53.059206	0.987	1.0195	3	9.83276	21.2759
3717	EGS1	215.089497	52.928703	0.631	0.671	4	10.925	18.986
3846	EGS2	214.78836	52.721087	0.522	0.5375	3	8.12403	24.3303
4038	EGS1	215.122321	52.957805	0.81	0.823	4	9.38139	22.1811
4244	EGS1	215.264402	53.058018	0.789	0.8275	4	10.2527	20.0167
4309	EGS1	215.109849	52.949076	0.8	0.779	3	9.71708	21.2634
5093	EGS1	215.184045	53.005281	1.157	1.118	3	11.1674	19.3268
5594	EGS1	215.120207	52.962807	0.675	0.746	4	10.6392	19.5835
5673	EGS1	215.11282	52.960499	0.726	0.741	3	10.0716	20.7561
6145	EGS1	215.079972	52.940889	1.245	1.263	3	8.88617	23.9184
6177	EGS1	215.21795	53.037024	1.28	1.445	3	10.2126	21.0614
7175	EGS2	214.735897	52.700194	0.65	0.6465	4	10.0483	19.9598
7539	EGS2	214.865545	52.797427	1.438	1.359	3	9.04183	23.805
7722	EGS1	215.172782	53.014279	1.123	0.749	3	10.2071	21.0805
7898	EGS1	215.0129	52.901446	0.7	0.7455	3	9.9796	20.391
7986	EGS2	214.860801	52.796214	0.495	1.1835	3	7.56426	24.7795
9005	EGS1	215.226145	53.059797	1.0	1.09	3	9.26927	22.7801
9332	EGS2	214.901692	52.831472	1.379	1.356	3	9.76352	22.2774
9672	EGS1	215.160298	53.01676	1.524	1.5425	3	9.2712	23.3358

ID	Mask	spec RA	spec DEC	photoz	specz	Qf	log(M*)	IRAC (3.6 μm) mag
10353	EGS2	214.799943	52.76307	0.499	0.457	4	10.4681	19.4952
10449	EGS1	215.112954	52.984147	1.03	1.0355	3	10.3207	20.4627
10518	EGS2	214.87712	52.819527	1.148	1.194	3	10.7237	19.7981
10599	EGS1	215.140608	53.004075	0.799	0.763	3	10.4901	19.1384
10700	EGS2	214.91512	52.846685	0.681	0.681	3	10.3427	20.1411
10927	EGS1	215.21558	53.061701	1.066	1.103	3	10.25	20.4857
11385	EGS3	215.21308	53.060931	0.752	0.8255	3	10.573	19.716
11502	EGS2	214.965175	52.887909	0.608	0.6355	3	8.495	24.141
11649	EGS2	214.882061	52.831075	0.579	0.497	4	7.78265	25.5988
11758	EGS3	215.20982	53.060886	0.798	0.809	3	10.0135	20.6613
11935	EGS2	214.90601	52.847249	0.732	0.7315	3	10.9116	19.5678
12097	EGS1	215.169498	53.033483	0.728	0.778	3	10.526	19.3652
12153	EGS2	214.773565	52.756285	1.02	0.956	3	9.06625	23.4493
12251	EGS3	215.110344	52.989586	0.604	0.6195	4	10.6575	19.411
12309	EGS1	215.041873	52.919926	0.517	0.638	3	10.402	18.7466
12413	EGS1	215.162365	53.030982	1.245	1.2575	3	10.7951	20.4602
12462	EGS1	215.12526	53.004814	1.563	1.5765	3	10.4575	20.8621
12768	EGS1	215.1164	52.997972	0.673	0.69	4	10.5787	19.3769
12933	EGS3	215.021987	52.936102	1.13	1.276	3	9.21201	22.9219
12955	EGS2	214.916147	52.851841	0.646	0.6705	3	10.195	18.2829
13002	EGS3	215.021337	52.935542	0.745	0.68	3	10.2065	20.3179
13068	EGS1	215.13848	53.017984	0.758	0.7767	3	10.0727	20.9027
13428	EGS1	215.133391	53.017083	1.175	1.219	3	10.0094	21.4739
13582	EGS3	215.05523	52.962252	0.715	0.743	3	10.2946	20.2232
13624	EGS3	215.198498	53.062472	1.111	1.103	4	10.8408	19.5051
13897	EGS2	214.680512	52.697866	1.303	1.383	3	10.2342	21.045
14173	EGS3	215.130786	53.018731	0.942	0.977	3	10.2133	20.5682

ID	Mask	spec RA	spec DEC	photoz	specz	Qf	log(M*)	IRAC (3.6 μm) mag
14240	EGS1	215.182511	53.054743	1.564	1.572	3	10.3634	21.1619
14252	EGS1	215.134057	53.01857	0.73	0.7775	4	10.5856	19.1765
14557	EGS1	215.21615	53.078048	1.131	1.18	3	10.632	19.93
14923	EGS1	215.130882	53.024317	0.885	0.951	4	8.20109	24.2502
14938	EGS3	215.205933	53.074624	0.789	0.807	4	10.239	19.9341
15381	EGS3	215.150568	53.039404	1.575	1.5705	3	10.0953	21.5973
15511	EGS3	215.0984	53.000484	1.222	1.2595	3	10.5148	19.7191
15813	EGS2	214.676694	52.702584	0.995	1.038	3	11.16	19.2897
15966	EGS3	215.134539	53.029116	0.557	0.5745	4	10.4817	19.7577
15969	EGS3	214.996828	52.935426	0.773	0.791	4	8.02619	25.0022
16107	EGS3	215.085655	52.997393	1.603	1.619	3	10.0175	21.9838
16399	EGS2	214.67445	52.70731	1.435	1.479	3	10.3051	21.3355
17004	EGS1	215.118738	53.023273	0.716	0.763	4	10.0071	20.5222
17101	EGS1	215.15711	53.052507	1.551	1.541	3	10.2996	21.3395
17141	EGS1	215.12744	53.030763	1.295	1.261	3	9.66726	22.3346
17179	EGS3	215.124989	53.02986	1.48	1.5405	3	10.0703	21.2419
17777	EGS2	214.83494	52.825806	0.535	0.5775	3	10.263	19.676
18468	EGS3	215.135738	53.045396	0.728	0.7945	4	9.01404	22.8325
18516	EGS3	215.018889	52.963959	1.525	1.5705	3	9.12865	24.2713
19418	EGS2	214.833703	52.837473	0.76	0.8015	3	7.6236	26.8465
19565	EGS2	214.7412	52.770173	1.321	1.355	3	10.2799	21.0653
19866	EGS3	215.009232	52.954264	0.428	0.356	4	10.7297	18.2682
20080	EGS3	215.035261	52.98055	0.455	0.453	4	10.5383	19.4959
20556	EGS2	214.75482	52.784303	1.33	1.3635	3	10.3103	20.8286
20784	EGS3	215.053086	52.997813	1.18	1.2445	3	9.87307	21.3715
21098	EGS2	214.81642	52.830193	0.889	0.9145	4	10.0557	20.8151
21194	EGS2	214.644007	52.709334	0.975	1.0305	3	10.0706	20.9677

ID	Mask	spec RA	spec DEC	photoz	specz	Qf	log(M*)	IRAC (3.6 μm) mag
21346	EGS3	215.04087	52.992113	1.201	1.259	3	10.1576	21.0245
21395	EGS1	215.170048	53.083073	1.378	1.394	3	10.2454	20.8541
21445	EGS3	215.09363	53.028927	1.091	1.0825	3	10.0286	21.2129
21890	EGS1	215.01401	52.975051	1.633	1.5625	3	10.0114	21.9625
22882	EGS2	214.73586	52.782846	0.807	0.8445	4	10.2533	20.6356
22884	EGS3	215.003135	52.965917	0.447	0.457	4	10.9825	18.5344
23017	EGS2	214.71984	52.771872	1.085	1.177	4	10.8866	19.5338
23417	EGS3	215.12253	53.061012	1.161	1.181	3	10.4573	20.4477
23429	EGS3	215.10124	53.04559	0.844	0.808	3	10.1555	20.4715
23528	EGS3	215.12753	53.06384	0.878	0.917	4	10.4171	20.473
23700	EGS3	215.088083	53.037394	1.37	1.44	3	10.5178	20.99
23913	EGS3	215.046481	53.008864	1.218	1.2425	3	10.6599	19.4756
25242	EGS2	214.779222	52.804784	1.029	1.017	3	10.5381	19.2768
25562	EGS3	215.040599	53.014646	0.664	0.681	3	9.37648	21.7008
25580	EGS3	215.148987	53.089251	0.779	0.808	3	10.2755	20.1497
26248	EGS2	214.648858	52.739442	0.875	0.924	4	9.40733	22.5018
26570	EGS2	214.629405	52.725712	0.98	1.029	3	10.0346	20.9871
28478	EGS3	214.883098	52.931629	0.362	0.349	3	10.0019	19.8417
29188	EGS3	214.910601	52.947187	0.759	0.758	3	10.5292	20.0031
30526	EGS3	215.123812	53.093588	0.962	0.978	3	10.1946	20.7184
30790	EGS3	214.9649	52.983159	1.177	1.2285	3	10.6559	20.0435
31449	EGS3	214.988774	52.990637	0.39	0.27	4	9.91703	19.116
31454	EGS3	215.085957	53.059659	1.525	1.5605	3	10.276	21.0492
31668	EGS3	214.95781	52.969946	0.427	0.462	4	9.67341	20.8997
31743	EGS3	214.992684	52.991779	1.179	1.1045	3	10.5316	19.635
35575	EGS2	214.912458	52.856549	0.39	0.435	4	8.95	-99.0

ID	Mask	spec RA	spec DEC	photoz	specz	Qf	log(M*)	IRAC (3.6 μm) mag
40960	EGS3	214.956658	52.98232	1.57	1.572	3	9.00213	24.146

7 Appendix B: Examples of CHESS Spectra

This appendix presents various examples of spectra obtained through the CHESS observing program. The showcased spectra include a broad range of sources, including typical star-forming galaxies, quiescent galaxies, Lyman α emitters, stellar spectra, instances of poor data reduction, and spectra that exhibit unusual features. The example spectra are shown in the SpecPro software in the format of both 1D and 2D spectra. The details about the objects and features are shown in figure descriptions.

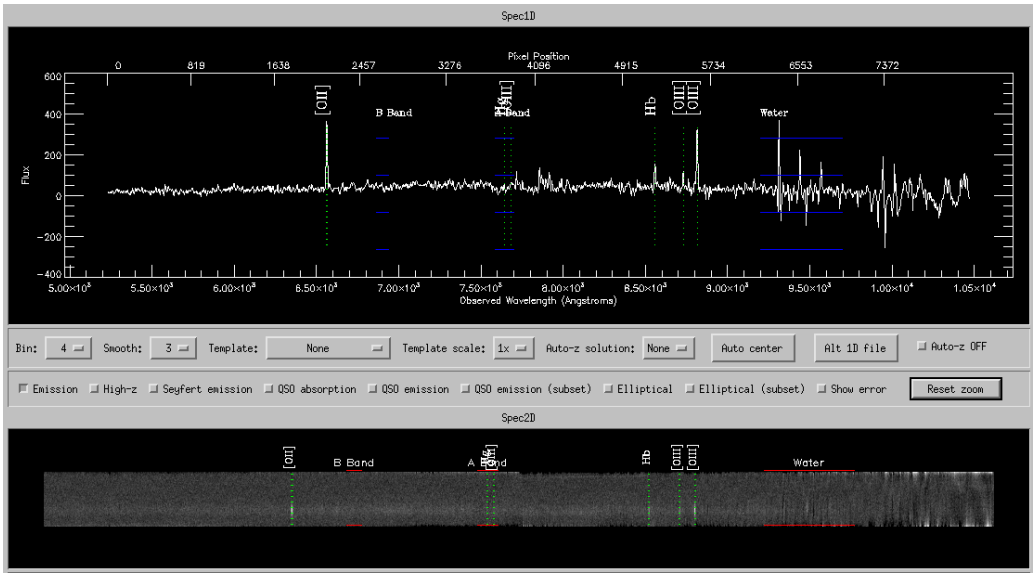

Figure 37: A star-forming galaxy spectrum with an ID of COS_11194 in the CANDELS COSMOS field. This spectrum shows many emission features including [OII], Hβ, and [OIII], indicating that this galaxy is likely to be a quiescent galaxy.

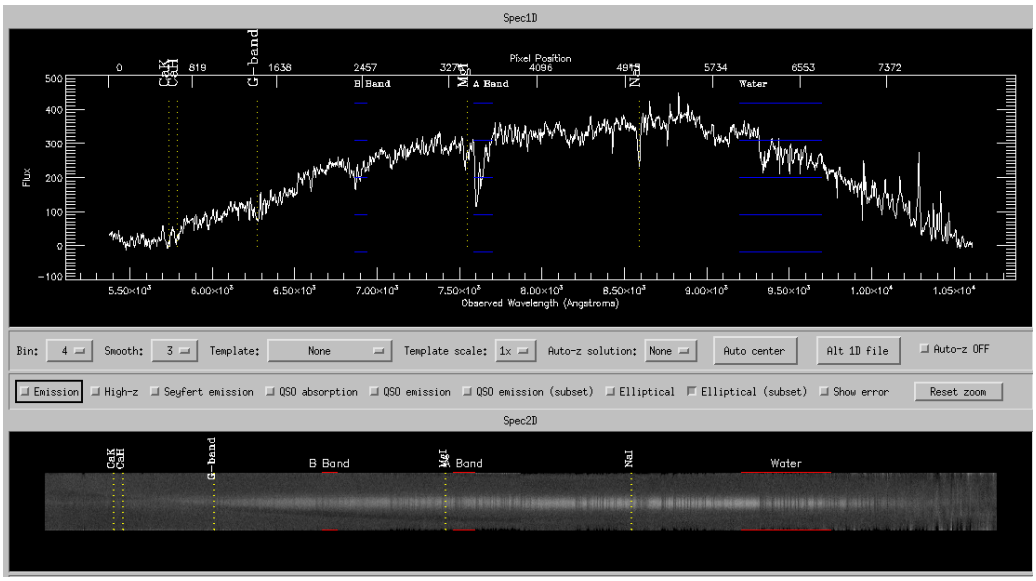

Figure 38: A quiescent galaxy spectrum with an ID of EGS_10353 in the CANDELS EGS field. This spectrum shows many absorption features including Ca K & H, G band, and MgI, indicating that this galaxy is likely to be a quiescent galaxy.

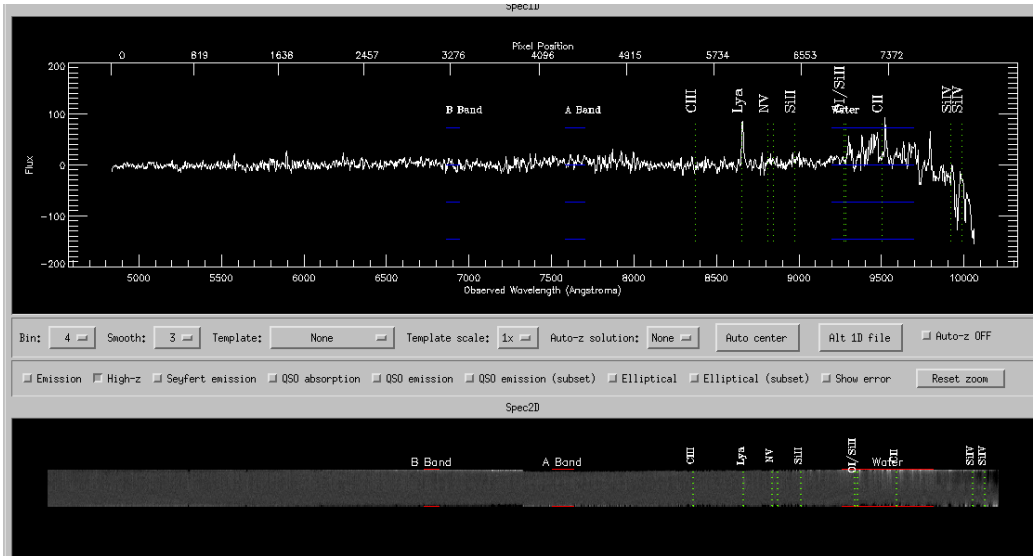

Figure 39: A galaxy spectrum with an ID of highz_18087 in the CANDELS UDS field showing a prominent Lyman α line at redshift $z_{spec} = 6.12$.

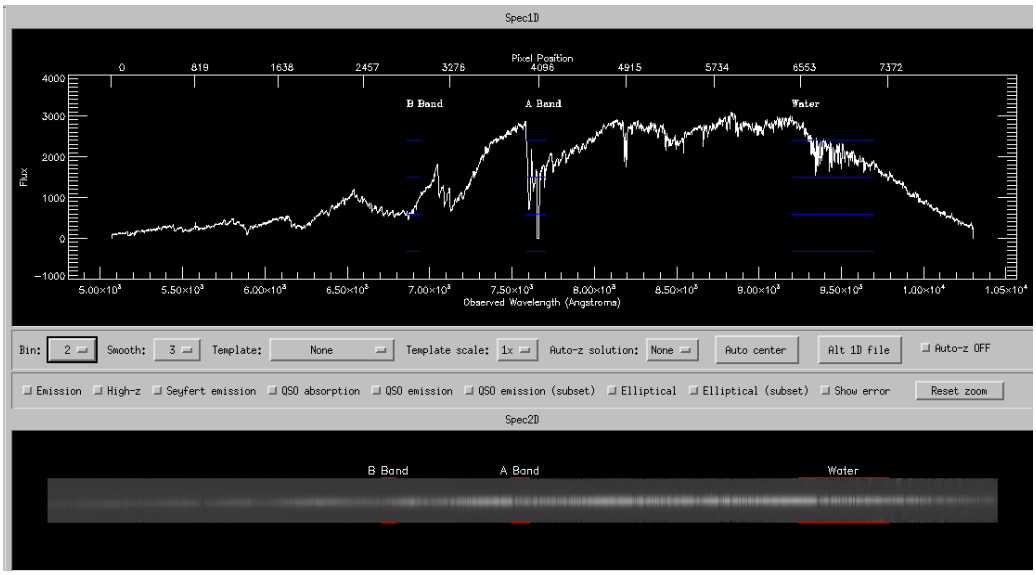

Figure 40: A stellar spectrum from a foreground star present in the EGS field.

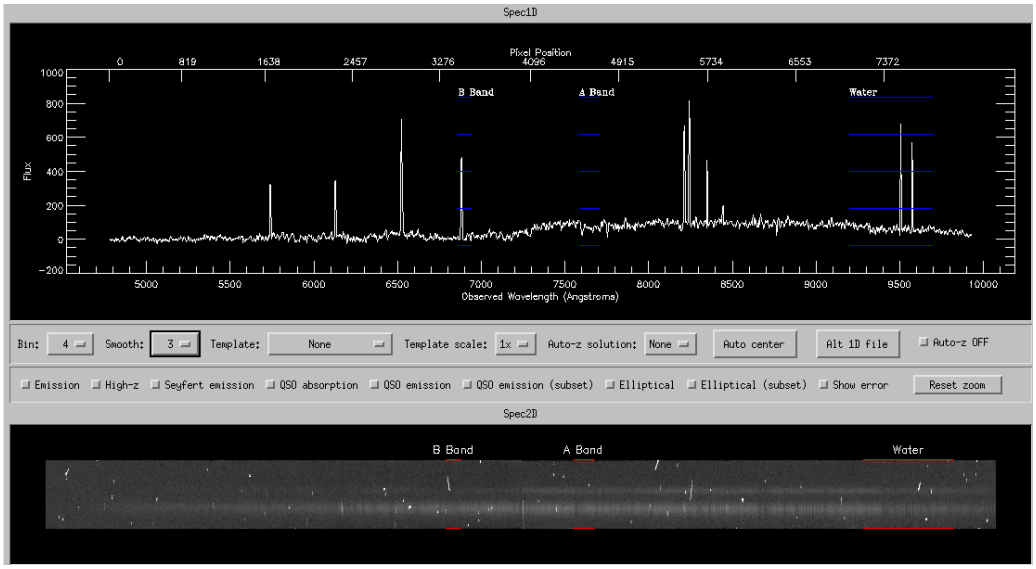

Figure 41: A galaxy spectrum with an ID of COS_23969 in the CANDELS COSMOS field. This spectrum was captured on November 29th, 2021, observing a run marked by adverse weather condition. The effect of bad weather made the DEEP2 pipeline unable to clean cosmic ray artifacts from this spectrum. We can also observe a serendipitous spectrum below the main spectrum.

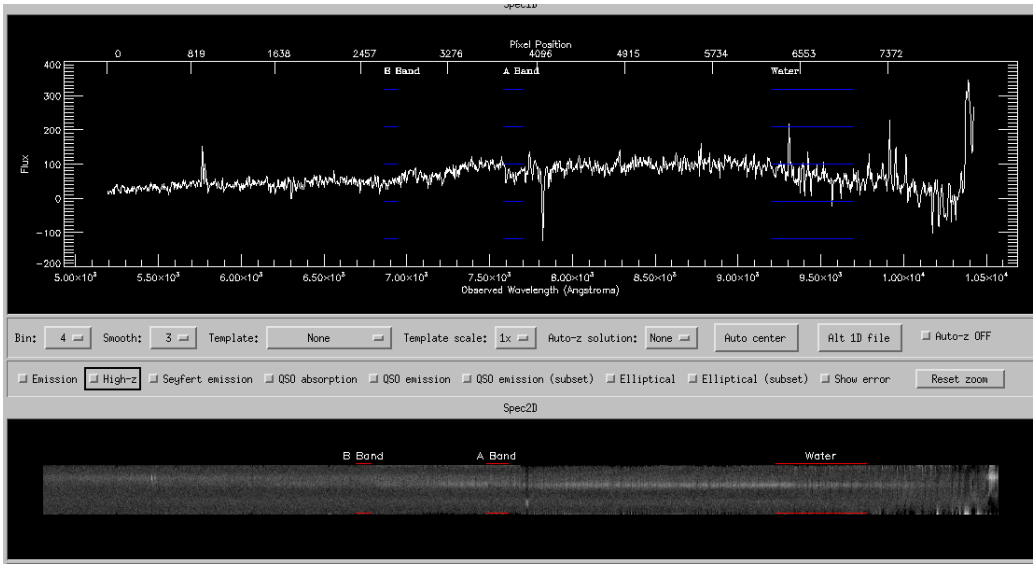

Figure 42: A galaxy spectrum with an ID of P_14187 in the CANDELS UDS field. This galaxy shows a doublet feature situated at the left side of the spectrum. This feature is suggestive of the Mg II 2796 emission line. However, due to the absence of additional emission features within the spectrum, the specz of this galaxy remains inconclusive.

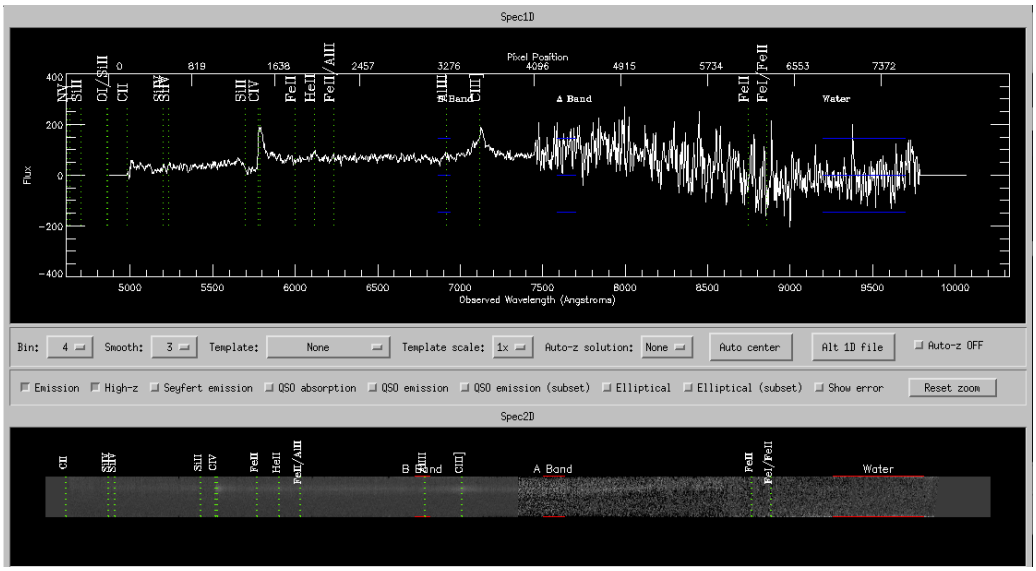

Figure 43: A galaxy spectrum with an ID of P_17629 in the CANDELS UDS field. This galaxy exhibits both a broad CIII] line and CIV line with the presence of a P-Cygni feature. The P-Cygni and the broad CIII] line suggest that this galaxy is a broad absorption line quasi stellar object (BAL QSO) (Lamy & Hutsemékers 2004). The spectrum of this galaxy is positioned on the CCD5 of the DEIMOS instrument, which results in a noisy spectrum on the red side.

Acknowledgments

From the accomplishment of this thesis, I would like to express my gratitude to Dr. Jeyhan Kartaltepe for her guidance in galaxy evolution research, as well as her assistance with writing and proofreading this thesis. Throughout two years of my studies, I have gained a deeper understanding of spectroscopy, galaxy evolution, programming, and observational astronomy. I would like to also thank Dr. Andrew Robinson, and Dr. Joshua Faber for their time to serve on my thesis committee.

Additionally, I would like to express my appreciation to all the volunteers (Brittany Vanderhoof, Sadie Coffin, Rohan Pattanik, Isabella Cox, Ali Ahmad Khostovan, Fiona Hufford, and Ash Bista) who contributed their time to measure spectroscopic redshifts and perform redshift reconciliation for the CHESS data. The CHESS spectroscopic catalog would not have been possible without the efforts of all volunteers from Jeyhan's research group.

Furthermore, I would like to thank Dr. Brian Lemaux for providing me with assistance on the basics of the Voronoi Monte-Carlo method to quantify the density and overdensity of extragalactic fields. His guidance enhanced my comprehension of the technical aspects of the Voronoi tessellation, and IDL programming, which are integral parts of my research.

Moreover, I would like to extend my gratitude to Jonathan Diaz for his contribution to identifying serendipitous sources in the CHESS spectra. His efforts and dedication during the summer of 2023 led to the successful addition of 31 new objects to the CHESS catalog. His assistance has enhanced the quality and scope of this research substantially.

I also want to acknowledge the RIT community and the Astrophysical Sciences and Technology program for providing me with the necessary astrophysical concepts for this research. The supportive academic environment at RIT helped me grow as a person and challenged me to develop into a more proficient astronomer.

Last but not least, I would like to express sincere gratitude to my family and my friends who support me throughout the master's program. Their emotional support played a crucial role to overcome all challenges I faced during my studies throughout the program.

References

Aguirre J. E., Bolocam Galactic Plane Collaboration 2007, in American Astronomical Society Meeting Abstracts. p. 89.25

Alexander D. M., et al., 2003, , 126, 539

Ashby M. L. N., et al., 2013, , 769, 80

Attali D., Boissonnat J.-D., 2004, Discrete and Computational Geometry, 31, 369

Barro G., et al., 2019, The Astrophysical Journal Supplement Series, 243, 22

Bermejo-Climent J. R., et al., 2018, Monthly Notices of the Royal Astronomical Society, 479, 1514

Boquien M., Buat V., Perret V., 2014, Astronomy &amp$$ Astrophysics, 571, A72

Boquien M., Burgarella D., Roehlly Y., et al., 2019, Astronomy &amp$$ Astrophysics, 622, A103

Bouché N., Lowenthal J. D., 2005, The Astrophysical Journal, 623, L75

Bradshaw E. J., et al., 2013, , 433, 194

Breiman L., Meisel W., Purcell E., 1977, Technometrics, 19, 135

Butcher H., Oemler A. J., 1978, , 219, 18

Capak P., et al., 2004, , 127, 180

Castellano M., et al., 2010, , 511, A20

Chartab N., et al., 2020, The Astrophysical Journal, 890, 7

Coil A. L., et al., 2004, , 609, 525

Coil A. L., et al., 2011, , 741, 8

Coil A. L., et al., 2015, The Astrophysical Journal, 801, 35

Combes F., 2017, Frontiers in Astronomy and Space Sciences, 4

Conroy C., 2013, Annual Review of Astronomy and Astrophysics, 51, 393

Cooper M. C., et al., 2007, Monthly Notices of the Royal Astronomical Society, 383, 1058

Cooper M. C., Newman J. A., Davis M., Finkbeiner D. P., Gerke B. F., 2012, spec2d: DEEP2 DEIMOS Spectral Pipeline, Astrophysics Source Code Library, record ascl:1203.003 (ascl:1203.003)

Cuillandre J. C., Starr B., Isani S., McDonald J. S., Luppino G., 2001, in Clowes R., Adamson A., Bromage G., eds, Astronomical Society of the Pacific Conference Series Vol. 232, The New Era of Wide Field Astronomy. p. 398

Darvish B., Sobral D., Mobasher B., Scoville N. Z., Best P., Sales L. V., Smail I., 2014, The Astrophysical Journal, 796, 51

Darvish B., Mobasher B., Sobral D., Scoville N., Aragon-Calvo M., 2015, , 805, 121

Darvish B., Mobasher B., Sobral D., Rettura A., Scoville N., Faisst A., Capak P., 2016, , 825, 113

Davis M., et al., 2007, The Astrophysical Journal, 660, L1

Delvecchio I., Lutz D., Berta S., et al., 2015, Monthly Notices of the Royal Astronomical Society, 449, 373

Elbaz D., et al., 2007, Astronomy &amp$$ Astrophysics, 468, 33

Elbaz D., et al., 2011, , 533

Faber S. M., et al., 2003, in Instrument Design and Performance for Optical/Infrared Ground-based Telescopes. pp 1657–1669

Feldmann R., Mayer L., 2014, Monthly Notices of the Royal Astronomical Society, 446, 1939

Ferrarese L., Merritt D., 2000, , 539, L9

Furusawa H., et al., 2008, The Astrophysical Journal Supplement Series, 176, 1

Gabor J. M., Davé R., Finlator K., Oppenheimer B. D., 2010, Monthly Notices of the Royal Astronomical Society, 407, 749

Galametz A., et al., 2013, The Astrophysical Journal Supplement Series, 206, 10

Garilli B., et al., 2021, Astronomy &amp$$ Astrophysics, 647, A150

Giacconi R., et al., 2002, , 139, 369

Grogin N. A., et al., 2011, The Astrophysical Journal Supplement Series, 197, 35

Gruppioni C., et al., 2013, Monthly Notices of the Royal Astronomical Society, 432, 23

Guo Y., et al., 2013, , 207, 24

Hasinger G., et al., 2007, The Astrophysical Journal Supplement Series, 172, 29

Hatch N. A., Overzier R. A., Kurk J. D., et al., 2009, Monthly Notices of the Royal Astronomical Society, 395, 114

Heavens A., Panter B., Jimenez R., Dunlop J., 2004, , 428, 625

Hilton M., et al., 2010, , 718, 133

Hung D., et al., 2019, Monthly Notices of the Royal Astronomical Society, 491, 5524

Icke V., van de Weygaert R., 1987, , 184, 16

Ivison R. J., et al., 2007, , 660, L77

Jannuzi B. T., Dey A., 1999, in Bunker A. J., van Breugel W. J. M., eds, Astronomical Society of the Pacific Conference Series Vol. 193, The Hy-Redshift Universe: Galaxy Formation and Evolution at High Redshift. p. 258

Kellermann K. I., Fomalont E. B., Mainieri V., Padovani P., Rosati P., Shaver P., Tozzi P., Miller N., 2008, , 179, 71

Kennicutt Robert C. J., 1992, , 79, 255

Kennicutt R. C., 1998, Annual Review of Astronomy and Astrophysics, 36, 189

Kennicutt R. C., Evans N. J., 2012, Annual Review of Astronomy and Astrophysics, 50, 531

Kennicutt Robert C. J., Tamblyn P., Congdon C. E., 1994, , 435, 22

Kodra D., et al., 2023, The Astrophysical Journal, 942, 36

Koekemoer A. M., et al., 2011, , 197, 36

Koyama Y., et al., 2013, , 434, 423

Laird E. S., et al., 2009, , 180, 102

Lamy H., Hutsemékers D., 2004, , 427, 107

Lawrence A., et al., 2007, , 379, 1599

Leitherer C., Heckman T. M., 1995, , 96, 9

Lemaux B. C., et al., 2018, Astronomy &amp$$ Astrophysics, 615, A77

Lilly S., et al., 2007, The Astrophysical Journal Supplement Series, 172, 70

Lilly S. J., et al., 2009, , 184, 218

Madau P., Dickinson M., 2014, Annual Review of Astronomy and Astrophysics, 52, 415

Madau P., Pozzetti L., Dickinson M., 1998, , 498, 106

Masters D., Capak P., 2011, Publications of the Astronomical Society of the Pacific, 123, 638

Mo H., van den Bosch F. C., White S., 2010, Galaxy Formation and Evolution

Momcheva I. G., et al., 2016, , 225, 27

Morrison G. E., Owen F. N., Dickinson M., Ivison R. J., Ibar E., 2010, The Astrophysical Journal Supplement Series, 188, 178

Mullaney J. R., Alexander D. M., Goulding A. D., et al., 2011, Monthly Notices of the Royal Astronomical Society, 414, 1082

Nandra K., et al., 2015, , 220, 10

Nayyeri H., et al., 2017, The Astrophysical Journal Supplement Series, 228, 7

Newman J. A., et al., 2013, , 208, 5

Nonino M., et al., 2009, , 183, 244

Peng Y.-j., et al., 2010, , 721, 193

Rettura A., et al., 2010, , 709, 512

Retzlaff J., Rosati P., Dickinson M., Vandame B., Rité C., Nonino M., Cesarsky C., GOODS Team 2010, , 511, A50

Robert C. Kennicutt J., 1998, The Astrophysical Journal, 498, 541

Salpeter E. E., 1955, , 121, 161

Sanders D. B., et al., 2007, , 172, 86

Schinnerer E., et al., 2004, The Astronomical Journal, 128, 1974

Schinnerer E., et al., 2007, The Astrophysical Journal Supplement Series, 172, 46

Schmidt M., 1959, , 129, 243

Schreiber C., et al., 2015, Astronomy &amp$$ Astrophysics, 575, A74

Schutte Z., Reines A. E., Greene J. E., 2019, The Astrophysical Journal, 887, 245

Scoville N., et al., 2007, The Astrophysical Journal Supplement Series, 172, 1

Scoville N., et al., 2013, The Astrophysical Journal Supplement Series, 206, 3

Sekiguchi K., et al., 2004, in , Vol. 5, Annual Report of the National Astronomical Observatory of Japan. p. 40

Silverman B. W., 1986, Density estimation for statistics and data analysis

Simpson C., et al., 2006, Monthly Notices of the Royal Astronomical Society, 372, 741

Stefanon M., et al., 2017, The Astrophysical Journal Supplement Series, 229, 32

Urrutia T., et al., 2019, , 624, A141

Vavilova I., Elyiv A., Dobrycheva D., Melnyk O., 2021, in , Intelligent Astrophysics. Springer International Publishing, pp 57–79, doi:10.1007/978-3-030-65867-0˙3, https://doi.org/10.1007%2F978-3-030-65867-0_3

Venemans B. P., et al., 2006, Astronomy &amp$$ Astrophysics, 461, 823

Weiß A., et al., 2009, , 707, 1201

Williams R. E., et al., 1996, , 112, 1335

Williams R. J., Quadri R. F., Franx M., van Dokkum P., Labbé I., 2009, The Astrophysical Journal, 691, 1879

Willner S. P., et al., 2006, , 132, 2159

Yoshikawa T., et al., 2010, , 718, 112

Zamojski M. A., et al., 2007, , 172, 468

da Cunha E., Charlot S., Elbaz D., 2008, , 388, 1595

van der Wel A., et al., 2021, The Astrophysical Journal Supplement Series, 256, 44